Spatial variability of light regimes under Arctic sea ice

by

Christian Katlein

A Thesis submitted in partial fulfillment
of the requirements for the degree of

Doctor of Philosophy in Geosciences

Approved Dissertation Committee:

Prof. Dr. Rüdiger Gerdes
Prof. Dr. Vikram Unnithan
Dr. Marcel Nicolaus

Date of Defense: 30th September 2015

4

Table of Contents

1. Abstract

Light transmission through Arctic sea ice is an important process for the energy partitioning in the climate system. Thus understanding its spatial variability is important for a precise determination and prediction of energy fluxes across the atmosphere-ice-ocean interface. In this thesis the variables driving this variability – such as melt pond cover and ice thickness – as well as the length scales of this variability are investigated together with experimental and theoretical analysis of the geometry of optical properties of the ice cover. The work is based on optical measurements conducted during under ice surveys with remotely operated vehicles employing an interdisciplinary sensor package. It is found that the spatial scale of the light field variability under sea ice is driven by variations in ice albedo on scales of hundred meters and by ice thickness variability on larger scales. Also, the geometry of the light-field under sea ice is strongly influenced by the lateral inhomogeneity of the sea ice cover, further complicating the interpretation of standard ocean optics measurements. This thesis shows, that due to the lamellar crystal structure of sea ice, light propagation within is dependent on the direction of photon travel. The operations of under ice remotely operated vehicles also enabled an interdisciplinary study, showing that the spatial distribution of algal aggregates underneath sea ice is not governed by typical habitat properties such as light availability or temperature, but by a hydrodynamic interaction of the buoyant algal aggregates with the ice bottom topography. These results were applied in a new light parameterization allowing for the calculation of Arctic wide in and under ice primary production and will lead to a better ability to assess the impact of the spatial inhomogeneity in sea ice on the large scale energy budget of the melting Arctic sea ice.

2. Introduction

This thesis is structured as follows: The introduction provides a general overview about the topic of this thesis and introduces the scientific objectives. It thematically links and lists the four scientific papers comprised in this thesis, as well as the related contributions to co-authored papers. The four first author manuscripts are included in full text and comprise the main part of this thesis. The papers are followed by an overarching discussion, summarizing the key results and discussing their meaning and relevance as well as implications for future investigations.

2.1. Arctic sea ice

Sea ice - frozen sea water covering large parts of the Polar Ocean - is a key component of the Arctic climate- and ecosystem. As a frozen cover floating on top of the ocean, sea ice has a significant impact on the fluxes of energy and momentum between atmosphere and ocean. One of the most prominent properties of this ice cover is its white color, originating in the fact that sea ice and the snow cover on top reflect a large portion of the incident solar shortwave radiation independent of wavelength in the visible band [*Grenfell*, 1977; *Perovich*, 1996]. Despite the extreme climatic conditions with winter temperatures far below zero degrees Celsius, total darkness during the winter and day round sunlight in summer, the Arctic Ocean is home to a complex ecosystem ranging from unicellular algae to the polar bear, the iconic top predator of the Arctic [*Arrigo*, 2014; *Melnikov*, 1997]. Furthermore sea ice is both a barrier to shipping activities, as well as it is used for transportation by the indigenous people of the north. Due to this importance, knowledge about the present state of sea ice as well as about its future evolution is of high interest to both the general public and polar scientists around the world.

In the last century, explorers and scientists have put huge efforts into the exploration and investigation of the Arctic. While early observations were the first to discover the general properties of the Arctic ice cover, observational efforts have been intensified in the last decades forming the basic understanding of the processes and dynamics linking atmosphere, ocean and sea ice in the Arctic. In the last two decades, Arctic-wide observations show distinct changes in the characteristics of the sea ice cover [*Meier et al.*, 2014; *Perovich*, 2011] in line with warming global mean temperatures and rising levels of atmospheric carbon

dioxide [*Solomon*, 2007]. These changes strongly affect the properties of the Arctic sea-ice and will have tremendous effects on the climate and ecosystem.

One of the most prominent processes governing the retreat of the Arctic sea ice is the ice-albedo feedback [*Curry et al.*, 1995; *Perovich et al.*, 2011]. Sea-ice reflects up to 87% of the incident sunlight, but when it melts, it exposes dark ocean waters that absorb more than 90% of the solar energy [*Perovich*, 1996; *Perovich and Polashenski*, 2012; *Perovich et al.*, 2002]. This energy absorption leads to a heating of the uppermost water layers which further promotes sea ice melt. The feedback loop causes the Arctic sea ice and climate to react particularly sensitive to changes in the mean global temperature, amplifying the signal of a warming climate in the Arctic. Thus it is crucial to investigate the partitioning of solar energy at the ice interface between atmosphere and ocean for a detailed understanding of the climate system.

2.2. Changing physical properties of sea ice

During the last decades, ice based, marine, airborne, and satellite based observations show a distinctive change in the properties of the Arctic sea ice. First and foremost the spatial extent of the sea ice cover is decreasing in all regions and seasons in the Arctic. Sea ice extent is on average reduced about 100 000 km² - an area as huge as Iceland - every year [*Serreze et al.*, 2007]. The Arctic sea ice has to date already lost approximately 30% of its extent at the annual minimum in September as compared to the beginning of regular observations by satellites in 1979 [*Fetterer et al.*, 2002, updated daily]. The observed reduction of sea ice extent is reproduced by the Climate models of the Intergovernmental Panel on Climate Change (IPCC), but most models underestimate the magnitude of the decrease [*Stroeve et al.*, 2007; *Stroeve et al.*, 2012].

Along with the decrease in sea ice extent, also the thickness of the sea ice has been reduced dramatically. Observations from various airborne [*Haas et al.*, 2008; *Renner et al.*, 2014], underwater and satellite observations [*Kwok and Rothrock*, 2009] show that ice thickness in some areas has been reduced by up to 60% since the early 1990s [*Lindsay and Schweiger*, 2015; *Rothrock et al.*, 2008]. Also the predominance of older multi-year pack ice in the Arctic Ocean has been replaced by a regime dominated by first-year or even seasonal ice cover [*Maslanik et al.*, 2011; *Maslanik et al.*, 2007]. Both, changes in ice thickness and age are reflected in changing physical properties, such as increasing sea ice drift speed [*Kwok et al.*, 2013; *Rampal et al.*, 2009] and an increased coverage of the

ice by melt ponds during summer [*Rösel and Kaleschke*, 2012] also fostered by an increasing length of the melting season [*Markus et al.*, 2009]. The impact of these changed physical characteristics on the optical properties of sea ice and the radiation partitioning between atmosphere, sea ice and ocean is thus a mayor concern in this thesis.

2.3. The energy budget of sea ice

Three groups of fluxes govern the energy budget of sea ice: The shortwave radiative fluxes, longwave radiative fluxes and the turbulent fluxes exchanging heat with ocean and atmosphere. Figure 1 gives an overview over these fluxes and their respective typical magnitudes.

A large portion of the incident shortwave radiative flux is reflected back into the atmosphere due to the high surface albedo of sea ice. Nevertheless some portion gets absorbed within the ice leading to ice warming and internal melting changing the physical properties of the ice while another portion is transmitted into the underlying ocean sustaining primary production and heating the upper water column [*Perovich*, 1990; 1996]. This thesis mostly discusses the partitioning of solar shortwave radiation. The relative contribution of shortwave energy to the energy budget of sea ice is biggest during summer, when sea ice albedo is low and a significant portion gets transmitted through the ice.

Similarly, longwave radiation emitted as thermal radiation due to the surface temperature contributes to the energy budget. The net longwave radiative flux can be positive or negative and is mostly depending on the surface temperature and cloud cover [*Hudson et al.*, 2013]. Longwave fluxes are most relevant during winter and the transition seasons and can cause considerable cooling of the surface of up to -50 W/m².

Turbulent fluxes from the atmosphere lead to ice growth or melting caused by cold or warm atmospheric temperatures, but their contribution is usually rather small except during certain pronounced weather events. The positive ocean heat flux melts the sea ice from below or inhibits refreezing if it dominates over the other heat fluxes [*Maykut and Untersteiner*, 1971]. The influence of the ocean heat flux is more pronounced, where ocean circulation brings warm water into the Arctic, such as in Fram Strait or in the Barents Sea. In the Central Arctic basin, where the influence of warm water inflow is limited, the ocean heat flux is considerably lower on the order of a few W/m².
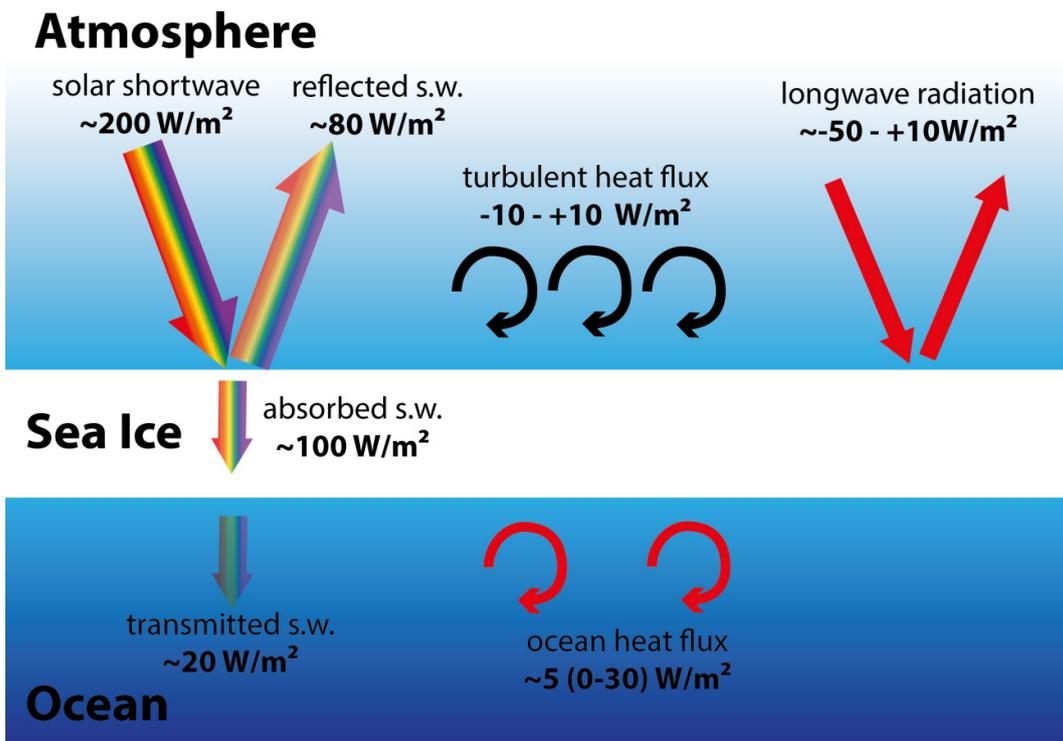
Figure 1: Summary of the energy fluxes and their magnitudes at the atmosphere-ice-ocean boundary. Values are taken from the literature [*Lu et al.*, 2013; *Nicolaus et al.*, 2012; *Perovich and Elder*, 2002].

This balance of energy fluxes determines the thermodynamic growth and melt of the sea ice cover. Precise representation of the energy fluxes in sea ice models is crucial for accurate modeling and prediction of the growth and particularly the melting of the polar pack ice. Thus understanding the effects of the changed physical properties on the energy budget of sea ice is important for both realistic climate projections as well as reliable seasonal sea ice forecasts.

2.4. Optical properties of sea ice

This thesis focuses on sunlight of the spectral range between 320 nm to 950 nm, covering a little bit more than the entire visible band. As the thesis is mainly concerned with light transmission through sea ice, this wavelength band is representative for the major part of the solar shortwave radiation (200nm to 2000nm) as light outside of the visible band gets strongly attenuated by sea ice [*Grenfell and Perovich*, 1981; *Grenfell et al.*, 2006].

Analogously to the surface albedo, which is defined as the ratio of reflected planar irradiance divided by the incident planar irradiance , sea ice transmittance (transflectance) is defined as the ratio of transmitted planar irradiance (radiance) divided by the incident planar irradiance [*Nicolaus and Katlein*, 2013; *Perovich*, 1996]

Both quantities are apparent optical properties that can be determined by conceptually simple field measurements [*Eicken and Salganek*, 2010; *Perovich et al.*, 1998b]. They can be presented as broadband values for different wavelength bands, as well as spectral quantities with a dependence on wavelength. While such apparent optical properties are simple to measure, they are dependent on measurement geometry and illumination conditions and not strictly speaking properties of the material [*Mobley*, 1994]. Light transfer in sea ice can be understood on a finer scale in the theory of radiative transfer [*Chandrasekhar*, 1960], where light is interacting with the material by scattering and absorption which are inherent optical properties of the material.

The amount of energy transmitted through sea ice is to a high degree dependent on the optical properties of the surface layer – the presence of snow, melt ponds or a surface scattering layer, but also on the thickness of the ice and its internal temperature dependent structure [*Light et al.*, 2003a; *Light et al.*, 2008; *Perovich*, 1990].

Sea ice and snow are strongly scattering media complicating radiative transfer simulations [*Grenfell and Hedrick*, 1983; *Light et al.*, 2003b; *Petrich et al.*, 2012a; *Trodahl et al.*, 1987]. Various models for the calculation of light transmission through sea ice exist, ranging from simple parameterizations, where light transmission can be derived from ice albedo, the ice thickness and an extinction coefficient using an exponential decay model similar to Beer's law [*Grenfell*, 1977] over multi-stream [*Perovich*, 1990; 1996] and discrete ordinate models [*Ehn et al.*, 2008; *Hamre et al.*, 2004] to highly complex Monte-Carlo ray tracing models [*Light et al.*, 2003b; *Petrich et al.*, 2012a] that enable the calculation of light transmission in inhomogeneous media. As a different degree of precision is needed for every application, the model needs to be chosen according to its purpose [*Holland et al.*, 2011]. Thus this thesis makes use of different models from the simplest exponential model to anisotropic ray tracing.

2.5. Spatial variability of sea ice properties

While sea ice is often represented as a horizontally homogenous slab in models [*Arrigo et al.*, 1991; *Light et al.*, 2008; *Maykut and Untersteiner*, 1971; *Mobley et al.*, 1998], the reality looks much different. The physical properties of sea ice don't only vary in time but also in space (Figure 2). While spatial variability on regional scale can be well represented in models, sea ice also exhibits high spatial variability on scales much smaller than the typical size of a grid box in sea ice models [*Thomas and Dieckmann*, 2010]. In addition to the fact that sea ice is

often a conglomerate of floes of different ice types with varying surface and bottom topography, thickness etc., smaller scale features caused by ice dynamics like ridges and cracks as well as a high spatial variation in the melt status from snow covered to ponded sea ice especially in summer, cause a high spatial variability of the ice properties relevant for light transmission [*Nicolaus et al.*, 2013a]. While melt water ponds on the sea ice increase light transmission through sea ice, a strongly scattering snow cover reduces light transmission [*Hudson et al.*, 2013; *Perovich*, 2005].

Understanding the influence of this spatial variability on light transmission is crucial as light transmission itself and many linked processes such as sea ice melt or biological production are highly nonlinear [*Arrigo et al.*, 2008]. This thesis thus investigates the effects of a spatially inhomogeneous sea ice layer on the under-ice light field to increase our knowledge how the spatial variability of the sea ice cover needs to be taken into account for a correct handling of the shortwave radiative fluxes.
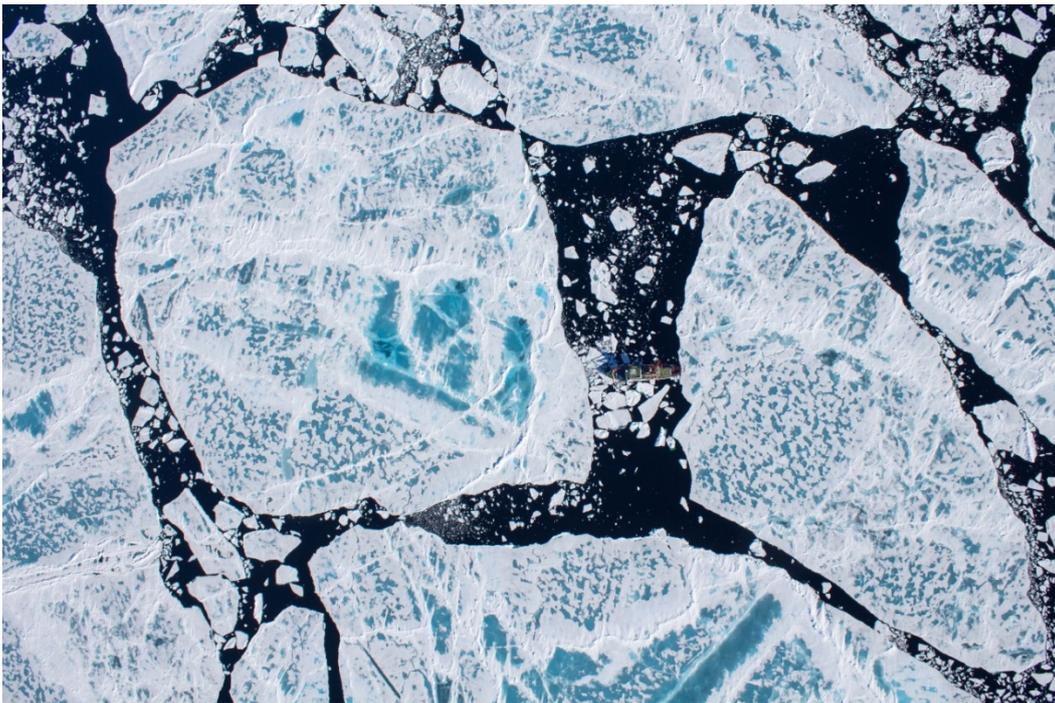

Figure 2: Aerial image of sea ice during the melting season showing the high spatial variability caused by melt ponds and pressure ridges on the sea ice floes of various size. The research icebreaker Polarstern (right of image center) has a length of 120m (Image: S. Arndt / AWI Meereisphysik).

2.6. Novel measurement concepts

Research in the polar areas has always been and is still a challenging undertaking. Even though the access to the Arctic has become easier with the construction of ice breaking ships, the Arctic Ocean remains considerably undersampled [*Gascard et al.*, 2008; *Polyakov et al.*, 2007]. The advent of autonomous drifting observatories has increased the amount of gathered seasonal data in the last two decades [*Krishfield et al.*, 2008; *Richter-Menge et al.*, 2006], but these measurements remain single point measurements in the vast pack ice with its high spatial variability [*Perovich and Richter-Menge*, 2006].

Optical measurements have often been centered around the determination of the surface albedo, as its measurement is conceptually simple and logistically less challenging than a measurement of light transmission that requires a light sensor underneath the ice. The developments in the field of underwater technology during the last decade, now also enable researchers to get a comprehensive picture of the conditions underneath Arctic sea ice. While under-ice light measurements using robotic technologies are still expensive, their application provides the advantageous capability to acquire spatially distributed datasets in a much shorter time span and with lower risk as compared to diving operations.

New robotic under-ice technology operated off research ice breakers with a highly interdisciplinary science team provides unique opportunities for a comprehensive and spatially extensive look at the underside of sea ice. In this thesis, we use two different remotely operated vehicles (ROV) to investigate the spatial variability of the light regimes under sea ice. Interdisciplinary sensor suites carried onboard the vehicles enable insights into the interplay of physics and biology widening the applicability and merit of the measurements. Apart from the use of novel technology, also progress in processing and interpretation of the optical data as well as in the theoretical description is necessary to be able to learn from these novel datasets of spatially resolved information.
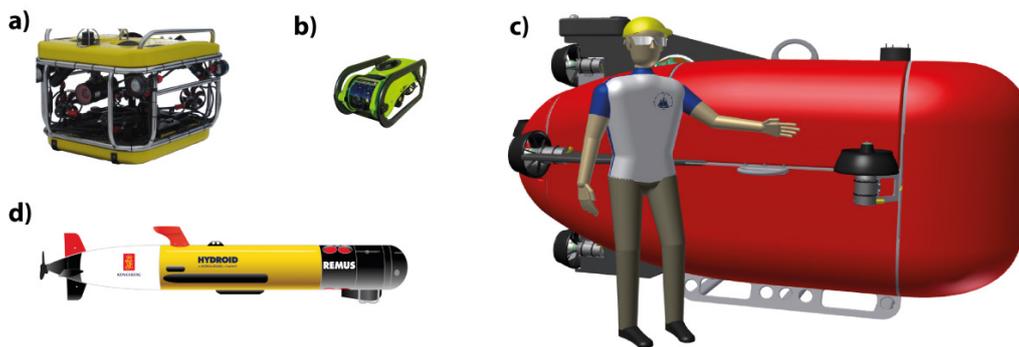
Figure 3: Different robotic underwater vehicles as used for under ice surveys. The relative size of the vehicles is to scale: a) Ocean Modules V8Sii observation class ROV able to carry a scientific sensor package as used during the Polarstern field campaigns in 2011, 2012 & 2015. Image: ACC Group AB b) SeaBotix camera ROV. Image: SeaBotix c) Nereid Under Ice (NUI) light-fiber tethered hybrid ROV as operated during the Polarstern field campaign in 2014. Image: WHOI NDSF d) REMUS autonomous underwater vehicle with under ice navigation capabilities. Image: Hydroid

2.7. Importance of light transmission for the sea ice ecosystem

Light transmission through Arctic sea ice also has a tremendous impact on the ecosystem. Ice algal and pelagic primary production is primarily fueled by sunlight transmitted through the ice until nutrient stocks are consumed towards the end of the season [*Arrigo et al.*, 2008; *Wassmann and Reigstad*, 2011]. The seasonal timing and development of the algal blooms is directly linked to the available light [*Arrigo et al.*, 2012; *Leu et al.*, 2010]. The observed changes in the sea ice cover, such as an earlier melt onset [*Markus et al.*, 2009] and higher light transmittance through thinner ice might critically offset the timing of algal blooms. If the zooplankton, depending on the algal blooms as a food source, is not able to adapt to these differences in timing, the resulting mismatch might have significant impact onto the food chain [*Leu et al.*, 2010; *Leu et al.*, 2011; *Wassmann and Reigstad*, 2011] and higher trophic levels up to fish stocks, whales and polar bears (Figure 4).

The fate of light driven ice algal blooms does not only influence the future development of the ice associated ecosystem, but variations in the physical conditions under the sea ice, favoring increased formation and subsequent sinking of algal aggregates [*Assmy et al.*, 2013; *Fernández-Méndez et al.*, 2014] might also have significant impact on the benthic ecosystem at the deep sea floor [*Lalande et al.*, 2014].

Vice versa, biological constituents in the sea ice also affect light transmission [*Arrigo et al.*, 1991; *Zeebe et al.*, 1996]. While this impact of sea ice biology on the physics of the energy budget is yet hard to quantify, it can reversely be used

as a tool to derive information about the algal content of the ice from spectral light measurements underneath the sea ice [*Legendre and Gosselin*, 1991; *Mundy et al.*, 2007].
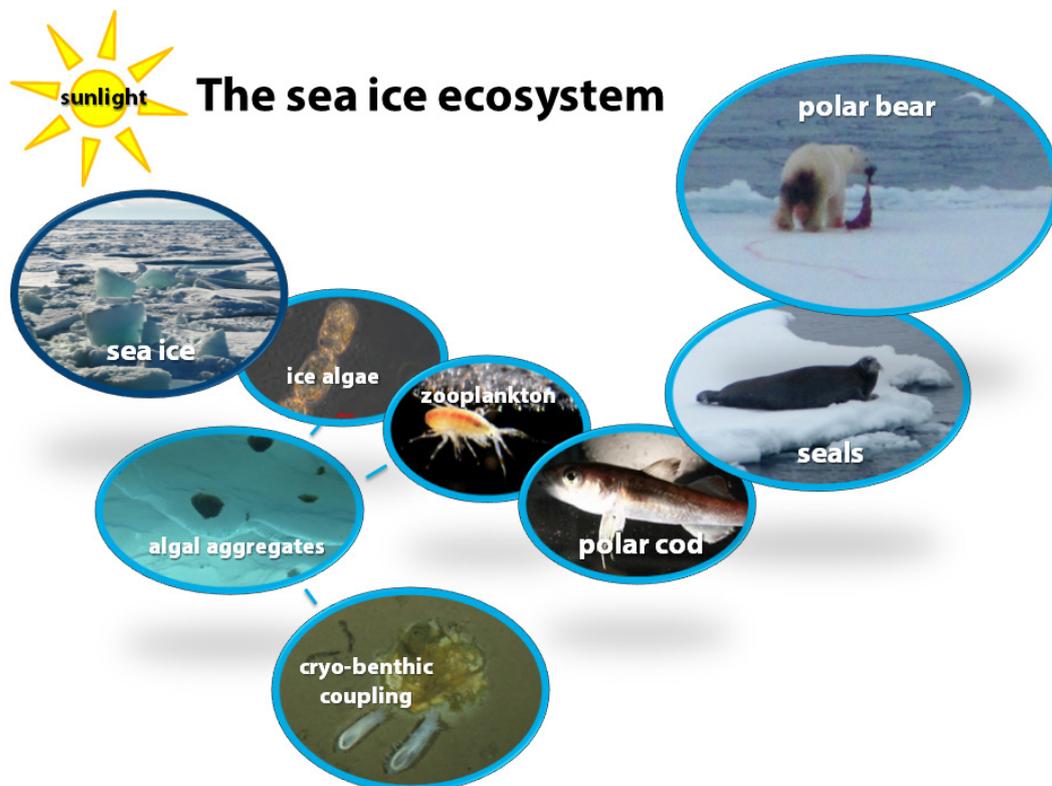
Figure 4: Schematic overview over the sea ice ecosystem: With sufficient sunlight, ice algae grow within the ice. Zooplankton is grazing on these algae, while in turn being prey of the polar cod, the food for seals. Polar bears are the top predators in this food web. After aggregation, ice algae can sink to the deep sea and provide a food source to the benthos.

2.8. Scope of this work

The objective of this thesis is to investigate the spatial variability of light conditions under sea ice during summer. This includes an analysis of the main factors governing the spatial variability and their spatial influence on the light field as well as the investigation of the capabilities and weaknesses of different optical sensors in determining this spatial variability. To do so, we make use of novel measurements conducted using a remotely operated vehicle underneath Arctic sea ice. To better understand the light field underneath sea ice, the influence of inherent optical properties linked to the crystal structure of sea ice on the angular radiance distribution is analyzed in field measurements as well as lab and radiative transfer model experiments. This work leads towards a better understanding of the influence of spatial variability of ice optical properties on the large scale energy balance as well as improved parameterizations of light

transmission in sea ice models but also for the light based calculation of Arctic primary production. This thesis also contributes to the investigation of the interdisciplinary research question of the spatial distribution of under-ice algal aggregates that can be addressed using the spatial datasets acquired with remotely operated vehicles.

The work was started with the establishment of the development of the methodology. A description of the developed methods of under-ice surveys using ROVs as well as first data analysis is shown in Paper 5 (MAPPING RADIATION TRANSFER THROUGH SEA ICE USING A REMOTELY OPERATED VEHICLE (ROV)) for the observations conducted with an observation class ROV in 2011 and 2012.

Paper 6 (CHANGES IN ARCTIC SEA ICE RESULT IN INCREASING LIGHT TRANSMITTANCE AND ABSORPTION) analyzes the ROV data acquired during the measurement campaign in 2011 and presents the observation that the changing properties of the Arctic sea ice cover lead to a threefold increase of light transmission through sea ice. While Paper 6 already presents the first map of under-ice light conditions, a precise description and analysis of the factors influencing the spatial variability of light transmission through sea ice on the basis of spatially distributed and co-registered measurements of light transmittance, sea ice topography and surface properties conducted during the NUI campaign in 2014 is given in **Paper 1** (INFLUENCE OF ICE THICKNESS AND SURFACE PROPERTIES ON LIGHT TRANSMISSION THROUGH ARCTIC SEA ICE).

A more theoretical approach is taken in **Paper 2** (GEOMETRIC EFFECTS OF AN INHOMOGENEOUS SEA ICE COVER ON THE UNDER ICE LIGHT FIELD) where the impacts of the horizontally inhomogeneous sea ice cover on light measurements obtained with different sensor types underneath sea ice are investigated to aid processing and interpretation of under ice light measurements. This work is complemented by an investigation of the dependence of the under-ice angular radiance distribution on the crystal structure of sea ice presented in **Paper 3** (THE ANISOTROPIC SCATTERING COEFFICIENT OF SEA ICE). By analysis of optical field measurements taken in 2012 in combination with results of lab experiments and radiative transfer modeling a link between anisotropic inherent optical properties and the propagation of spatially variable light fields to depth under sea ice is established.

In Paper 7 (PHOTOSYNTHETIC PRODUCTION IN THE CENTRAL ARCTIC DURING THE RECORD SEA-ICE MINIMUM IN 2012) the acquired knowledge about radiative transfer processes in the complex ice cover is used for the formulation of a simplified radiative

transfer scheme specifically adapted for the sea ice environment and the purpose of calculating arctic-wide primary production on the basis of measured or remotely sensed incoming solar radiation and photosynthesis versus irradiance curves obtained by collaborating biologists. The model was evaluated against several others in the course of the primary productivity algorithm round robins. The results presented in Paper 8 (AN ASSESSMENT OF OCEAN COLOR MODEL ESTIMATES OF PRIMARY PRODUCTIVITY IN THE ARCTIC OCEAN) show that the model - despite its simplicity - is competitive in the field of mostly more complex algorithms even in the ice-free areas which it was never designed for.

The highly interdisciplinary effort of Paper 9 (EXPORT OF ALGAL BIOMASS FROM THE MELTING ARCTIC SEA ICE) discovered evidence of a strong cryo-pelagic coupling between sea ice and sea floor mediated by macroscopic algal aggregates. The ROV system used in 2012 provides a great platform to combine the light transmission data with a quantitative analysis of the abundance of under-ice algal aggregates. These efforts are further developed to provide the first investigation of the spatial variability of these algal aggregates in Paper 10 (FLOATING ICE-ALGAL AGGREGATES BELOW MELTING ARCTIC SEA ICE). **Paper 4** (DISTRIBUTION OF ALGAL AGGREGATES UNDER SUMMER SEA ICE IN THE CENTRAL ARCTIC) provides a more detailed evaluation of the physical drivers of the spatial distribution of the algal aggregates both on floe scale and throughout the Eurasian part of the Arctic Ocean.

2.9. List of relevant papers

First author papers (full papers included in the following):

Paper 1:

Influence of ice thickness and surface properties on light transmission through Arctic sea ice

Christian Katlein, Stefanie Arndt, Marcel Nicolaus, Donald K. Perovich, Michael V. Jakuba, Stefano Suman, Stephen Elliott, Louis L. Whitcomb, Christopher J. McFarland, Rüdiger Gerdes, Antje Boetius, Christopher R. German, *under review in Journal of Geophysical Research* (2015)

Contribution: I participated in the field work, leading the sea ice work. I performed the data analysis presented in the manuscript and assisted in reprocessing of the NUI vehicle navigation and multibeam data. I wrote the text and prepared all figures during a research stay visiting Prof. Donald K. Perovich. The manuscript is submitted for publication in the *Journal of Geophysical Research*.

Paper 2:

Geometric effects of an inhomogeneous sea ice cover on the under ice light field

Christian Katlein, Donald K. Perovich, Marcel Nicolaus, *submitted to Frontiers in Earth Science: Cryospheric Sciences* (2015)

Contribution: As first author I had the idea, developed the theoretical frame, implemented the numerical model and performed all calculations. I wrote the text and prepared all figures during a research stay visiting Prof. Donald K. Perovich who discussed the topic with me and contributed to the development and writing of the text. The manuscript is submitted for publication in *Frontiers in Earth Science: Cryospheric Sciences*.

Paper 3:

The anisotropic scattering coefficient of sea ice

Christian Katlein, Marcel Nicolaus, and Chris Petrich, *Journal of Geophysical Research – Oceans, 119*, doi:10.1002/2013JC009502, (2014)

Contribution: As first author I had the idea, developed the theoretical frame and conducted the field and lab work, as well as the numerical modeling. Chris Petrich provided the core code of the radiative transfer model. I wrote the text and prepared all figures. All authors provided guidance and comments during the writing process. The paper is published in the *Journal of Geophysical Research*.

Paper 4:

Distribution of algal aggregates under summer sea ice in the Central Arctic

Christian Katlein, Mar Fernández-Méndez, Frank Wenzhöfer, Marcel Nicolaus, *Polar Biology*, doi:10.10007/s00300-014-1634-3, (2014)

Contribution: I developed the image analysis algorithm and performed the field work. An intern student validated the automated aggregate detection under my supervision, all further analysis was performed by myself. Mar Fernández-Méndez and Frank Wenzhöfer provided biological background information. I wrote the text and prepared all figures. The paper is published in the journal *Polar Biology*.

2.10. Contributions as Co-Author

Papers are not included in the following, but listed including the abstract and a description of my respective contribution:

Paper 5:

MAPPING RADIATION TRANSFER THROUGH SEA ICE USING A REMOTELY OPERATED VEHICLE (ROV), Marcel Nicolaus, **Christian Katlein**, *The Cryosphere*, doi:10.5194/tc-7-763-2013, (2013)

Abstract:
Transmission of sunlight into and through sea ice is of critical importance for sea-ice associated organisms and photosynthesis because light is their primary energy source. The amount of visible light transferred through sea ice contributes to the energy budget of the sea ice and the uppermost ocean. However, our current knowledge on the amount and distribution of light under sea ice is still restricted to a few local observations, and our understanding of light-driven processes and interdisciplinary interactions is still sparse. The main reasons are that the under-ice environment is difficult to access and that measurements require large logistical and instrumental efforts. Hence, it has not been possible to map light conditions under sea ice over larger areas and to quantify spatial variability on different scales. Here we present a detailed methodological description for operating spectral radiometers on a remotely operated vehicle (ROV) under sea ice. Recent advances in ROV and radiation-sensor technology have allowed us to map under-ice spectral radiance and irradiance on floe scales within a few hours of station time. The ROV was operated directly from the sea ice, allowing for direct relations of optical properties to other sea-ice and surface features. The ROV was flown close to the sea ice in order to capture small-scale variability. Results from the presented data set and similar future studies will allow for better quantification of light conditions under sea ice. The presented experiences will support further developments in order to gather large data sets of under-ice radiation for different ice conditions and during different seasons.

Contribution:
I participated in the field work and contributed to the development of the method. I performed most of the data analysis during my diploma thesis, but some of the writing as well as the work on revisions also including additional

simulations of sensor response falls into the timeframe of my PhD project. I contributed to the writing of the manuscript and crafted several of the figures

Paper 6:

CHANGES IN ARCTIC SEA ICE RESULT IN INCREASING LIGHT TRANSMITTANCE AND ABSORPTION, Marcel Nicolaus, **Christian Katlein**, James Maslanik, Stefan Hendricks, *Geophysical Research Letters, doi:10.1029/2012GL053738,* (2012)

Abstract:
Arctic sea ice has declined and become thinner and younger (more seasonal) during the last decade. One consequence of this is that the surface energy budget of the Arctic Ocean is changing. While the role of surface albedo has been studied intensively, it is still widely unknown how much light penetrates through sea ice into the upper ocean, affecting sea-ice mass balance, ecosystems, and geochemical processes. Here we present the first large-scale under-ice light measurements, operating spectral radiometers on a remotely operated vehicle (ROV) under Arctic sea ice in summer. This data set is used to produce an Arctic-wide map of light distribution under summer sea ice. Our results show that transmittance through first-year ice (FYI, 0.11) was almost three times larger than through multi-year ice (MYI, 0.04), and that this is mostly caused by the larger melt-pond coverage of FYI (42 vs. 23%). Also energy absorption was 50% larger in FYI than in MYI. Thus, a continuation of the observed sea-ice changes will increase the amount of light penetrating into the Arctic Ocean, enhancing sea-ice melt and affecting sea-ice and upper-ocean ecosystems.

Contribution:
I participated in the field work and performed the analysis of the field data during my diploma thesis. I contributed to the writing of the manuscript and the preparation of the figures. The work on manuscript revisions after initial submission where I provided comments, falls into the time frame of my PhD thesis.

Paper 7:

Abstract:

The ice-covered Central Arctic Ocean is characterized by low primary productivity due to light and nutrient limitations. The recent reduction in ice cover has the potential to substantially increase phytoplankton primary production, but little is yet known about the fate of the ice-associated primary production and of the nutrient supply with increasing warming. This study presents results from the Central Arctic Ocean collected during summer 2012, when sea-ice reached a minimum extent since the onset of satellite observations. Net primary productivity (NPP) was measured in the water column, sea ice and melt ponds by $^{14}CO_2$ uptake at different irradiances. Photosynthesis vs. irradiance (PI) curves were established in laboratory experiments and used to upscale measured NPP to the deep Eurasian Basin (north of 78° N) using the irradiance-based Central Arctic Ocean Primary Productivity (CAOPP) model. In addition, new annual production was calculated from the seasonal nutrient drawdown in the mixed layer since last winter. Results show that ice algae can contribute up to 60% to primary production in the Central Arctic at the end of the season. The ice-covered water column has lower NPP rates than open water due to light limitation. As indicated by the nutrient ratios in the euphotic zone, nitrate was limiting primary production in the deep Eurasian Basin close to the Laptev Sea area, while silicate was the main limiting nutrient at the ice margin near the Atlantic inflow. Although sea-ice cover was substantially reduced in 2012, total annual new production in the Eurasian Basin was 177 TgCyr^{-1}, which is within the range of estimates of previous years. However, when adding the contribution by sub-ice algae, the annual production for the deep Eurasian Basin (north of 78° N) could double previous estimates for that area with a surplus of 16 TgCyr^{-1}. Our data suggest that sub-ice algae are an important component of the ice-covered Central Arctic productivity. It remains an important question if their contribution to productivity is on the rise with thinning ice, or if it will decline due to overall sea-ice retreat and be replaced by phytoplankton.

Contribution:

I participated in the sea-ice-physics part of the field work and assisted with the analysis of biological data, fitting the measured PI-curves. In collaboration with Mar Fernández-Méndez I developed and implemented the CAOPP upscaling-model for estimation of in and under-ice primary productivity, based on the available light. I performed all the model related calculations and analysis of output data. I provided figures and contributed to the writing of the manuscript. The manuscript is published in *Biogeosciences*.

Paper 8:

An assessment of ocean color model estimates of primary productivity in the Arctic Ocean

Younjoo J. Lee, Patricia A. Matrai, Marjorie A. M. Friedrichs, Vincent S. Saba, David Antoine, Ichio Asanuma, Simon Bélanger, Mar Fernández-Méndez, **Christian Katlein**, Toru Hirawake, Takahiko Kameda, Zhongping Lee, Frederic Mélin, Michele Scardi, Tim Smyth, Shilin Tang, Kevin Turpie, Kirk Waters, and Toby Westberry, under review for *Journal of Geophysical Research*, June 2015

Abstract:

We investigated the skill of 32 ocean color models by assessing their ability to reproduce the mean and variability of integrated net primary productivity (NPP) relative to in situ measurements in the Arctic Ocean during 1988-2011. Models were provided with surface chlorophyll-a, photosynthetically available radiation (PAR), sea surface temperature (SST), mixed-layer depth (MLD), and other satellite-derived properties. The models were most sensitive to the source of surface chlorophyll data, generally performing better with satellite than in situ chlorophyll, but much less sensitive to the source of PAR, SST, and MLD data. Regardless of model type or complexity, most models significantly underestimated the variability of NPP, often by more than a factor of two, whereas some models exhibited almost no bias. Although the model performance varied seasonally and regionally, most models overestimated the mean NPP (i.e., positive bias) in low-productivity regions/seasons and underestimated the mean NPP (i.e., negative bias) in high-productivity regions/seasons. Depth-resolved models had a strong tendency to overestimate the mean NPP compared to the depth-integrated models, and absorption-based models exhibited low bias and/or high standard deviation. The models performed better with in situ chlorophyll when no subsurface chlorophyll-a maximum was present, but mean NPP was still overestimated, which may be offset by underestimation of NPP due to the absence of subsurface chlorophyll-a maximum or dampened by averaging temporally on a pan-Arctic scale. Our study suggests that ocean color models need to be tuned to the Arctic Ocean because most models that performed well in estimating NPP were those developed or modified specifically for the Arctic region. Furthermore, the future success of ocean color models in estimating NPP relies on the substantial improvement of the algorithms that derive surface chlorophyll from satellite measurements of ocean color.

Contribution:

I developed and implemented the CAOPP upscaling-model for estimation of in and under-ice primary productivity based on the available light in collaboration with Mar Fernández-Méndez. I performed the model calculations of the PPARR5 scenarios and provided a description of the model. Analysis of the output data and model intercomparison was performed by Y. Lee. I contributed to the writing of the manuscript. The manuscript is submitted for publication in *Journal of Geophysical Research*.

Paper 9:

Export of Algal Biomass from the Melting Arctic Sea Ice, Antje Boetius, Sebastian Albrecht, Karel Bakker, Christina Bienhold, Janine Felden, Mar Fernández-Méndez, Stefan Hendricks, **Christian Katlein**, Catherine Lalande, Thomas Krumpen, Marcel Nicolaus, Ilka Peeken, Benjamin Rabe, Antonina Rogacheva, Elena Rybakova, Raquel Somavilla, Frank Wenzhöfer, RV Polarstern ARK27-3-Shipboard Science Party, *Science*, doi:10.1126/science.1231346, (2013)

Abstract:
In the Arctic, under-ice primary production is limited to summer months and is restricted not only by ice thickness and snow cover but also by the stratification of the water column, which constrains nutrient supply for algal growth. Research Vessel Polarstern visited the ice-covered eastern-central basins between 82° to 89°N and 30° to 130°E in summer 2012, when Arctic sea ice declined to a record minimum. During this cruise, we observed a widespread deposition of ice algal biomass of on average 9 grams of carbon per square meter to the deep-sea floor of the central Arctic basins. Data from this cruise will contribute to assessing the effect of current climate change on Arctic productivity, biodiversity, and ecological function.

Contribution:
I participated in the field work onboard RV Polarstern, analysed the ROV data and provided the first analysis of algal aggregate abundance underneath the ice using an early version of the aggregate detection algorithm. I contributed during the writing and revisions of the manuscript.

Paper 10:

Abstract:
During two consecutive cruises to the Eastern Central Arctic in late summer 2012, we observed floating algal aggregates in the melt-water layer below and between melting ice floes of first-year pack ice. The macroscopic (1-15 cm in diameter) aggregates had a mucous consistency and were dominated by typical ice-associated pennate diatoms embedded within the mucous matrix. Aggregates maintained buoyancy and accumulated just above a strong pycnocline that separated meltwater and seawater layers. We were able, for the first time, to obtain quantitative abundance and biomass estimates of these aggregates. Although their biomass and production on a square metre basis was small compared to ice-algal blooms, the floating ice-algal aggregates supported high levels of biological activity on the scale of the individual aggregate. In addition they constituted a food source for the ice-associated fauna as revealed by pigments indicative of zooplankton grazing, high abundance of naked ciliates, and ice amphipods associated with them. During the Arctic melt season, these floating aggregates likely play an important ecological role in an otherwise impoverished near-surface sea ice environment. Our findings provide important observations and measurements of a unique aggregate-based habitat during the 2012 record sea ice minimum year.

Contribution:
I participated in the field work onboard RV Polarstern, analysed the ROV data and provided the first analysis of algal aggregate abundance underneath the ice using an early version of the aggregate detection algorithm. This includes the contribution of one figure showing the first map of the spatial distribution of algal aggregates, as well as upscaling calculations. I contributed to the writing and the revisions of the manuscript.

3. Paper 1

INFLUENCE OF ICE THICKNESS AND SURFACE PROPERTIES ON LIGHT TRANSMISSION THROUGH ARCTIC SEA ICE

Christian Katlein[1],Stefanie Arndt[1], Marcel Nicolaus[1], Donald K. Perovich[2], Michael V. Jakuba[3], Stefano Suman[3], Stephen Elliott[3], Louis L. Whitcomb[3,4], Christopher J. McFarland[4], Rüdiger Gerdes[1], Antje Boetius[1,5], Christopher R. German[3]

[1]Alfred-Wegener-Institut Helmholtz-Zentrum für Polar- und Meeresforschung, Bussestr. 24, 27570 Bremerhaven, Germany

[2]Cold Regions Research and Engineering Laboratory, Hanover, New Hampshire, USA

[3]Woods Hole Oceanographic Institution, Woods Hole, Massachusetts, USA

[4]Johns Hopkins University, Baltimore, Maryland, USA

[5]Max Planck Institute for Marine Microbiology, Bremen, Germany

Abstract

The observed changes in physical properties of sea ice such as decreased thickness and increased melt pond cover severely impact the energy budget of Arctic sea ice. Increased light transmission leads to increased deposition of solar energy in the upper ocean and thus plays a crucial role for amount and timing of sea-ice-melt and under-ice primary production. Recent developments in underwater technology provide new opportunities to study light transmission below the largely inaccessible underside of sea ice. We measured spectral under-ice radiance and irradiance using the new Nereid Under-Ice (NUI) underwater robotic vehicle, during a cruise of the R/V Polarstern to 83°N 6°W in the Arctic Ocean in July 2014. NUI is a next generation hybrid remotely operated vehicle (H-ROV) designed for both remotely-piloted and autonomous surveys underneath land-fast and moving sea ice. Here we present results from one of the first comprehensive scientific dives of NUI employing its interdisciplinary sensor suite. We combine under-ice optical measurements with three dimensional under-ice topography (multibeam sonar) and aerial images of the surface conditions. We investigate the influence of spatially varying ice-thickness and surface properties on the spatial variability of light transmittance during summer. Our results show that surface properties such as melt ponds dominate the spatial distribution of the under-ice light field on small scales (<1000m²), while sea ice-thickness is the most important predictor for light transmission on larger scales. In addition, we propose the use of an algorithm to obtain histograms of light transmission from distributions of sea ice thickness and surface albedo.

Key points

- Surface properties of sea ice strongly influence the light field on local scales

- Large scale variability of under ice light is determined by ice thickness

- Light transmittance can be inferred from thickness and albedo distribution

1. Introduction

The sea ice cover of the Arctic Ocean has significantly decreased in the last decades [*Meier et al.*, 2014; *Perovich*, 2011] by extent [*Serreze et al.*, 2007; *Stroeve et al.*, 2007; *Stroeve et al.*, 2012] and in thickness [*Haas et al.*, 2008; *Kwok and Rothrock*, 2009; *Renner et al.*, 2014; *Rothrock et al.*, 2008]. Changed surface properties, such as the increased formation of melt ponds [*Rösel and Kaleschke*, 2012], and the shift from multi-year sea ice to predominantly first-year sea ice in vast regions of the Arctic [*Maslanik et al.*, 2011; *Tschudi et al.*, 2010], led to increased light transmission through the sea ice in spring and summer [*Nicolaus et al.*, 2012; *Perovich et al.*, 2011]. Yet detailed knowledge of the physical processes governing the fate of the sea ice is limited [*Perovich and Polashenski*, 2012; *Perovich et al.*, 2002], especially with regard to the role of small- to meso-scale melting processes. In the last half-century knowledge about vertical gradients of physical and biological environmental properties depended on ice cores and instruments lowered on a wire [*Frey et al.*, 2011; *Grenfell*, 1977; *Light et al.*, 2003b; *Thomas and Dieckmann*, 2010; *Zeebe et al.*, 1996], with limitations for regional upscaling. Airborne and satellite remote sensing as well as new tools for field investigations improved the study of spatially distributed processes at the ice surface [*Hudson et al.*, 2012; *Perovich et al.*, 1998a; *Petrich et al.*, 2012b], but only recently advances in the field of marine robotics allow comprehensive large scale studies underneath the polar pack ice [*Bowen et al.*, 2012; *Jakuba et al.*, 2008; *Kukulya et al.*, 2010; *Nicolaus and Katlein*, 2013; *Williams et al.*, 2013] that allow for Arctic wide upscaling [*Arndt and Nicolaus*, 2014].

One process of particular interest both for sea ice physics and biology is the partitioning of solar shortwave radiation at the sea ice surface [*Light et al.*, 2008; *Perovich et al.*, 2011]. In winter and spring, the snow cover on the ice limits light transmission and determines its spatial variability [*Mundy et al.*, 2005]. As Arctic sea ice gets increasingly translucent over the course of the season, the fraction of the solar flux absorbed in the ice [*Nicolaus et al.*, 2013a] and the water layer right beneath can sustain algal productivity and cause substantial sea ice melt. This solar heat flux can easily dominate over the ocean heat flux contribution to ice melt during summer [*Hudson et al.*, 2013; *Nicolaus et al.*, 2013b]. Nevertheless, shortwave radiative transfer in sea ice is often poorly represented in sea ice ocean models due to its complexity and high spatial variability on a scale smaller than the model resolution.

While the quantitative impact of the physical sea-ice properties on light transmittance is well understood for the text-book case of one-dimensional homogenous horizontal layers [*Light et al.*, 2008; *Perovich*, 1996; *Perovich et al.*, 1998a], the influence of surface features and the three-dimensional ice-topography is poorly quantified for the pack ice of the Central Arctic where these factors vary on spatial scales of just a few meters.

The objective of this paper is to analyze the influence of the spatially varying surface properties of the sea ice cover and sea ice thickness on the spatial variability of light transmittance. The respective contribution of the two variables is assessed quantitatively on the basis of a survey conducted by the new Nereid Under-Ice (NUI) hybrid remotely operated vehicle coordinated with co-registered aerial images and classical sea ice observations. This novel approach using spatially distributed measurements overcomes the limitations of one-dimensional modeling and data analysis.

2. Methods

2.1. Sampling site

Measurements were carried out during the expedition of the German research ice-breaker *RV Polarstern* to the Aurora mount, a hydrothermal vent site at Gakkel Ridge off Northeast Greenland (Figure 1a) [*Boetius*, 2015]. The described sea ice floe was surveyed on station PS86/080 at 82° 51' N and 6° 19' W on 28 July 2014 by on-site ice-thickness drillings combined with an under-ice survey of NUI and aerial images taken during a helicopter survey. Snow thickness was measured using a MagnaProbe (Snow Hydro, Fairbanks, AK, USA). During the study, air temperature was slightly below 0°C, the average sea ice drift velocity was 0.3 kn, and ice concentration was 80%.

2.1. Vehicle and sensors

The Nereid Under Ice (NUI) vehicle (Figure 1b) is a hybrid remotely operated vehicle, designed especially for surveys in ice-covered waters [*Bowen et al.*, 2012; *Bowen et al.*, 2014; *Jakuba et al.*, 2008]. While offering the inspection and intervention capabilities of a conventional remotely operated vehicle (ROV), the light-fiber tether concept allows the vehicle to operate in a drifting sea ice environment at increased standoff distances of in principle up to 20 km from the support vessel. In the event of failure of the light fiber-optic tether, high-bandwith optical communication to the vehicle is lost, and the vehicle enters a

semi-autonomous mode in which it communicates to the ship via low-bandwidth acoustic telemetry through the water-column. In this mode the operators can send acoustic commands to the vehicle to guide it back to the ship for recovery. NUI is a recent development of the Deep Submergence Laboratory at the Woods Hole Oceanographic Institution (Woods Hole, MA, USA) in collaboration with the Johns Hopkins University (Baltimore, MD, USA). The vehicle provides space, power and communication for various payloads. Vehicle position data is determined by the navigation software via dead reckoning using a combination tracking of the ice bottom by upward-looking doppler velocity log (DVL), and ship-relative acoustic long baseline (LBL) positioning [*McFarland et al.*, 2015].

Downwelling under-ice spectral irradiance and spectral zenith radiance (both 320-950 nm) were measured using two RAMSES-ACC/ARC (Trios GmbH, Rastede Germany) sensors positioned in the spine payload bay of the NUI vehicle. Here we present broadband values integrated over the 320-950 nm band after interpolation to a spectral resolution of 1 nm [*Nicolaus et al.*, 2010a]. The sensors were positioned approximately 0.5 m above the vehicle's depth sensor and triggered at the fastest achievable sampling rate, in most cases 0.5Hz, leading to a spatial resolution of approximately 0.3m during the under-ice survey. The field of view of the radiance sensor is 9.3° pointing towards zenith resulting in a mean footprint of 0.23m at the underside of the ice varying with the sensor distance to the ice. Processing of the optical data as well as the calculation of transmittance (transflectance) as the quotient of under-ice irradiance (radiance) and the surface reference measurement has been described in *Nicolaus et al.* [2010a] and *Nicolaus and Katlein* [2013]. Zenith radiance measurements were scaled with a factor 2.5 assuming isotropic scattering in the ice according to *Katlein et al.* [2014] to be comparable to irradiance measurements. Incident solar irradiance was measured with a reference sensor (RAMSES-ACC) located in the crowsnest of the ship. Due to low stratus clouds, incident light conditions exhibited very little variation and effects of shading by the ship's superstructure are negligible.

Sea-ice draft was measured as the difference between the vehicle depth and its distance to the ice bottom. The distance to the ice was measured by the upward-looking navigation DVL throughout the whole survey. During the last part of the survey, an upward-looking 260kHz Delta T multibeam sonar (Imagenex Technology Corp., Port Coquitlam, BC, Canada) provided three-dimensional measurements of the ice bottom topography. We chose not to convert draft measurements into ice thickness, as ice thickness and draft values measured by

drillings showed that the isostatic equilibrium were not valid for most single point measurements.

To register the sub-ice dataset with the aerial image and to ground-truth ice draft measurements, 6 holes of ~5cm diameter were drilled through the ice along a 90 m transect. The locations of the holes in the ice were marked with red marker paint to ease location in the aerial images. After measuring sea-ice thickness and draft with an ice-thickness gauge (Kovacs Entreprise Inc., Roseburg , OR, USA) we deployed 1m long red-white colored marking poles hanging underneath the sea ice from ropes at ~4m depth. These poles were detectable in the 900 kHz forward looking obstacle avoidance and imaging P900 BlueView sonar (Teledyne BlueView, Bothell, WA, USA). Bearing and range from the vehicle to the closest pole were extracted from the BlueView images to establish exact positions of the poles in the coordinate system of the NUI navigation. The dead reckoning throughout the entire 2 km long trackline (Figure 2a) suffers from rotation of the ice floe and other undetermined navigation errors, so that the measurements cannot be co-located with the surface measurements. In contrast, the known position relative to the poles during the last 100m before the survey end allows for a position accuracy of better than 1m for this 100m transect and thus the ability to co-locate surface measurements and aerial images. The last part of the survey, conducted at a constant vehicle depth of 5m will be referred to as the pole survey throughout the rest of this paper.

2.3. Aerial images

Aerial images were obtained on four parallel low altitude flight lines using a downward looking GoPro digital camera (GoPro Hero 3 Black Edition, GoPro Inc., San Mateo, CA, USA) mounted to a helicopter. Images were corrected for camera distortion and merged to a photomosaic using Adobe Photoshop (Figure 2a). It was not possible to acquire higher quality images from higher altitude (>75 m) due to low clouds.

Melt ponds in the image were detected using a manually drawn mask of the floe and threshold values determined from a training dataset. All pixels on the floe, where $mean(R, G, B) < 70 + 0.5 \cdot B$ were classified as melt pond (Figure 2b) with R, G, B the integer values of the respective channels of the RGB color space Rec. 709 (R=700nm, G=525nm, B=450nm).

To obtain a co-located aerial image, one of the images taken by the GoPro camera covering the entire area of the pole survey with least possible distortion was selected and corrected for lens distortion and vignetting. The vehicle track

obtained from dead reckoning was projected to image coordinates using the marker coordinates as ground control points in a similarity transform (scale and rotate). Quantitative information about the surface conditions could thus be deduced along the vehicle track from the aerial image.

From the three RGB channels, we constructed pixel brightness by dividing the intensity (mean of R, G and B) through the maximum value of 255. This brightness value ranges between 0 and 1 and represents a proxy for surface albedo, recognizing that this study is most interested in assessing spatial variability and does not require fully calibrated albedo measurements. Extracted albedo values are similar to those generally observed on Arctic sea ice [*Perovich*, 1996] with values between 0.55 and 0.6 for melting white ice and 0.3 to 0.4 for melt-ponds. Albedo values were extracted along the vehicle track, both as single pixel values and as averages over albedo values in a circle around the vehicle position with a diameter of 2m, 4m and 6m. This averaging accounts for effects of lateral spreading of light by scattering in the ice as well as the large field of view of the irradiance sensor.

2.4. Analysis

From all the data available for the pole survey, we constructed a dataset of simultaneous measurements of under-ice irradiance, radiance, ice draft derived from the DVL range, ice draft derived from the multi-beam sonar, as well as point and spatially averaged albedo. This dataset was transferred into the statistical software R to analyze the multi-variate dependencies and to determine the variability explained by each variable.

To analyze the scales of spatial variability, we computed and fitted spatial variograms (Figure 4). The empirical variogram describes the variance in subsets of the dataset with varying spatial distance (lag distance). Empirical variograms were fitted with exponential theoretical variograms to obtain range values. The range parameter is defined as the lag distance at which the fitted variogram reaches ~95% of the sill value, the asymptotic variance of unrelated datapoints with large distance. Thus it describes the scale of the distance at which datapoints are related to each other.

3. Results

3.1. Physical properties of the ice floe

The surveyed ice floe was of large extent (> 1 km²) and had a modal ice draft of 1.6m. It consisted of several parts of rather undeformed first- or second-year ice as well as heavily deformed parts. While the level ice was mostly covered by extensive melt ponds between old and young ridges, the more deformed ice also hosted isolated lighter-blue ponds (Figure 2a).

The floe surface was in an intermediate melting stage showing various stages of melt pond development. The ice surface was covered by a layer of large grains resembling wet melting snow, but also very similar to the surface scattering layer present on summer sea ice. The modal thickness of the surface layer was 8cm. In large areas, especially adjacent to some melt ponds, the surface layer was partly saturated with water. Analysis of the aerial image revealed, that 13% of the floe was covered by melt-ponds. The length scale of melt pond variability on the floe was 9.3m as determined by variogram analysis of the classified aerial image (range value). The thick ice, the considerable surface layer, the geographic position close to Greenland and the timing early in the melting season are the reason for the low light transmittances when compared to other studies from other regions or later in the summer [*Arrigo et al.*, 2012; *Nicolaus et al.*, 2012].

3.2. Pole survey

Results from the pole survey transect are shown in Figure 3. Light transmittance was between 0.02 and 0.10 along the transect: In the vicinity of the first pole, light transmittance was high due to a melt pond, but it dropped quickly under the influence of a ridge visible on the surface. After crossing the ridge, light levels increased due to a reduction in ice draft from 2m to 1.2m before dropping again due to the thickest ice observed in the transect, between poles 2 and 3 with a draft of up to 2.5m. The two clear peaks of light-transmittance near poles 4 and 5, respectively can be attributed to the crossing beneath two melt ponds at the surface (Figure 3a). The final increase at the end of the survey is caused by the approach to a third, larger melt pond.

A noteworthy feature of the multibeam ice draft measurements is that the under-ice topography might deviate substantially from what would be expected when looking at the surface structure. Ridges visible at the surface do not necessarily have keels visible at the underside of the ice while ice features with

greater thickness do not necessarily have to be represented in the surface topography (Figure 3b). This can lead to confusion when navigating under-ice vehicles according to features visible on the surface.

Extracted albedo values lie between 0.3 and 0.6. Spatial averaging of albedo values over circles of increasing diameter shows the strength of the influence of the pond geometries on either side of the vehicle track on optical properties (Figure 3c).

Ice draft varies between 1.0m and 2.3m along the transect (Figure 3d). Multibeam draft data agree well with draft data acquired from the DVL when the different methods of calculation are taken into consideration. The DVL range is calculated as the average range of 4 beams angled 30° from vertical, thus averaging over an area of 1m to 3m depending on the distance between instrument and ice. Comparison of the multibeam draft data with ice draft measured at the positions of the poles revealed an accuracy of <0.1m for the ice topography, similar to what has been achieved earlier [*Wadhams et al.*, 2006; *Williams et al.*, 2015].

Light transmittance as observed from the irradiance and radiance sensors is clearly related to both surface albedo and ice draft. The peaks of light transmittance related to drops in the surface albedo caused by melt ponds are particularly obvious (Figure 3c and 3e).

Statistical analysis of the resulting dataset reveals that 72% percent of the variance in the measured radiance can be explained by the combination of the 1m albedo average (65%) and the ice-draft value at the spot (7%). All other combinations of the available variables described a smaller portion of the observed variance. While radiance measurements thus seem to be mostly influenced by the ice properties at the spot, irradiance measurements are influenced by albedo and ice thickness over a larger region in the vicinity of the measurement. Thus a combination of the 3m albedo average and the draft measured from the DVL representing a spatial average of 1-3m explains 66% percent of the variance in measured irradiance.

The contrast in peakiness between the different measured light transmission curves (Figure 3c) shows that the smooth contrasts of irradiance are mainly caused by the large sensor footprint and not by lateral light propagation in the ice. If lateral light propagation were the dominant cause, then the radiance profile would be comparable in smoothness to the irradiance profile.

3.3. Scales of spatial variability

To investigate the length scales of the spatial variability of different variables, variograms were computed for the available dataset of albedo, ice draft and light transmittance (Figure 4). The variograms were computed each for both the dataset of the whole dive survey and a subset covering the pole survey only. The typical length scale of albedo variability was 10.6m for the whole dive and 8.4m for the pole survey. This comes from the typical size range of melt ponds which cause the highest variations in surface albedo. For sea ice draft we considered only the DVL data, as the multibeam data is not available for the entire dive. We derived length scales of ice-draft variability ranging from 15.1m for the whole dive to 26.8m for the pole transect. This is significantly greater than the length scale of a typical pond at this time of the year. The length scale of the variability of light transmittance was 8.4m on the pole survey and 16.6m when considering the whole floe, indicating different causes for the observed variability on different scales.

3.4. From point measurements to histograms

A great advantage of spatially extensive measurements is the ability to construct histograms showing the distribution of measured values in contrast to single point values. While this technique of histograms has been used frequently for ice-thickness distributions [*Thorndike et al.*, 1975] its application to optical properties has only begun recently, triggered by the development of relevant sampling methods [*Divine et al.*, 2015; *Nicolaus et al.*, 2012; *Nicolaus et al.*, 2013a].

Figure 5a shows the frequency distribution of surface albedo pixels as derived from the aerial image. A clear bimodal distribution is visible, but the wide variety of ponds on the floe causes a wide saddle in between the two peaks related to melt ponds and bare ice respectively. Associating the albedo values with their respective surface type retrieved from color thresholding, shows that a portion of bright light blue ponds is "leaking" into the peak associated with bare sea ice.

The ice draft distribution shows differences between the two instruments related to the different sampling areas (Figure 5b). While the DVL dataset covering the whole dive shows a unimodal distribution with a modal ice draft of ~1.7 m, the multibeam data covering only the pole transect shows a bimodal distribution with a consistent mode at ~1.7 m and a local mode of thinner ice at ~1.2 m.

Bulk light extinction coefficients κ computed from light transmittance T and ice draft z_i ($\kappa = -\ln\left(\frac{T}{z_d}\right)$) show a mode centered around 1.8 m^{-1} but also significantly higher values (Figure 5c). The light transmittance distribution is primarily unimodal with a modal transmittance between 0.03 and 0.04 evident from both sensors (Figure 5d). In addition, both sensors show a small secondary mode of dark patches below 0.01. Low light transmittance occurs more frequently in the radiance data as measurements at dark spots are not influenced by adjacent ponds. The tail of the distribution is longer (maximum 0.12) for the radiance sensor than for the irradiance sensor (maximum 0.09). This was expected, as small scale structures with high light transmission such as small ponds, cracks or channels are better represented by the radiance measurements.

4. Discussion

4.1. Light transmission under a spatially varying ice cover

Our results show that 72% of variance in the spatially varying light field underneath the ice can be explained by ice draft and surface albedo, in particular the influence of melt ponds at this time of the year when the snow cover starts to disappear. To describe the variance in the irradiance measurements best, it is necessary to use spatial averages, while the radiance field can be best described using local values. This is due to the irradiance sensor having a larger footprint than the radiance sensor.

Several factors lead to the fact that only 72% of the under-ice light field variance can be explained by surface albedo and ice draft: First, our measurements only include ice draft and not the portion of the ice above the waterline, which can have significant impact on the under ice light and is not necessarily represented in the albedo variability. Second, we were not able to quantify the spatially varying properties of the surface layer. The observed melting stage with properties in between melting snow and surface scattering layer, varied throughout the floe and included water saturation in some places. Third, lateral changes in ice internal properties caused by different stages of melt are hard to quantify. These poorly quantifiable factors can easily explain the 28% of unexplained variance in the under ice light field.

While the irradiance curve is very smooth, the radiance curve shows clearly accented peaks (Figure 3e). This shows that the smoothness of the irradiance curve is caused by measurement geometry and the large sensor footprint

resulting from the sensor not being placed exactly at the ice water interface. Lateral propagation of light due to scattering in the ice is thus not the primary cause for smoothing of the irradiance curve.

Our results show that a one-dimensional approach is not enough for modeling under ice irradiance measurements as the large sensor footprint results in a significant influence of adjacent structures on the measurements. This is also the case to a lesser extent for radiance measurements, as light measured at one point immediately against the underside of the sea ice will still be influenced by optical conditions within a certain area above the point due to lateral transport of light by scattering in the ice [*Petrich et al.*, 2012a; *Trodahl et al.*, 1987].

4.2. Scales of spatial variability

Analysis of the spatial scales using variograms revealed a characteristic length scale for albedo variations around 10 m, the typical length scale of melt ponds. This is consistent with similar observations by *Petrich et al.* [2012b] on landfast ice. As noted previously by *Perovich et al.* [1998a], this length scale of pond variability is closely linked to the length scale of under ice light variability due to the obvious impact of melt ponds on light transmission [*Nicolaus et al.*, 2012]. We found a characteristic length scale of 8.4 m for the variance in the under ice irradiance measurements along the pole transect, which lies very close to the length scale of pond variability. Surprisingly, the characteristic length scale of under ice light variability obtained from the complete dataset was 16.6m, twice as long as the scale determined during the pole survey. This is significantly bigger than the length scale for melt ponds and lies very close to the length scale of ice draft variability observed during the whole transect of 15.1 m. Thus we suggest that the variability of under ice light is governed by variations in ice draft, when considering areas bigger than 1000 m². On this scale, the variability of the pond cover is averaged spatially. While the presence of ponds will only impact the mean light level, the large scale variability of under ice light is driven by changes in ice thickness which in turn also reflects the variability of ice type, its properties and the pond ratio. This result confirms the feasibility of using ice thickness as a predictor for light transmission in large-scale sea ice models during summer, when the influence of snow cover is limited.

4.3. Describing the light-field by distribution functions

Under ice datasets with large spatial extent can successfully be employed to compute histograms of ice apparent optical properties. Light transmission has

proved to be related to ice draft and surface albedo, both variables for which histograms and distribution functions can be acquired using surface surveys or eventually satellite observations. We thus want to examine the possibility of composing a light transmission histogram from the distributions of surface albedo and ice draft. For reasons of simplicity we here assume that ice draft equals ice thickness, which is a good approximation for the early melting season. Different ice draft to ice thickness relations can be easily implemented analogously.

As the distributions are not completely independent from each other – e.g. ponds occur more often on thinner ice [*Fetterer and Untersteiner*, 1998; *Nicolaus et al.*, 2012] – it is not possible to produce the exact light transmission histogram just out of the two distribution functions. Nevertheless, we propose a method that allows an approximation of the light transmission histogram treating the two distributions as independent or with simply constrained dependence. One argument for considering the distributions of ice draft and surface albedo to be independent is that in many cases, they will be determined by different instruments in slightly differing locations. Similarly it is extremely challenging to produce a combined dataset of under ice and surface observations that are precisely co-located over a large enough area. Thus we will start with a formulation using independent distribution functions:

Let the surface albedo distribution be described by a row of albedo values $[\alpha_1, \alpha_2, …, \alpha_n]$ with occurrence frequencies $[h(\alpha_1), h(\alpha_2), …, h(\alpha_n)]$ complying to the normalization $\sum_{i=1}^{n} h(\alpha_i) = 1$, and the ice thickness distribution as a row of ice thickness values $[z_1, z_2, …, z_m]$ with occurrence frequencies $[g(z_1), g(z_2), …, g(z_m)]$ and $\sum_{i=1}^{m} g(z_i) = 1$. In a simple approach, light transmittance can be calculated from surface albedo α, ice thickness z and a known extinction coefficient κ as follows:

$$T = (1 - \alpha) \exp(-\kappa z) \text{ (2)}$$

This equation can be evaluated for all possible combinations of n and m, yielding transmittance values $T_{1…l} = [T(\alpha_1, z_1), T(\alpha_1, z_2), …, T(\alpha_2, z_1), T(\alpha_2, z_2), …, T(\alpha_n, z_m)]$ and combined occurrence frequencies

$$w_{1…l} = [h(\alpha_1) g(z_1), h(\alpha_1)g(z_2), …, h(\alpha_2)g(z_1), h(\alpha_2)g(z_2), …, h(\alpha_n)g(z_m)]$$

still normalized as $\sum_{i=1, j=1}^{n,m} h(\alpha_i)g(z_j) = 1$ with $l = nm$. Mean transmittance can now be calculated as $\bar{T} = \sum_{k=1}^{l} T_k w_k$. To acquire a meaningful histogram,

these pairs of transmittance and their respective weights need to be resampled into a histogram with a large enough bin width 2λ. The histogram of transmittance occurrence frequencies is then given by:

$$f(T - \lambda \leq T < T + \lambda) = \sum_{T-\lambda \leq T_i < T+\lambda} w_i \quad (3)$$

As this approach realizes some unlikely combinations of albedo and ice-thickness, the total range of light transmittance may be bigger than in reality, showing a longer tail in the histogram at higher transmittances. Similarly the precision at the lower end of the calculated transmittance will be biased including unrealistic albedo thickness combinations leading to low transmittance. Nevertheless, the respective probabilities (weights) are fairly small, so that the influence on both the mean value and the modal peak of the distribution should be negligible.

If the dependence of the ice thickness and surface albedo distribution are known or can be assumed, Equation 2 will only be evaluated for the valid combinations of n and m. In this case, the resulting weights f need to be adjusted to comply with the normalization criterion.

This treatment can be generalized by also including other parameters. The presented parameterization proved useful for summer conditions and is expected to provide good results while melt ponds are the governing surface feature. Before melting starts, a combination of histograms of ice thickness and snow thickness might be superior to a dedicated albedo treatment as the albedo is more uniform in space. The extinction coefficient can be either included as a distribution function determined from measurements, a constant with values chosen from the literature or used as a tuning parameter depending on the purpose. For a better investigation of the general applicability of this approach, more spatially extensive datasets have to be acquired with under-ice vehicles such as NUI.

Histograms derived from our dataset are shown in Figure 6. Using independent source distribution functions and an extinction coefficient of $\kappa = 1.5\ m^{-1}$ as commonly used in the literature [Grenfell, 1977; Perovich, 1996], the algorithm correctly estimates the main mode at 0.035 but slightly underestimates the occurrence of small light transmittance values (Figure 6c). As explained above, the deviations between measured and derived histogram at both ends of the distribution are expected. Comparing the cumulative distribution functions (Figure 6d) confirms a good agreement between measured and derived light transmittance distributions. While a final conclusion as to the possibility of

estimating transmission histograms from distributions of ice thickness and surface albedo is not possible using this limited dataset, our results encourage future exploration now that extensive spatial datasets of sea ice optics are attainable.

5. Conclusion

Our measurements conducted with a novel under ice vehicle combined with co-located surface measurements and aerial images enabled new insights into the spatial variability of the under ice light field. Measurements using irradiance sensors are strongly influenced by measurement geometry, so that under ice irradiance measurements must be analyzed in the context of ice and surface properties within a radius of several meters. This radius is determined by the distance of the sensor to the underside of the ice and lateral light propagation. The application of one-dimensional models based on spot measurements is not able to reproduce the full variability of the under ice light field.

While the spatial scales of under ice light variability are given by the scale of melt ponds when considering a smaller area (<1000 m²), the variability on larger scales is mostly driven by variations in the ice thickness. These variations may be due to ice deformation or to changes in ice type. This suggests that ice thickness might be a reliable predictor of under ice light conditions when combined with other aspects such as ice type and pond coverage.

Large spatially extensive datasets enable a statistical view on ice optical properties through the ability to construct histograms of light transmission underneath the ice. Based on our dataset, we suggest an algorithm to construct a histogram of light transmittance through sea ice as a combination of distribution functions of ice thickness and surface albedo. This approach could be used to combine remote sensing datasets of ice thickness (e.g. Cryosat 2) and albedo distributions (e.g. AVHRR, MODIS) into Arctic-wide maps of light transmittance through sea ice.

Figures

Figure 1 a) Map showing the cruise track (red line) in the northern Fram Strait between Greenland and Spitsbergen. The black x indicates the location of the presented ice station work. Sea ice concentration of the sampling day from AMSR2 (http://www.iup.uni-bremen.de:8084/amsr2/) is shown in grey shadings with high sea ice concentration in brighter colors. b) NUI shortly before deployment into a pool of open water on the starboard side of Polarstern. The upward looking sensors are located in the spine payload bay in between the two white landing skids toward the front of the vehicle.
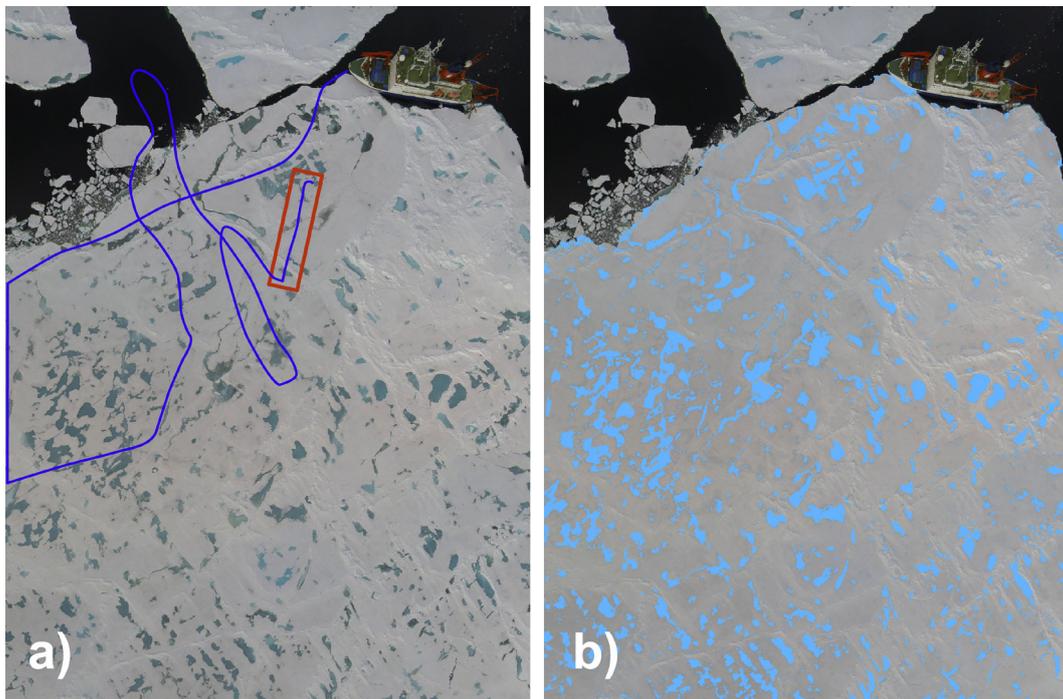
Figure 2 a) Mosaic of aerial images of the surveyed ice floe at 82° 51' N and 6° 19' W acquired during a low altitude helicopter flight on 28th July 2014. The blue line indicates the estimated vehicle track underneath the ice floe, ending with the co-registered pole transect marked by the red box. The length of Polarstern as reference scale is 120m. b) On the same image, pixels on the surveyed floe that were classified as melt pond are marked in light blue.
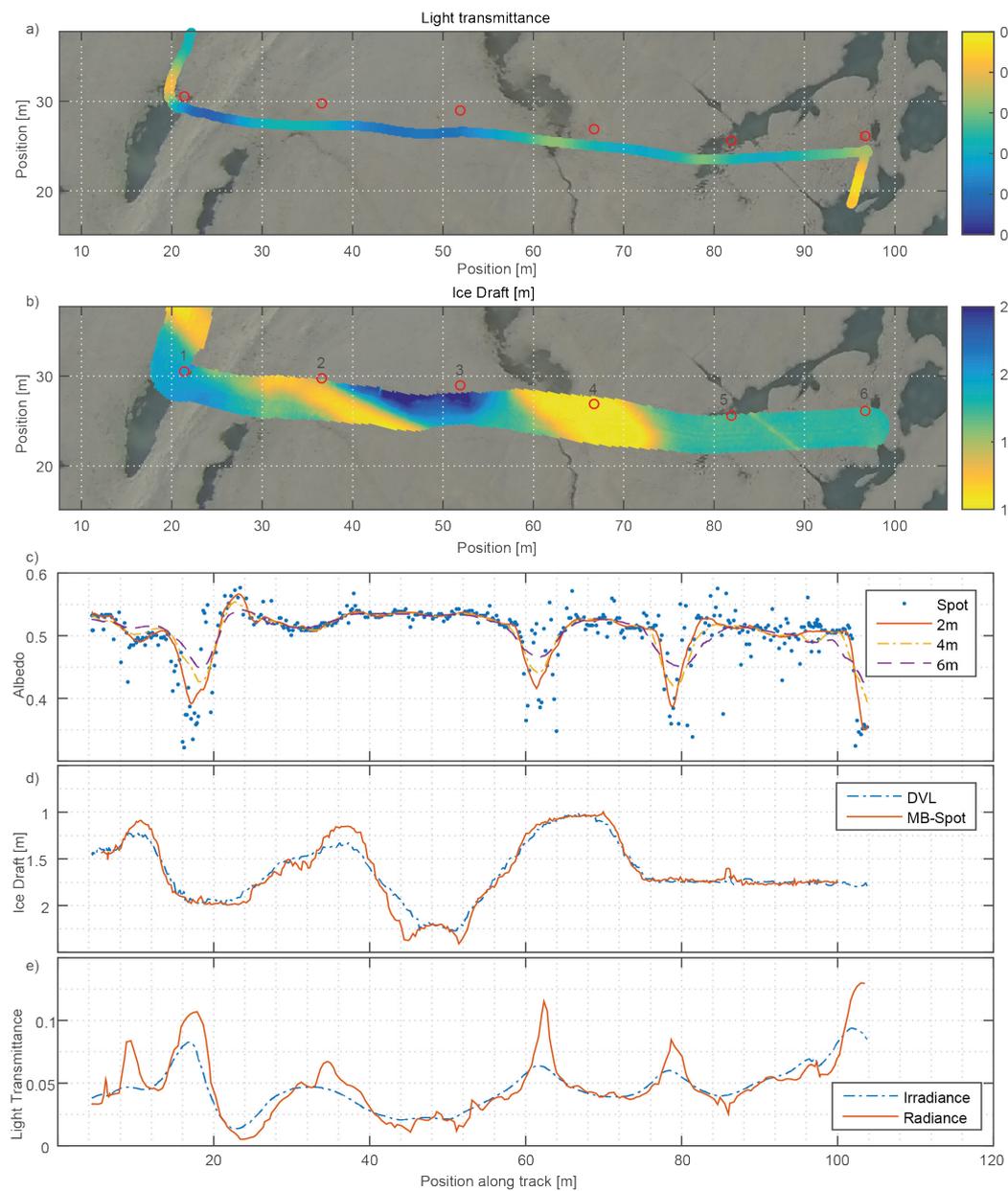
Figure 3 Physical measurements taken from the ROV during the colocated pole survey: a) Light transmittance along the survey track. Red circles show positions of numbered marker poles. b) Ice draft as measured along track with upward looking multibeam sonar. c) Surface albedo extracted from the image. Blue dots indicate spot data, while lines depict data averaged over circles with different diameters. d) Ice Draft as derived from the DVL (blue dashed line) and measured by the center beam of the multibeam sonar (red line). e) Light transmittance measured by the radiance (red line) and irradiance (blue dashed line) sensors along the survey.
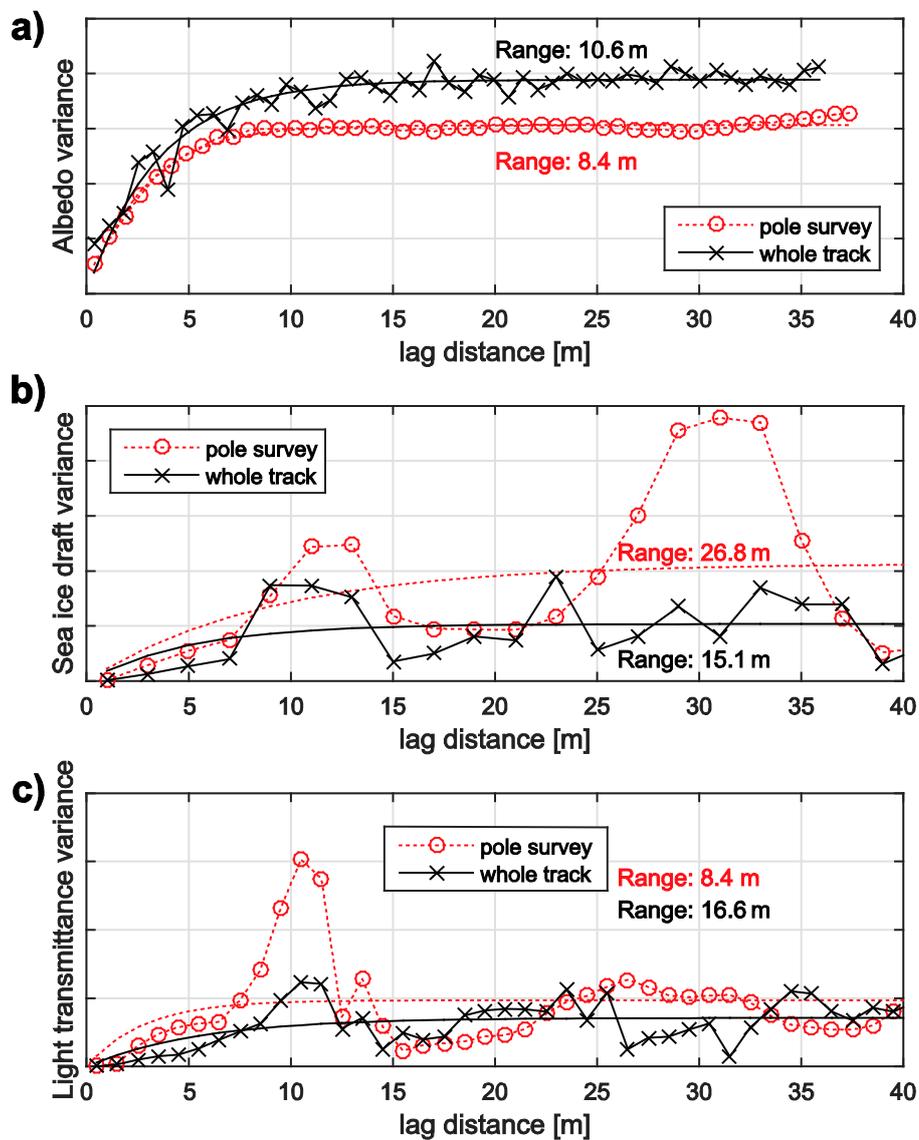
Figure 4 Variograms of surface albedo (a) sea ice draft (b) and light transmittance (c). Red lines indicate variograms obtained from the area of the pole survey, while black lines are derived from all available data. Empirical variograms are shown with x as data marker, while unmarked lines are fitted theoretical exponential histograms. The range values obtained from the fitting are given as annotations in the same color as the corresponding curve. Variance is given in arbitrary units starting at zero.
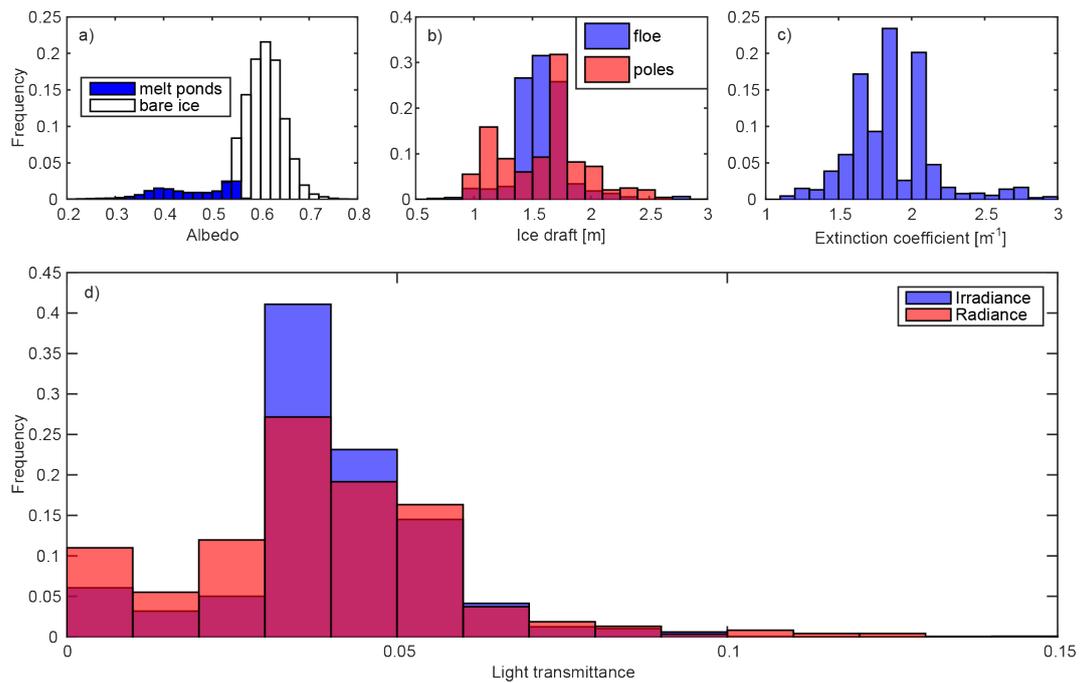
Figure 5 a) Histogram of surface albedo derived from the aerial image. b) Histogram of sea ice draft as measured from multibeam during the pole survey (red) and throughout the complete floe from upward looking DVL (blue). c) Histogram of bulk broadband light extinction coefficients derived from measured light transmittance. d) Histogram of irradiance (blue) and radiance (red, scaled to irradiance) light transmittance.
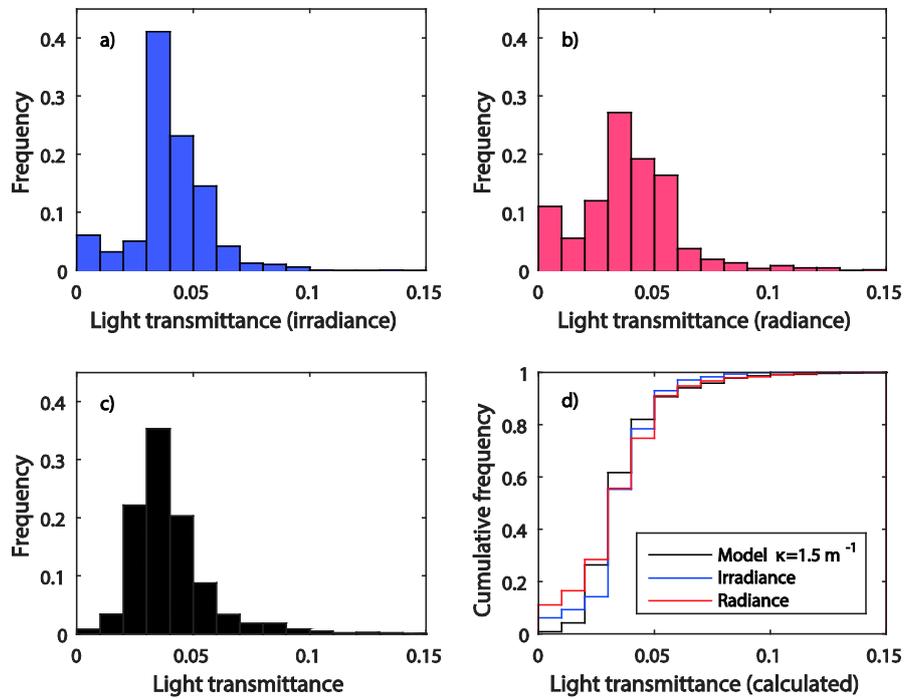
Figure 6 Histograms of light transmission as obtained from the irradiance (a) and radiance sensors (b). Light transmission histograms generated with the presented algorithm from the distribution of surface albedo and ice thickness using a extinction coefficient of κ =1.5m^{-1} for the case of independent source distribution functions (c). Same histograms presented as cumulative probability functions (d).

References

Arndt, S., and M. Nicolaus (2014), Seasonal cycle and long-term trend of solar energy fluxes through Arctic sea ice, *The Cryosphere*, *8*(6), 2219-2233, doi: 10.5194/tc-8-2219-2014.

Arrigo, K. R., et al. (2012), Massive Phytoplankton Blooms Under Arctic Sea Ice, *Science*, *336*(6087), 1408, doi: 10.1126/science.1215065.

Boetius, A. (2015), The expedition PS86 of the research vessel POLARSTERN to the Arctic Ocean in 2014, edited, Alfred Wegener Institute for Polar and Marine Research, Bremerhaven.

Bowen, A. D., M. Jakuba, D. Yoerger, C. German, J. C. Kinsey, L. L. Whitcomb, and L. Mayer (2012), Lightly tethered unmanned underwater vehicle for under-ice exploration, paper presented at Aerospace Conference, 2012 IEEE, 3-10 March 2012.

Bowen, A. D., et al. (2014), Design of Nereid-UI: A remotely operated underwater vehicle for oceanographic access under ice, paper presented at Oceans - St. John's, 2014, 14-19 Sept. 2014.

Divine, D. V., M. A. Granskog, S. R. Hudson, C. A. Pedersen, T. I. Karlsen, S. A. Divina, A. H. H. Renner, and S. Gerland (2015), Regional melt-pond fraction and albedo of thin Arctic first-year drift ice in late summer, *The Cryosphere*, *9*(1), 255-268, doi: 10.5194/tc-9-255-2015.

Fetterer, F., and N. Untersteiner (1998), Observations of melt ponds on Arctic sea ice, *J. Geophys. Res.-Oceans*, *103*(C11), 24821-24835, doi: 10.1029/98jc02034.

Frey, K. E., D. K. Perovich, and B. Light (2011), The spatial distribution of solar radiation under a melting Arctic sea ice cover, *Geophys. Res. Lett.*, *38*, L22501, doi: 10.1029/2011gl049421.

Grenfell, T. C. (1977), The optical properties of ice and snow in the arctic basin, *J. Glaciol.*, *18*(80), 445-463.

Haas, C., A. Pfaffling, S. Hendricks, L. Rabenstein, J.-L. Etienne, and I. Rigor (2008), Reduced ice thickness in Arctic Transpolar Drift favors rapid ice retreat, *Geophys. Res. Lett.*, *35*(17), L17501, doi: 10.1029/2008gl034457.

Hudson, S. R., M. A. Granskog, T. I. Karlsen, and K. Fossan (2012), An integrated platform for observing the radiation budget of sea ice at different spatial scales,

Cold Reg. Sci. Tech., *82*(0), 14-20, doi: http://dx.doi.org/10.1016/j.coldregions.2012.05.002.

Hudson, S. R., M. A. Granskog, A. Sundfjord, A. Randelhoff, A. H. H. Renner, and D. V. Divine (2013), Energy budget of first-year Arctic sea ice in advanced stages of melt, *Geophys. Res. Lett.*, *40*(11), 2679-2683, doi: Doi 10.1002/Grl.50517.

Jakuba, M. V., L. L. Whitcomb, D. R. Yoerger, and A. D. Bowen (2008), Toward under-ice operations with hybrid underwater robotic vehicles, paper presented at Autonomous Underwater Vehicles, 2008. AUV 2008. IEEE/OES, 13-14 Oct. 2008.

Katlein, C., M. Nicolaus, and C. Petrich (2014), The anisotropic scattering coefficient of sea ice, *Journal of Geophysical Research: Oceans*, doi: 10.1002/2013JC009502.

Kukulya, A., et al. (2010), Under-ice operations with a REMUS-100 AUV in the Arctic, paper presented at Autonomous Underwater Vehicles (AUV), 2010 IEEE/OES, 1-3 Sept. 2010.

Kwok, R., and D. A. Rothrock (2009), Decline in Arctic sea ice thickness from submarine and ICESat records: 1958-2008, *Geophys. Res. Lett.*, *36*, doi: 10.1029/2009gl039035.

Light, B., G. A. Maykut, and T. C. Grenfell (2003b), A two-dimensional Monte Carlo model of radiative transfer in sea ice, *J. Geophys. Res.-Oceans*, *108*(C7), doi: 10.1029/2002jc001513.

Light, B., T. C. Grenfell, and D. K. Perovich (2008), Transmission and absorption of solar radiation by Arctic sea ice during the melt season, *J. Geophys. Res.-Oceans*, *113*(C3), doi: 10.1029/2006jc003977.

Maslanik, J. A., J. Stroeve, C. Fowler, and W. Emery (2011), Distribution and trends in Arctic sea ice age through spring 2011, *Geophys. Res. Lett.*, *38*, doi: 10.1029/2011gl047735.

McFarland, C., M. Jakuba, S. Suman, J. Kinsey, and L. L. Whitcomb (2015), Toward Ice-Relative Navigation of Underwater Robotic Vehicles Under Moving Sea-Ice: Experimental Evaluation in the Arctic Sea in *IEEE ICRA 2015*, edited, Seattle WA (in press).

Meier, W. N., et al. (2014), Arctic sea ice in transformation: A review of recent observed changes and impacts on biology and human activity, *Rev Geophys*, *52*(3), 185-217, doi: Doi 10.1002/2013rg000431.

Mundy, C. J., D. G. Barber, and C. Michel (2005), Variability of snow and ice thermal, physical and optical properties pertinent to sea ice algae biomass during spring, *Journal of Marine Systems*, *58*(3-4), 107-120, doi: 10.1016/j.jmarsys.2005.07.003.

Nicolaus, M., and C. Katlein (2013), Mapping radiation transfer through sea ice using a remotely operated vehicle (ROV), *The Cryosphere*, *7*(3), 763-777, doi: 10.5194/tc-7-763-2013.

Nicolaus, M., S. R. Hudson, S. Gerland, and K. Munderloh (2010a), A modern concept for autonomous and continuous measurements of spectral albedo and transmittance of sea ice, *Cold Reg. Sci. Tech.*, *62*(1), 14-28, doi: 10.1016/j.coldregions.2010.03.001.

Nicolaus, M., C. Katlein, J. Maslanik, and S. Hendricks (2012), Changes in Arctic sea ice result in increasing light transmittance and absorption, *Geophys. Res. Lett.*, *39*, L24501, doi: 10.1029/2012gl053738.

Nicolaus, M., C. Petrich, S. R. Hudson, and M. A. Granskog (2013a), Variability of light transmission through Arctic land-fast sea ice during spring, *The Cryosphere*, *6*(5), 4363-4385, doi: 10.5194/tcd-6-4363-2012.

Nicolaus, M., S. Arndt, C. Katlein, J. Maslanik, and S. Hendricks (2013b), Correction to "Changes in Arctic sea ice result in increasing light transmittance and absorption", *Geophys. Res. Lett.*, *40*(11), 2699-2700, doi: 10.1002/grl.50523.

Perovich, D. K. (1996), The optical properties of sea ice, *Monograph 96-1*.

Perovich, D. K. (2011), The changing Arctic sea ice cover, *Oceanography*, *24*(3), 162-173.

Perovich, D. K., and C. Polashenski (2012), Albedo evolution of seasonal Arctic sea ice, *Geophys. Res. Lett.*, *39*, doi: 10.1029/2012gl051432.

Perovich, D. K., C. S. Roesler, and W. S. Pegau (1998a), Variability in Arctic sea ice optical properties, *J. Geophys. Res.-Oceans*, *103*(C1), 1193-1208, doi: 10.1029/97jc01614.

Perovich, D. K., T. C. Grenfell, B. Light, and P. V. Hobbs (2002), Seasonal evolution of the albedo of multiyear Arctic sea ice, *J. Geophys. Res.-Oceans*, *107*(C10), doi: 10.1029/2000jc000438.

Perovich, D. K., K. F. Jones, B. Light, H. Eicken, T. Markus, J. Stroeve, and R. Lindsay (2011), Solar partitioning in a changing Arctic sea-ice cover, *Ann. Glaciol.*, *52*(57), 192-196.

Petrich, C., M. Nicolaus, and R. Gradinger (2012a), Sensitivity of the light field under sea ice to spatially inhomogeneous optical properties and incident light assessed with three-dimensional Monte Carlo radiative transfer simulations, *Cold Reg. Sci. Tech.*, *73*, 1-11, doi: 10.1016/j.coldregions.2011.12.004.

Petrich, C., H. Eicken, C. M. Polashenski, M. Sturm, J. P. Harbeck, D. K. Perovich, and D. C. Finnegan (2012b), Snow dunes: A controlling factor of melt pond distribution on Arctic sea ice, *J. Geophys. Res.*, *117*(C9), C09029, doi: 10.1029/2012jc008192.

Renner, A. H. H., S. Gerland, C. Haas, G. Spreen, J. F. Beckers, E. Hansen, M. Nicolaus, and H. Goodwin (2014), Evidence of Arctic sea ice thinning from direct observations, *Geophys. Res. Lett.*, *41*(14), 5029-5036, doi: Doi 10.1002/2014gl060369.

Rösel, A., and L. Kaleschke (2012), Exceptional melt pond occurrence in the years 2007 and 2011 on the Arctic sea ice revealed from MODIS satellite data, *J. Geophys. Res.*, *117*(C5), C05018, doi: 10.1029/2011jc007869.

Rothrock, D. A., D. B. Percival, and M. Wensnahan (2008), The decline in arctic sea-ice thickness: Separating the spatial, annual, and interannual variability in a quarter century of submarine data, *J. Geophys. Res.*, *113*(C5), C05003, doi: 10.1029/2007jc004252.

Serreze, M. C., M. M. Holland, and J. Stroeve (2007), Perspectives on the Arctic's Shrinking Sea-Ice Cover, *Science*, *315*(5818), 1533-1536, doi: 10.1126/science.1139426.

Stroeve, J. C., M. M. Holland, W. Meier, T. Scambos, and M. Serreze (2007), Arctic sea ice decline: Faster than forecast, *Geophys. Res. Lett.*, *34*(9), doi: 10.1029/2007gl029703.

Stroeve, J. C., M. C. Serreze, M. M. Holland, J. E. Kay, J. Malanik, and A. P. Barrett (2012), The Arctic's rapidly shrinking sea ice cover: a research synthesis, *Climatic Change*, *110*(3-4), 1005-1027, doi: DOI 10.1007/s10584-011-0101-1.

Thomas, N. D., and G. S. Dieckmann (2010), *Sea Ice*, John Wiley \& Sons.

Thorndike, A. S., D. A. Rothrock, G. A. Maykut, and R. Colony (1975), The thickness distribution of sea ice, *Journal of Geophysical Research*, *80*(33), 4501-4513, doi: 10.1029/JC080i033p04501.

Trodahl, H. J., R. G. Buckley, and S. Brown (1987), Diffusive transport of light in sea ice, *Appl. Optics*, *26*(15), 3005-3011, doi: 10.1364/AO.26.003005.

Tschudi, M., C. Fowler, J. Maslanik, and J. Stroeve (2010), Tracking the Movement and Changing Surface Characteristics of Arctic Sea Ice, *Ieee J-Stars*, *3*(4), 536-540, doi: Doi 10.1109/Jstars.2010.2048305.

Wadhams, P., J. P. Wilkinson, and S. D. McPhail (2006), A new view of the underside of Arctic sea ice, *Geophys. Res. Lett.*, *33*(4), L04501, doi: 10.1029/2005GL025131.

Williams, G. D., T. Maksym, J. Wilkinson, C. Kunz, C. Murphy, P. Kimball, and H. Singh (2015), Thick and deformed Antarctic sea ice mapped with autonomous underwater vehicles, *Nature Geosci*, *8*(1), 61-67, doi: 10.1038/ngeo2299.

Williams, G. D., et al. (2013), Beyond Point Measurements: Sea Ice Floes Characterized in 3-D, *Eos, Transactions American Geophysical Union*, *94*(7), 69-70, doi: 10.1002/2013EO070002.

Zeebe, R. E., H. Eicken, D. H. Robinson, D. WolfGladrow, and G. S. Dieckmann (1996), Modeling the heating and melting of sea ice through light absorption by microalgae, *J. Geophys. Res.-Oceans*, *101*(C1), 1163-1181, doi: 10.1029/95jc02687.

4. Paper 2

GEOMETRIC EFFECTS OF AN INHOMOGENEOUS SEA ICE COVER ON THE UNDER ICE LIGHT FIELD

Christian Katlein[1], Donald K. Perovich[2], Marcel Nicolaus[1]

[1]Alfred-Wegener-Institut Helmholtz-Zentrum für Polar- und Meeresforschung, Bussestr. 24, 27570 Bremerhaven, Germany

[2]Cold Regions Research and Engineering Laboratory, Hanover, New Hampshire, USA

Abstract

Light measurements in the ocean provide crucial information about the energy fluxes in the climate and ecosystem. Currently radiative transfer problems are usually considered in horizontally homogeneous layers. In this paper, we examine the effects of a horizontally inhomogeneous sea ice layer on the light field in the water underneath. We implemented a three dimensional model, capable to simulate the light field underneath various surface geometries using ray optics. The results show clear effects of the measurement geometry on measured fluxes obtained with different sensor types, which need to be taken into account for the correct interpretation of the data. Furthermore we show that the determination of the light extinction coefficient of water from vertical profiles is complicated under a horizontally inhomogeneous ice cover. This also limits the possibility to correct light measurements taken at depth for the influence of water in between the sea ice and the sensor.

1. Introduction

Light measurements using radiometers are an important tool in geosciences. They provide crucial input data for various disciplines. From atmospheric shortwave radiation measurements [e.g. *Ohmura et al.*, 1998] to rain forest ecology [e.g. *Nicotra et al.*, 1999] to ocean optics [e.g. *Antoine et al.*, 2014], scientists derive inherent optical properties, often from vertical profiles or time series data. In most of those cases the approach of horizontally infinite homogenous layers is a sufficiently good approximation of reality.

Light measurements above, in and underneath the sea ice of the polar regions are of particular interest due to their crucial role in the description of the surface energy budget of sea ice and the light conditions available to organisms associated to the ice [*Perovich*, 1996]. In contrast to most other above named cases, the light field underneath sea ice exhibits a high spatial variability on length scales smaller or of similar size as the measurement footprint of the instruments [*Perovich*, 1990; *Petrich et al.*, 2012a]. Horizontal variability on those length scales is usually not considered in the interpretation of light measurements apart from a few exemptions - such as light focusing by waves at the ocean surface [*Wijesekera et al.*, 2005].

The horizontal heterogeneity of Arctic sea ice is especially pronounced in the summer season when melting reshapes the surface and causes the formation of melt ponds [*Fetterer and Untersteiner*, 1998; *Petrich et al.*, 2012b] and an

increased number of floe edges due to breakup of the pack ice [*Perovich and Jones*, 2014]. This surface looks similar to a jigsaw puzzle from the air and the complicated geometry heavily influences the light field underneath [*Ehn et al.*, 2011; *Frey et al.*, 2011]. Typically geometric effects of the sea ice cover have not been taken into account during data interpretation.

The objective of this paper is to illustrate the various effects of measurement geometry to facilitate correct interpretation of future under ice light measurements. We discuss in particular the constraints for corrections of measurements not taken directly at the ice underside and the influence on retrieval of water properties - such as the extinction coefficient - by vertical light profiles in ice covered waters.

2. Methods

To evaluate the effects of measurement geometry on under ice light measurements, we implemented a three dimensional model of geometric radiometry in MATLAB. It builds on previous models of the under ice light field. These models did not account for arbitrary surface variations by either only considering a two dimensional linear transect [*Katlein et al.*, 2014] or strongly simplified surface geometries that allow for algebraic solutions [*Frey et al.*, 2011]. Here we present a three dimensional model, that can be used under arbitrary light conditions at the ice underside.

The goal of our model is to calculate the under ice light field as measured by different sensors under an arbitrary inhomogeneous ice cover in an efficient manner. The model is of purely geometric nature using only ray optics. It is not taking into account scattering within the medium - here sea-water - which is a very good approximation for the clear water found underneath sea ice in the central Arctic Ocean, except for strong bloom situations. We consider the ice to have a flat bottom and all distances are measured relative to the ice bottom. To be able to separate the effects caused by geometry from effects of ice topography and lateral transport of light in the ice by scattering, which has been investigated previously [*Petrich et al.*, 2012a], the model calculates the under-ice light field geometry based on the light transmitted to the ice bottom.

Downwelling planar irradiance F is defined as the cosine weighted integral over downwelling radiance $L(\theta, \phi)$ in the upper half space with the zenith angle θ and the azimuth angle ϕ.

$$F = \int_{\phi=0}^{2\pi} \int_{\theta=0}^{\pi/2} L(\theta, \phi) \cos \theta \, \sin \theta d\theta d\phi \qquad (1)$$

Numerical integration of Equation 1 can be achieved in various ways. A computationally efficient way is a high order Lebedev-quadrature [*Lebedev and Laikov*, 1999], where the unit sphere is divided into up to 5810 similarly sized sub-segments of which 2861 represent the upward looking solid angles Ω_i. The angular integration then reduces to a sum over all upward pointing light rays L_i with weights ω_i representing the respective solid angle covered by the segments:

$$F = \sum_i L_i(\theta_i, \phi_i)\omega_i \quad (2)$$

For each single ray the radiance L_i reaching the detector can then be determined by calculating the intersection point of the respective ray with the surface plane from the given zenith and azimuth angles and the depth of the detector z (Figure1). The surface plane is represented by a sufficiently large matrix defining surface light values (sea ice transmittance or total flux). Light transmittance was set to 0.04 for bare ice and 0.22 for melt ponds according to *Nicolaus et al.* [2012]. The surface matrix needs to be wide enough to cover enough grazing rays with large zenith angles. A horizontal extent of at least ten times the investigated sensor depth ensures numerical stability and accuracy of better than 2% (10%) for planar (scalar) irradiance. However, the picked surface values cannot be inserted directly into equation 2, but need to be corrected for both, the angular distribution of radiance emitted from the underside of the sea ice, and the angular sensitivity of the detector.

There are several versions of radiance distribution implemented in the model. In the fully isotropic case, the radiance is the same in any direction. As this is not the case under strongly scattering media, we only implemented it into the model for validation purposes, as the ratios of different sensor types are only trivially defined for a completely isotropic light field [*Mobley*, 1994]. In realistic cases, the radiance distribution is described by the exit function of an isotropically scattering medium presented by *Kokhanovsky* [2006]

$$L(\theta) = \frac{3}{7}(1 + 2\cos\theta) \qquad (3)$$

or for cases of anisotropic scattering in sea ice

$$L(\theta, \gamma) = \left(\frac{1}{3} + \frac{2}{3}\cos\theta\right)\cos\theta\,(1-\gamma) + \gamma\exp(-0.0568\theta) \ (4)$$

with the anisotropy parameter γ as presented by *Katlein et al.* [2014]. Here we only present results for the case of isotropic scattering in ice being an upper bound, as a more downward peaked radiance distribution reduces geometric

effects [*Katlein et al.*, 2014].The surface light conditions are given as transmittances or fluxes of planar irradiance, so the surface values need to be divided by π, that the resulting computation yields irradiance values.

The second correction of the radiances L_i is the sensor dependent weighting of different zenith angles θ_i. While for planar irradiance the radiance needs to be weighted with the cosine of the zenith angle θ, scalar irradiance is calculated without any further weighting. For calculation of radiance sensor readings, only rays with a zenith angle θ smaller than half the angle given by the sensors field of view are considered. The result is then divided by the solid angle covered by the cone of the sensors field of view. Due to the finite segments of solid angle represented in the Lebedev sphere, this calculation only provides stable results for sufficiently large field of view of the radiance sensor (10°).

Before final evaluation of the sum, all obtained and corrected radiances are scaled to account for water absorption with a radiance extinction coefficient using the respective pathlength d of the ray from the surface to the sensor and the radiance extinction coefficient κ:

$$L_i = L \exp(-\kappa d) \quad (5)$$

The resulting model performs well on an ordinary desktop computer. For validation it was checked, that the model correctly reproduces the ratios between measurements with different sensor types and the exponential decay under a homogenous surface. In particular, the apparent extinction coefficient determined for all three sensor types matches the radiance extinction coefficient, as expected in the asymptotic limit. A MATLAB implementation of the model can be downloaded from the MATLAB file exchange under http://www.mathworks.com/matlabcentral/fileexchange/50566-geometric-light-field-model.

3. Results

To evaluate the effect of surface geometry, we ran the model for four surface geometries depicted in Figure 2. They correspond to the following sea ice features: The semi-infinite obstruction with a linear edge (Figure 2a) is a first approach to investigating lateral effects. The geometry is applicable to any sharp large scale contrast in the ice optical properties, especially to edges of ice floes. A linear obstruction (Figure 2b) is similar to the geometry of pressure ridges. A

single melt pond was approximated by a circular patch with higher light transmission (Figure 2c) and a part of a classified aerial image enabled for evaluation of a real melt pond geometry with a pond fraction of 12% (Figure 2d).

3.1. Lateral effects at a linear edge

The response of different light sensors on a transect crossing a linear edge is shown in Figure 3. This example comprises two zones of light transmittances of 0.04 and 0.22 and a water extinction coefficient of $\kappa = 0.1\mathrm{m}^{-1}$, typical for Arctic first year ice in the summer [*Nicolaus et al.*, 2012]. While the narrow footprint of the radiance sensor (10°) reproduces the sharp contrast in light measurements even at greater depths, the measurements with the planar and scalar irradiance sensors are strongly influenced by geometric effects at the boundary. The contrast gets smoothed by the large footprint of the irradiance sensors. Light is propagating laterally into the darker area from the adjacent bright patch leading to irradiance levels higher than expected from a one dimensional model. Vice versa, measurements under the bright patch are influenced by the adjacent dark patch leading to lower light measurements than expected from a one dimensional model. At increasing depths, the contrast between both zones gets increasingly smeared out leaving only a weak contrast. The variability of the surface light field can thus only be captured appropriately, when using radiance sensors or limiting the distance of irradiance sensors to the sea ice. Scalar irradiance sensors show the strongest geometric effects.

From the different response of the three sensors to simple geometric variation, we can immediately deduct, that the ratios between radiance and planar or scalar irradiance are not constant in space under a spatially varying sea ice cover. While the ratio of different light sensor readings is often used to describe the optical properties of the water body in open ocean optics [*Mobley*, 1994], the geometric variation of the ice cover makes such an approach difficult in ice covered seas.

To allow for the application of the results to any combination of transmittance values, we normalized the calculated values in such way, that the range between the asymptotical light values far into each region is mapped to the interval from 0 to 1. When considering absorption to calculate the asymptotic values at a certain depth, the resulting relative light field geometry is independent of water absorption.

The calculated lateral transects are shown for three different depths in Figure 4. The radiance measurements follow a step curve, with a tapering section of a width given by the field of view of the sensor the distance to the surface.

The irradiance sensors show a different characteristic response, a smooth transition between the asymptotic values. For a first estimation of the lateral extent of the geometric effects, we found that at the distance from the edge, that equals the distance of the sensor from the ice underside, the reading of planar (scalar) irradiance is about 12% (20%) - of the difference in light transmission between the zones - away from the asymptotic value. The distance at which the irradiance has reached a difference of less than 1/e of the difference in light transmission is linearly dependent on the distance between sensor and ice (Figure 5). Thus the distance to the ice gives a first order approximation of the extent of geometric effects in the lateral dimensions.

The calculated transect of planar irradiance was fitted with a piecewise exponential function F adapted from *Petrich et al.* [2012a]:

$$F(x) = \begin{cases} x > 0 & 1 - 0.5\exp(-a|x|) \\ x < 0 & 0.5\exp(-a|x|) \end{cases}, \qquad (6)$$

where the coefficient of the lateral exponential decay a is given by the distance of the sensor to the ice by $a = 1.405d^{-1}$. The fitted equation matches the calculated curve very well with an adjusted $R^2 > 0.99$. For scalar irradiance the same equation can be used with a different coefficient $a = 0.811d^{-1}$. From now on we will focus on results regarding planar irradiance only, as the smoothing across light contrasts for spherical irradiance is very similar but somehow stronger.

We want to point out, that equation 6 describes the pure geometric effect of a contrast in ice optical properties on the under ice light field. The absolute magnitude of the geometric effects is of course dependent on the contrast in light transmittance. Similar equations have been proposed by *Petrich et al.* [2012a] and *Ehn et al.* [2011] but in the context of lateral light propagation due to scattering within the ice.

3.2. Lateral effects associated with sea ice features

The results from the linear semi-infinite obstruction can be qualitatively generalized to the more complex situation underneath melt ponds, pressure ridges and leads in the ice cover. For pressure ridges and leads being mostly linear features, the results of the previous section can be used directly, if the

ridge or lead is wider than two times the sensor depth. If the ridge or lead is narrower than this threshold, irradiance levels will not reach the asymptotic end value under the obstruction. The contrast in light transmittance then seems weaker than it actually is. This is similar for circular features such as melt ponds, but due to the circular geometry, the asymptotic end value underneath the pond will only be reached at a slightly greater distance from the pond edge as compared to a linear feature.

3.3. Vertical effects associated with ridges and melt ponds

Figure 4 shows the calculated light field underneath a darker linear feature. It is clearly visible, that the surface geometry can distort the vertical profile away from an exponential decay. While under bright patches, the vertical profile follows an exponential decay monotonically decreasing with increasing depth, the irradiance maximum can be located at depth under dark patches (Figure 6). This is due to the fact that the adjacent brighter areas get into the large footprint of the irradiance sensor when getting to greater depth and has been observed before [*Frey et al.*, 2011; *Nicolaus and Katlein*, 2013].

The depth of this deep irradiance maximum is dependent on several factors: The width of the dark area and the distance of the sensor to the boundaries. While the irradiance maximum is located at the surface under the bright patch, it quickly submerges to a typical depth of 5 to 10m. If the dark patch is large enough, the magnitude of the deep irradiance maximum decreases. The larger the dark patch, the deeper the irradiance maximum is located. Contrary, a greater water extinction coefficient compensates the effect and reduces the maximum depth, as deep irradiance maxima then can only be found in a narrower zone close to the boundary between bright and dark patch. Additionally a downward peaked anisotropic radiance distribution causes deeper irradiance maxima, but further limits their lateral extent [*Katlein et al.*, 2014].

Extraction of the extinction coefficient from the calculated light field under a circular melt pond of varying size revealed significant differences to the given radiance extinction coefficient (Figure 7). Even though the vertical profiles could be well fitted with an exponential decay law ($R^2 > 0.98$), the apparent extinction coefficient differs from the actual one even under very large ponds. If the pond radius is equal to the maximum depth of the sensor during the profile, the retrieved apparent extinction coefficient is still deviating about 25% from the true value. Usually the pond radii are much smaller than the depth of the profile, making a robust retrieval of the extinction coefficient of sea water from vertical

irradiance profiles difficult in ice covered waters. This shows, that the influence of geometric effects on the light field cannot be ruled out, even when the profiles seem to follow a perfect exponential decay.

3.4. Combined lateral and vertical effects in a real geometry

To further assess the abilities to extract water extinction coefficients, we calculated the irradiance field underneath a real surface geometry from a classified aerial image (Figure 8) obtained during a helicopter flight north of Greenland in July 2014 (http://epic.awi.de/37745/). Figure 8b shows how different the vertical profiles are when taken at different close lying points. Analysis of all 2600 calculated vertical profiles under the real geometry revealed a mean extinction coefficient of $\bar{\kappa} = 0.1 \ m^{-1}$ when only considering fits where $R^2 > 0.9$. While this result seems to show accuracy of extraction of the extinction coefficient underneath a spatially varying ice cover, we want to point to the fact, that only 49% of the depth profiles could be fitted with a $R^2 > 0.9$. Even within this limited selection of vertical profiles, the mean deviation ($\delta = \overline{(|\kappa - \kappa_r|)}/\kappa$) of the retrieved extinction coefficient κ_r from the true extinction coefficient κ is 27% with values of κ_r ranging between $\kappa_r = 0.07m^{-1}$ and $\kappa_r = 0.44m^{-1}$. About 10% of the extracted extinction coefficients were overestimated by more than 120%. To obtain an extinction coefficient closer than 10% to the real one from averaging of several vertical profiles, one would need to consider over 200 randomly positioned profiles, which is not practicable. Estimates can in general be significantly improved to reduce the mean deviation from 27% to 7% by only considering the lower part (>15m depth) of the vertical profile which is less affected by geometric effects. As the extinction coefficient might vary vertically, this estimate may though not represent the water layer close to the sea ice.

Furthermore, we evaluated the effect of lateral geometry on measured data to explore the advantages and disadvantages of correcting measurement data for the distance between sensor and the ice water interface. Using the true extinction coefficient for correction of planar irradiance (radiance) values assuming an exponential decay law, we determined mean deviations between calculated and true value of 45% (10%) at a depth of 5m and 60%(35%) at a sensor depth of 30m. When using an extinction coefficient deviating from the true one by the mean error in the retrieval from vertical profiles (27%) increases this deviation to 52% at 5m and 81% at 30m depth. Considering the worst case deviation of retrieved apparent extinction coefficient of in our case $\kappa_r = 0.44m^{-1}$, a deviation of 440%, the mean error of the depth corrected data is

significantly bigger than the mean error of uncorrected data for all sensor depths shallower than 3m.

In spite of the errors when comparing specific points, depth correction successfully corrects the mean energy loss with depth. Contrary it cannot restore the variability of the light field present in the surface, which is better accomplished by radiance sensors (Figure 9).

4. Discussion

4.1. Retrieval of extinction coefficients

The retrieval of inherent optical properties from the observation of apparent optical properties is a main objective of ocean optics observations [*Antoine et al.*, 2014; *Light et al.*, 2008]. Our results show, that the inhomogeneous ice cover increases the difficulties for the retrieval of inherent optical properties from vertical profiles dramatically. To obtain valid measurements of inherent optical properties, the surface needs to be homogenous in a radius much bigger than the maximum depth of the vertical profile around the vertical profile. This does not only apply to measurements from instruments lowered through a hole in the ice [*Frey et al.*, 2011], but also to optical packages deployed in the vicinity of sea ice [*Bélanger et al.*, 2013], for example in a pool of open water next to the ship used to lower instrumentation in the water column or generally in the vicinity of ships. Unfortunately contamination from geometric effects may not be detectable from the shape of the vertical profile. While these geometric effects would not be as severe in radiance sensors, it is very likely that imperfect horizontal positioning during vertical profiles due to lateral drift and sensor tilt can also reduce the quality of the retrieval of inherent optical properties.

Precise modeling of the light field under sea ice needs to take into account the complex geometry of the sea ice surface and cannot be achieved by multiple one dimensional models. Thus light measurements under sea ice should be interpreted in the context of spatial datasets of ice geometry, such as aerial images and ice bottom topography [*Williams et al.*, 2013]. In particular, care should be taken to account for the measurement geometry when investigating any geometric aspect of the under ice light field, such as high resolution lateral transects.

4.2. Depth correction of sensor data

Our results show, that the usefulness of correcting light measurements taken at depth to the level of the ice-water interface is strongly dependent on the ultimate goal of the data analysis. For studies interested in the spatial variability of the light field, we recommend to use radiance sensors and convert the readings to irradiance at the ice bottom according to *Katlein et al.* [2014]. If only irradiance sensors are available, they should be operated with minimum distance to the ice. Discarding data with a distance of more than a certain limit to the ice bottom instead of applying a correction, avoids introducing undetermined errors due to unknown exact geometry and water absorption. Even when water absorption is precisely known from direct measurements using a transmissometer, the geometric errors of a measurement taken at depth cannot be corrected. For example, a one dimensional "correction" of a measurement taken under a dark patch would result in too high light values at the ice bottom.

On the other hand, even an imperfect estimate of light extinction in the water column can provide a reasonable way, to account for the water in between sensor and ice when investigating the large scale average of measurements for studies of the energy balance.

The geometric effects average out on larger scales and thus do not affect the energy transfer to depth. However, the measurement geometry influences the shape of histograms of measured light values such as those presented in [*Nicolaus et al.*, 2013a]. Thus geometric effects should be considered when picking modal values from histograms for upscaling efforts [*Arndt and Nicolaus*, 2014]. Here data that is potentially contaminated by geometric effects should be discarded from the analysis.

4.3. Sensitivity of different sensor types

We mostly showed results for planar irradiance data, as this sensor type is most widely used throughout the physical community [*Eicken and Salganek*, 2010; *Hudson et al.*, 2013; *Nicolaus et al.*, 2010a; *Perovich*, 1996]. The footprint of these sensors is very large leading to strong effects of measurement geometry. Radiance sensors have a narrower field of view and thus suffer less from geometric effects and better represent the true variability of light conditions even in measurements taken at depth. While this is an advantage in lateral surveys, it can also impact the quality of vertical profiles under a spatially varying ice cover, when the profile deviates from being perfectly vertical.

Spherical irradiance sensors behave similar to planar irradiance sensors, but have an even larger effective field of view as the proportional contribution of lateral traveling light to the signal is even bigger. The effects of measurement geometry are thus even stronger for spherical sensors making them the least suitable sensor for studies on spatial variability. This disadvantage for studies of spatial variability is of course an advantage, when only the mean energy fluxes are of interest.

5. Conclusion

We developed and implemented a model of geometric radiometry underneath spatially inhomogeneous surfaces and investigated the effects of various simplified geometries on the light field underneath. Results show that radiance sensors are least affected by the measurement geometry and spherical irradiance sensors are mostly unsuitable for studies of spatial variability.

The effect of the inhomogeneous surface hinders effective retrieval of the inherent optical properties of the water column from vertical profiles in the sea ice covered ocean and limits the possibilities of correcting data that was measured at depth, for the influence of light extinction in water. Great care should be taken when interpreting measurements taken over lateral contrasts in the optical properties of the sea ice. Here the distance of the sensor to the ice significantly smoothens out the contrast and might easily mask the effects of lateral light transport in the ice by scattering.
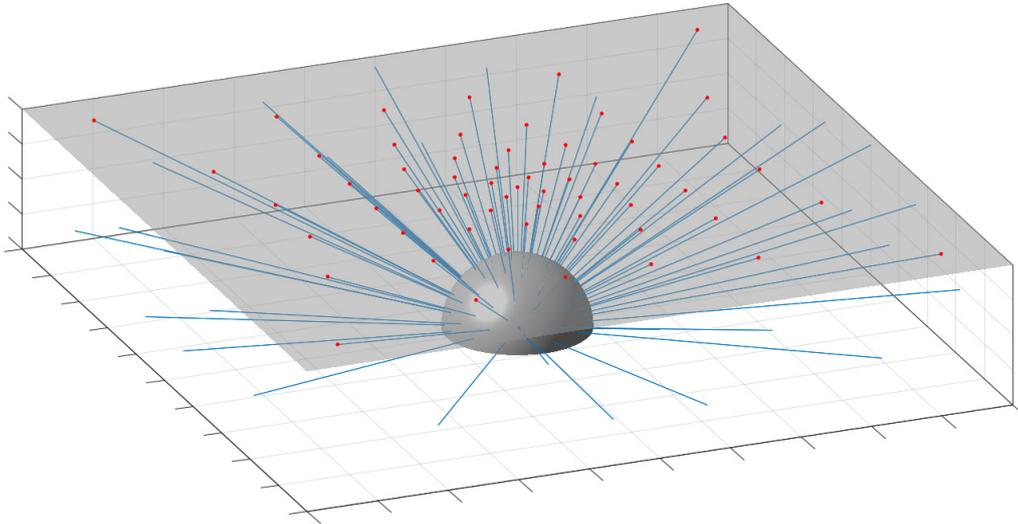
Figures

Figure 1: Geometry of the light model integrator. The half sphere represents the unit Lebedev sphere with blue rays pointing in the direction of each segment. Rays are intersecting the surface (grey transparent layer) in the location of the red dots. At these locations radiance values are taken from the inhomogenous surface matrix.
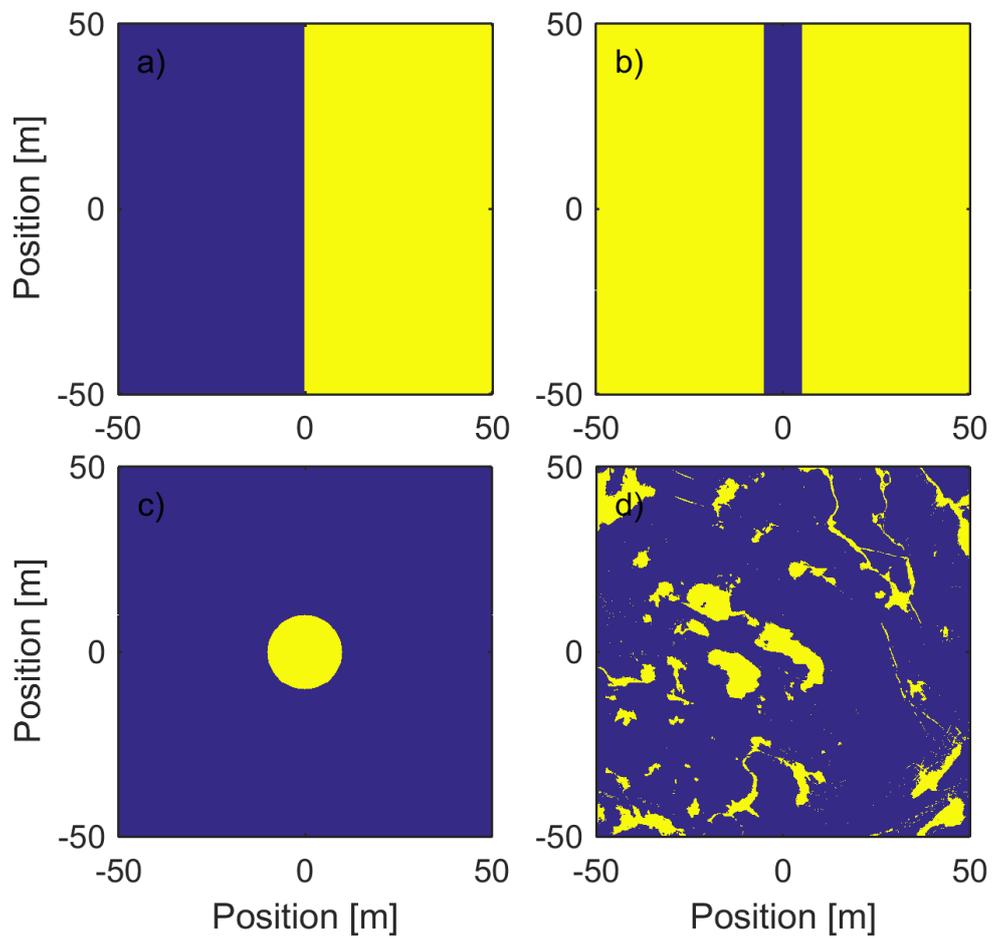
Figure 2: The different geometries used in this study. Yellow color depicts high light transmittance and blue color low light transmittance. The surface geometries resemble a) a floe edge, b) a pressure ridge, c) a melt pond, and d) a real geometry of melt pond covered sea ice extracted from an aerial picture.
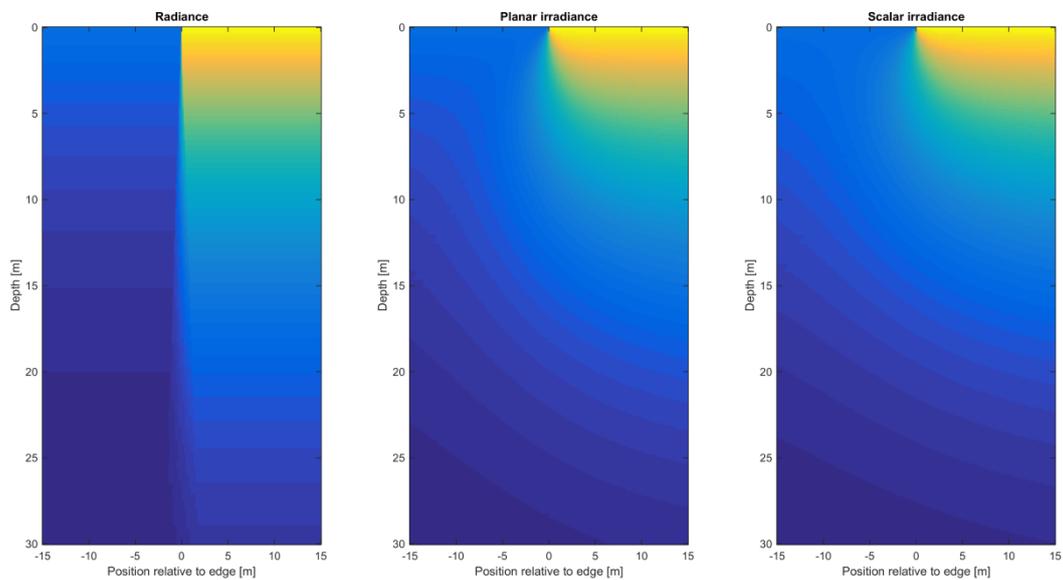
Figure 3: Under ice light transmittance across a semi-infinite boundary measured with radiance (left), planar irradiance (middle), and scalar irradiance (right) sensors. Colors represent normalized light measurements from bright (yellow) to dark (blue). The scenario uses ice transmittances of 0.22 (right of the edge) and 0.04 (left of the edge) and an extinction coefficient $\kappa = 0.1 \text{ m}^{-1}$.
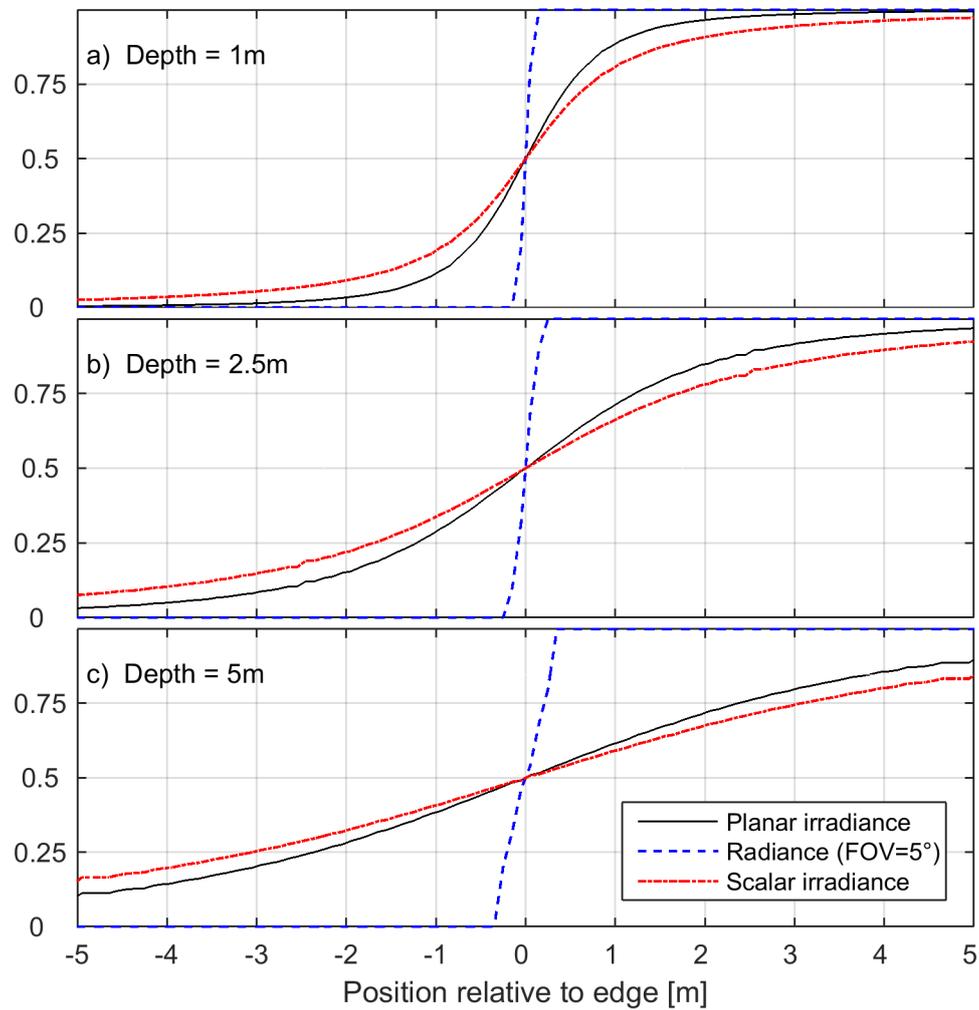
Figure 4: Lateral transect of light measurements across a semi-infinite boundary in different depths under the ice water interface.
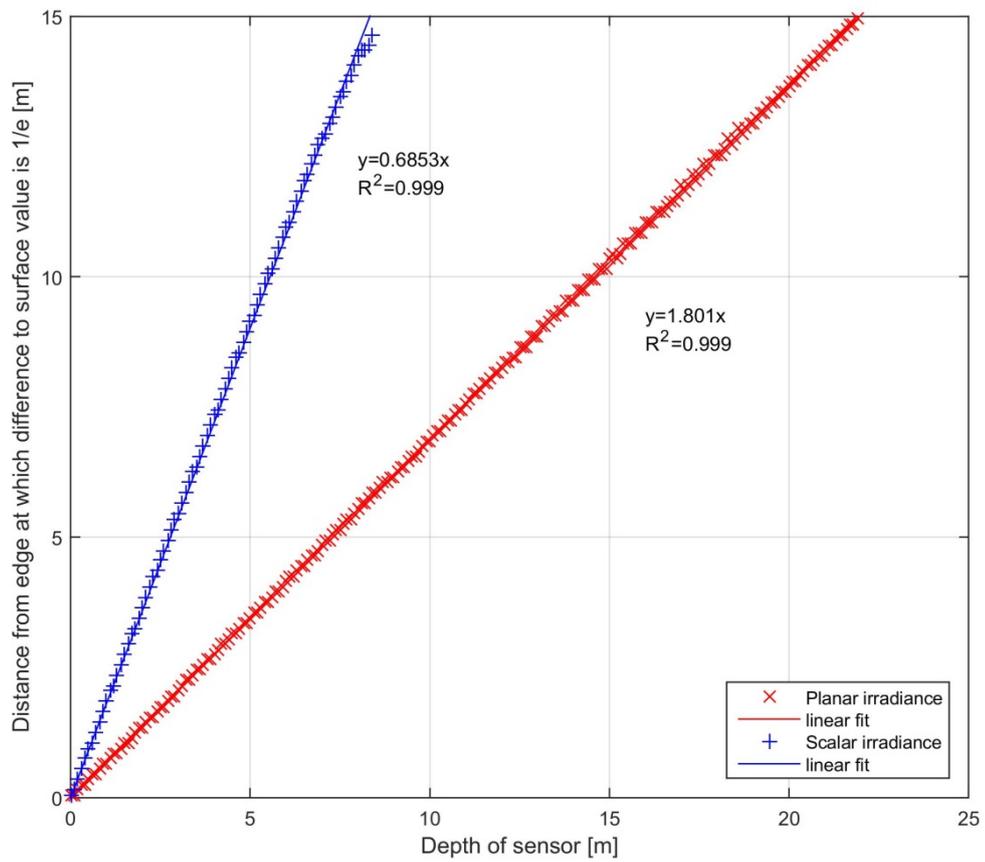
Figure 5: This plot shows the distance from the edge at which the difference of the sensor reading from the true asymptotical value has decreased to 1/e of the difference of light transmission across the edge (e-folding length)
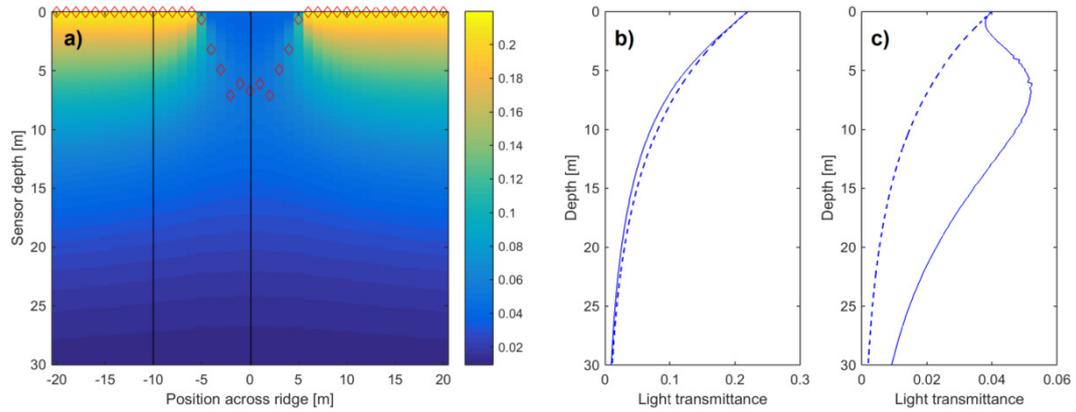
Figure 6: a) Vertical depth profiles across a linear dark patch. Red diamonds mark the location of the maximal irradiance. b) Vertical irradiance profile for the position shown by the black lines in a within the bright patch c) and in the middle under the dark patch. Solid blue lines show the calculated irradiance profile while dashed lines are given by a one dimensional exponential decay model.
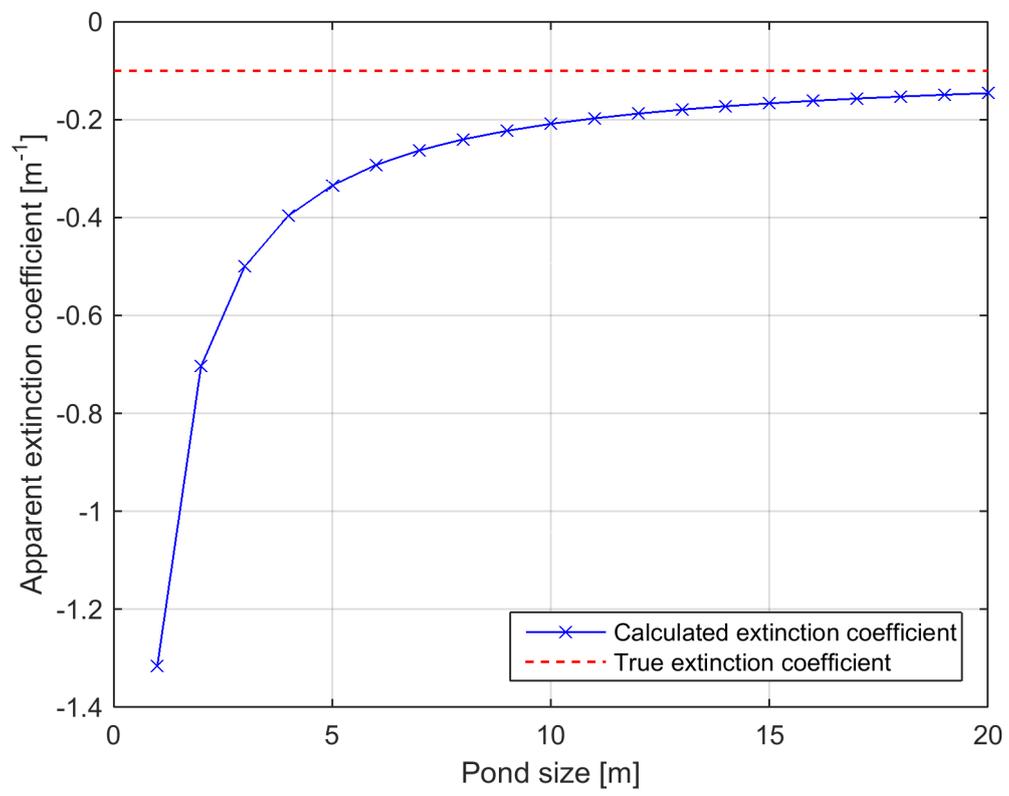
Figure 7: Extinction coefficients as retrieved from vertical depth profiles under the middle of a melt-pond of varying radius.
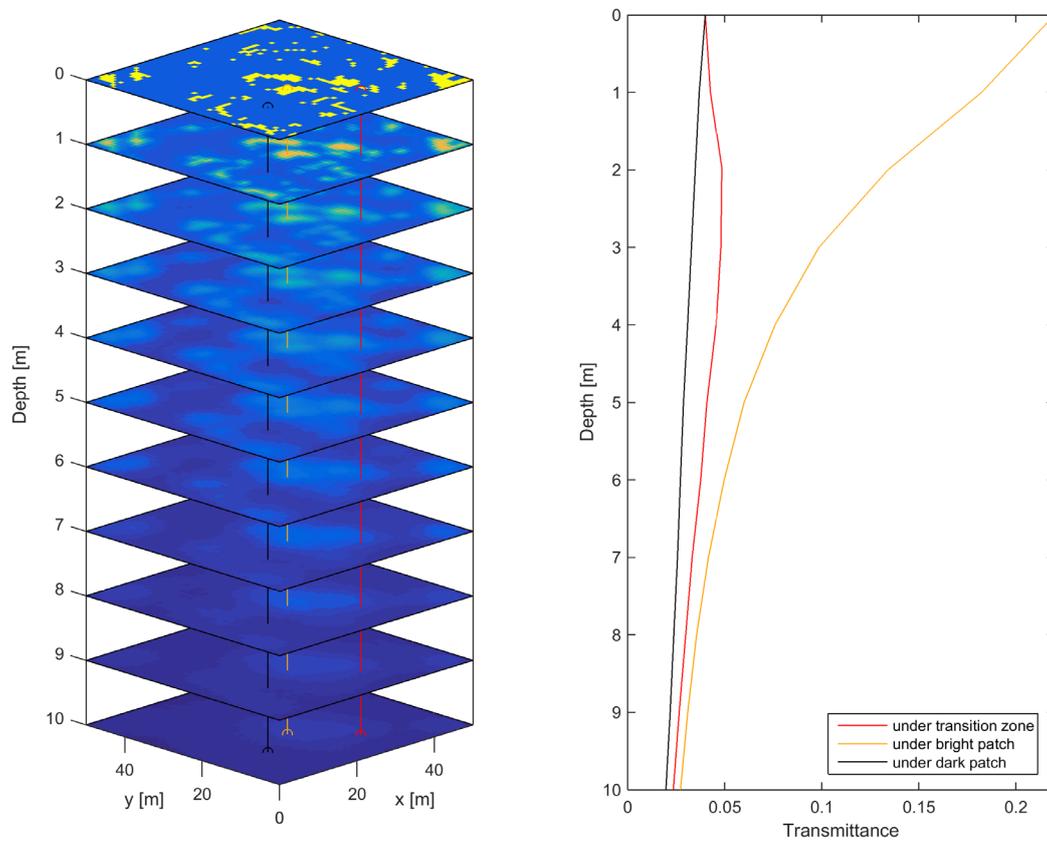
Figure 8: a) Depth slices of the light field underneath a real surface geometry extracted from an aerial image. Bright colors show high light transmittance. b) Vertical irradiance profiles extracted at three different close lying locations indicated in a.
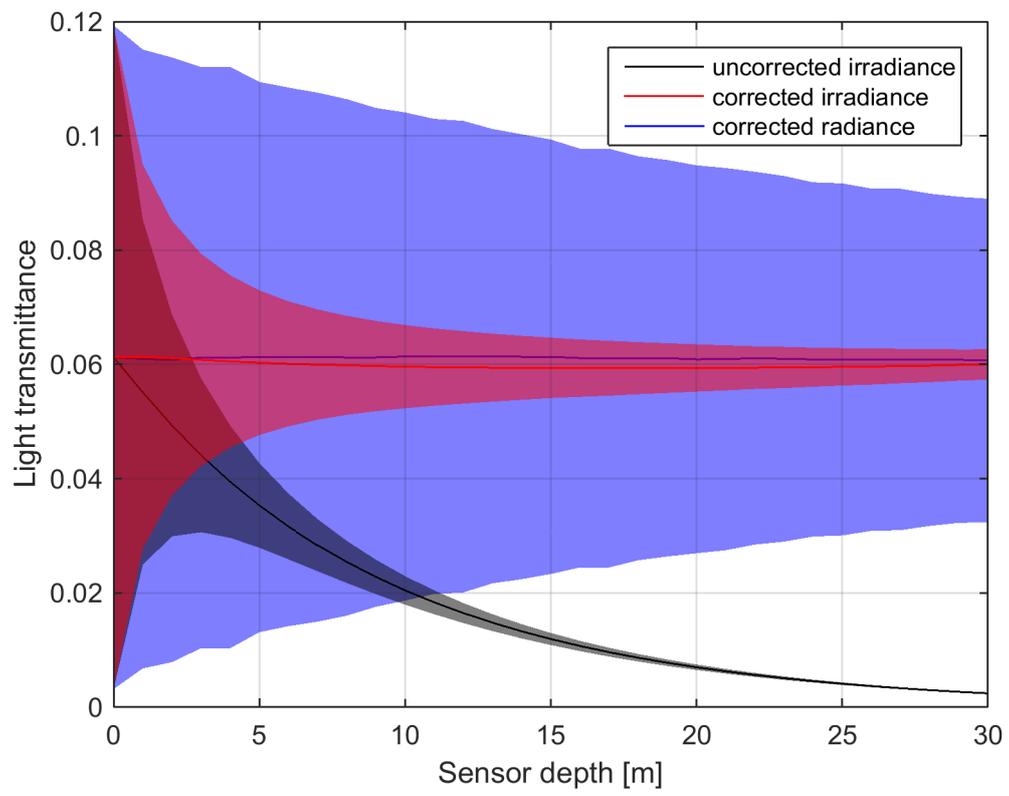
Figure 9: a) Depth slices of the light field underneath a real surface geometry extracted from an aerial image. Bright colors show high light transmittance. b) Vertical irradiance profiles extracted at three different close lying locations indicated in a.

References

Antoine, D., M. Babin, J.-F. Berthon, A. Bricaud, B. Gentili, H. Loisel, S. Maritorena, and D. Stramski (2014), Shedding Light on the Sea: André Morel's Legacy to Optical Oceanography, *Annual Review of Marine Science*, *6*(1), 1-21, doi: doi:10.1146/annurev-marine-010213-135135.

Arndt, S., and M. Nicolaus (2014), Seasonal cycle and long-term trend of solar energy fluxes through Arctic sea ice, *The Cryosphere*, *8*(6), 2219-2233, doi: 10.5194/tc-8-2219-2014.

Bélanger, S., S. A. Cizmeli, J. Ehn, A. Matsuoka, D. Doxaran, S. Hooker, and M. Babin (2013), Light absorption and partitioning in Arctic Ocean surface waters: impact of multiyear ice melting, *Biogeosciences*, *10*(10), 6433-6452, doi: 10.5194/bg-10-6433-2013.

Ehn, J. K., C. J. Mundy, D. G. Barber, H. Hop, A. Rossnagel, and J. Stewart (2011), Impact of horizontal spreading on light propagation in melt pond covered seasonal sea ice in the Canadian Arctic, *J. Geophys. Res.-Oceans*, *116*, doi: 10.1029/2010jc006908.

Eicken, H., and M. Salganek (2010), *Field Techniques for Sea-Ice Research*, University of Alaska Press.

Fetterer, F., and N. Untersteiner (1998), Observations of melt ponds on Arctic sea ice, *J. Geophys. Res.-Oceans*, *103*(C11), 24821-24835, doi: 10.1029/98jc02034.

Frey, K. E., D. K. Perovich, and B. Light (2011), The spatial distribution of solar radiation under a melting Arctic sea ice cover, *Geophys. Res. Lett.*, *38*, L22501, doi: 10.1029/2011gl049421.

Hudson, S. R., M. A. Granskog, A. Sundfjord, A. Randelhoff, A. H. H. Renner, and D. V. Divine (2013), Energy budget of first-year Arctic sea ice in advanced stages of melt, *Geophys. Res. Lett.*, *40*(11), 2679-2683, doi: Doi 10.1002/Grl.50517.

Katlein, C., M. Nicolaus, and C. Petrich (2014), The anisotropic scattering coefficient of sea ice, *Journal of Geophysical Research: Oceans*, doi: 10.1002/2013JC009502.

Kokhanovsky, A. A. (2006), *Cloud Optics*, Springer Netherlands.

Lebedev, V. I., and D. N. Laikov (1999), A quadrature formula for the sphere of the 131st algebraic order of accuracy, *Doklady Mathematics*, *59*(3), 477-481.

Light, B., T. C. Grenfell, and D. K. Perovich (2008), Transmission and absorption of solar radiation by Arctic sea ice during the melt season, *J. Geophys. Res.-Oceans*, *113*(C3), doi: 10.1029/2006jc003977.

Mobley, C. D. (1994), *Light and water: radiative transfer in natural waters*, Academic Press.

Nicolaus, M., and C. Katlein (2013), Mapping radiation transfer through sea ice using a remotely operated vehicle (ROV), *The Cryosphere*, *7*(3), 763-777, doi: 10.5194/tc-7-763-2013.

Nicolaus, M., S. R. Hudson, S. Gerland, and K. Munderloh (2010a), A modern concept for autonomous and continuous measurements of spectral albedo and transmittance of sea ice, *Cold Reg. Sci. Tech.*, *62*(1), 14-28, doi: 10.1016/j.coldregions.2010.03.001.

Nicolaus, M., C. Katlein, J. Maslanik, and S. Hendricks (2012), Changes in Arctic sea ice result in increasing light transmittance and absorption, *Geophys. Res. Lett.*, *39*, L24501, doi: 10.1029/2012gl053738.

Nicolaus, M., C. Petrich, S. R. Hudson, and M. A. Granskog (2013a), Variability of light transmission through Arctic land-fast sea ice during spring, *The Cryosphere*, *6*(5), 4363-4385, doi: 10.5194/tcd-6-4363-2012.

Nicotra, A. B., R. L. Chazdon, and S. V. B. Iriarte (1999), SPATIAL HETEROGENEITY OF LIGHT AND WOODY SEEDLING REGENERATION IN TROPICAL WET FORESTS, *Ecology*, *80*(6), 1908-1926, doi: 10.1890/0012-9658(1999)080[1908:SHOLAW]2.0.CO;2.

Ohmura, A., et al. (1998), Baseline Surface Radiation Network (BSRN/WCRP): New Precision Radiometry for Climate Research, *Bulletin of the American Meteorological Society*, *79*(10), 2115-2136, doi: 10.1175/1520-0477(1998)079<2115:BSRNBW>2.0.CO;2.

Perovich, D. K. (1990), Theoretical estimates of light reflection and transmission by spatially complex and temporally varying sea ice covers, *J. Geophys. Res.-Oceans*, *95*(C6), 9557-9567, doi: 10.1029/JC095iC06p09557.

Perovich, D. K. (1996), The optical properties of sea ice, *Monograph 96-1*.

Perovich, D. K., and K. F. Jones (2014), The seasonal evolution of sea ice floe size distribution, *Journal of Geophysical Research: Oceans*, *119*(12), 8767-8777, doi: 10.1002/2014JC010136.

Petrich, C., M. Nicolaus, and R. Gradinger (2012a), Sensitivity of the light field under sea ice to spatially inhomogeneous optical properties and incident light assessed with three-dimensional Monte Carlo radiative transfer simulations, *Cold Reg. Sci. Tech.*, *73*, 1-11, doi: 10.1016/j.coldregions.2011.12.004.

Petrich, C., H. Eicken, C. M. Polashenski, M. Sturm, J. P. Harbeck, D. K. Perovich, and D. C. Finnegan (2012b), Snow dunes: A controlling factor of melt pond distribution on Arctic sea ice, *J. Geophys. Res.*, *117*(C9), C09029, doi: 10.1029/2012jc008192.

Wijesekera, H., W. S. Pegau, and T. Boyd (2005), Effect of surface waves on the irradiance distribution in the upper ocean, *Opt. Express*, *13*(23), 9257-9264, doi: 10.1364/OPEX.13.009257.

Williams, G. D., et al. (2013), Beyond Point Measurements: Sea Ice Floes Characterized in 3-D, *Eos, Transactions American Geophysical Union*, *94*(7), 69-70, doi: 10.1002/2013EO070002.

5. Paper 3

THE ANISOTROPIC SCATTERING COEFFICIENT OF SEA ICE

Christian Katlein[1], Marcel Nicolaus[1], Chris Petrich[2]

[1]Alfred-Wegener-Institut Helmholtz-Zentrum für Polar- und Meeresforschung, Bussestr. 24, 27570 Bremerhaven, Germany

[2]Norut Narvik AS, P.O. Box 250, 8504 Narvik, Norway.

@AGU PUBLICATIONS

JGR

Journal of Geophysical Research: Oceans

The anisotropic scattering coefficient of sea ice

Christian Katlein[1], Marcel Nicolaus[1], and Chris Petrich[2]

[1]Alfred-Wegener-Institut Helmholtz-Zentrum für Polar- und Meeresforschung, Bremerhaven, Germany, [2]Norut Narvik AS, Narvik, Norway

Abstract Radiative transfer in sea ice is subject to anisotropic, multiple scattering. The impact of anisotropy on the light field under sea ice was found to be substantial and has been quantified. In this study, a large data set of irradiance and radiance measurements under sea ice has been acquired with a Remotely Operated Vehicle (ROV) in the central Arctic. Measurements are interpreted in the context of numerical radiative transfer calculations, laboratory experiments, and microstructure analysis. The ratio of synchronous measurements of transmitted irradiance to radiance shows a clear deviation from an isotropic under-ice light field. We find that the angular radiance distribution under sea ice is more downward directed than expected for an isotropic light field. This effect can be attributed to the anisotropic scattering coefficient within sea ice. Assuming an isotropic radiance distribution under sea ice leads to significant errors in light-field modeling and the interpretation of radiation measurements. Quantification of the light field geometry is crucial for correct conversion of radiance data acquired by Autonomous Underwater Vehicles (AUVs) and ROVs.

1. Introduction

The optical properties of sea ice are tightly linked to climate and biological productivity in polar oceans. Sea-ice albedo and light transmittance strongly impact the energy balance in the Arctic Ocean [*Nicolaus et al.*, 2012; *Perovich et al.*, 2011], and absorption of solar incoming energy affects surface and internal melting [*Nicolaus et al.*, 2010b; *Zeebe et al.*, 1996], leading to ice decay [*Petrich et al.*, 2012b]. Melt and decay of sea ice cause changes in its physical properties. Those properties like density, brine volume, and the internal structure of sea ice are determining its function as a habitat [*Eicken et al.*, 2002; *Krembs et al.*, 2011; *Mundy et al.*, 2005]. Good quantitative understanding of radiation partitioning is also important for assessment of the productivity of ice-borne microalgae [*Ehn and Mundy*, 2013; *Ehn et al.*, 2008a; *Leu et al.*, 2010].

Radiative transfer in sea ice has been widely studied using various numerical models and a large variety of measurements [e.g., *Ehn et al.*, 2008b; *Light et al.*, 2008; *Mobley et al.*, 1998; *Pegau and Zaneveld*, 2000; *Tro-dahl et al.*, 1987]. Nevertheless, knowledge about the optical properties of sea ice is still incomplete. While sea-ice albedo has been subject to considerable attention, knowledge about radiative transfer and absorption in sea ice is more limited due to the difficult access to the under-ice environment.

Due to the changes in properties of the Arctic sea ice such as younger ice age and decreased thickness [e.g., *Haas et al.*, 2008; *Maslanik et al.*, 2007; *Perovich*, 2011; *Serreze et al.*, 2007], the assumption of a homogenous ice cover becomes increasingly invalid, in particular during summer when melt ponds develop [*Nicolaus et al.*, 2012; *Roesel and Kaleschke*, 2012] and the ice cover is transformed into a patchwork of various surface types. The larger heterogeneity of surface properties requires a better understanding of scattering properties and vertical radiation transfer, as recently highlighted in studies by *Ehn et al.* [2011] and *Frey et al.* [2011]. The discrepancy of models and observations [*Frey et al.*, 2011] also impacts estimates of the depth of the euphotic zone in ice-covered oceans [*Bélanger et al.*, 2013], which might be underestimated due to insufficient consideration of radiation partitioning in sea ice.

In sea ice, radiative transfer is subject to multiple scattering, altering the angular distribution of radiance [*Petrich et al.*, 2012a]. In order to obtain energy balance measurements, irradiance is typically measured on a horizontal planar interface. The downwelling planar irradiance F is defined as the integral of the radiance L incident from all angles of the upper hemisphere, weighed by the cosine of the zenith angle θ,

$$F = \int_{\phi=0}^{2\pi} \int_{\theta=0}^{\pi/2} L(\theta,\phi)\ \cos\theta\ \sin\theta d\theta d\phi\ , \tag{1}$$

where θ and ϕ is the azimuth angle.

Equation (1) describes the energy flux through a horizontal surface. Downwelling scalar irradiance $F_{2\pi}$ is frequently used in biology, since the photosystems of autotrophic organisms are equally sensitive to photons from all incidence angles. It is defined analogously to equation (1),

$$F_{2\pi} = \int_{\phi=0}^{2\pi} \int_{\theta=0}^{\pi/2} L(\theta,\phi)\ \sin\theta d\theta d\phi\ . \tag{2}$$

As the azimuthal dependence of the radiance distribution is negligible under optically thick ice [*Maffione et al.*, 1998; *Pegau and Zaneveld*, 2000], the radiance distribution in equation (1), $L(\theta,\phi)$, can be replaced by the zenith radiance L_0 and the relative angular distribution of radiance $f(\theta)$ with $f(0°) = 1$,

$$F = 2\pi \cdot L_0 \int_{\theta=0}^{\pi/2} f(\theta)\cos\theta\ \sin\theta d\theta. \tag{3}$$

When the radiance distribution under the sea ice is isotropic and thus $f(\theta) = 1$, equation (3) evaluates to $F = \pi \cdot L_0$. Although it is well known that even for strong scattering and in the asymptotic state of large optical thickness the radiance distribution of transmitted light does not become isotropic [*Jaffé*, 1960; *Maffione et al.*, 1998; *Pegau and Zaneveld*, 2000; *van de Hulst*, 1980], an isotropic light field has been assumed frequently to convert between radiance and irradiance under sea ice [*Frey et al.*, 2011; *Grenfell*, 1977; *Roulet et al.*, 1974]. To provide a practical measure to convert between radiance and irradiance, we introduce the C value that depends on the angular distribution of radiance, $f(\theta)$:

$$C = \frac{F}{L_0}. \tag{4}$$

C is the ratio of irradiance F to zenith radiance L_0. Combining equations (3) and (4), the C value can also be obtained from a direct measurement of the radiance distribution $f(\theta)$ under sea ice,

$$C = 2\pi \int_{\theta=0}^{\pi/2} f(\theta)\cos\theta\ \sin\theta d\theta. \tag{5}$$

Equations (1)–(5) describe the geometry of the light field and are valid for both monochromatic light and wavelength integrated broadband fluxes.

While most studies of inherent optical properties of sea ice treated sea ice as optically isotropic [e.g., *Ehn et al.*, 2008b; *Light et al.*, 2003; *Maffione et al.*, 1998; *Mobley et al.*, 1998], *Trodahl et al.* [1987] introduced the idea of an anisotropic scattering coefficient to explain their measurements. The only measurements of the radiance distribution of transmitted light under sea ice appear to be those of *Trodahl et al.* [1989]. However, the radiance distribution has been studied within sea ice [*Pegau and Zaneveld*, 2000] and for a laser beam leaving the upper surface of the sea ice [*Schoonmaker et al.*, 1989]. *Trodahl et al.* [1987] found that light transfer could be described by assuming a scattering coefficient that is greater horizontally than vertically, which manifests itself in a greater extinction of "laterally propagating light" [*Zhao et al.*, 2010]. The stronger extinction of light traveling horizontally changes the radiance distribution in such a way that the resulting light field is more downward directed [*Trodahl et al.*, 1987] (Figure 1).

As nomenclature of anisotropy in scattering can be ambiguous, we want to clarify the nomenclature used in the following. In most of the literature, "anisotropic scattering" refers to the anisotropy of the scattering
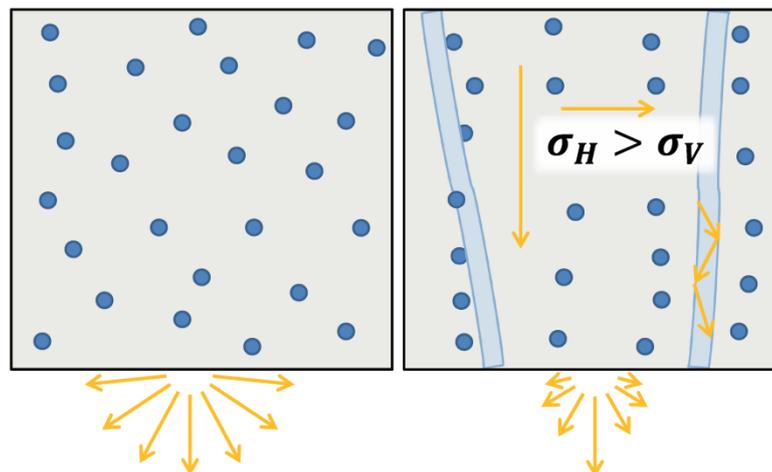
Figure 1. (left) In standard radiative transfer models scatterers (blue circles) are distributed randomly and homogenous throughout the medium. (right) Scatterers in sea ice are predominantly aligned along the lamellar crystal structure causing the anisotropy of the scattering coefficient. Anisotropic light extinction changes the shape of the radiance distribution underneath the sea ice.

phase function. Here we examine the effects of the anisotropic optical properties of the scattering medium on the radiance distribution exiting the sea ice. In this paper, we use the term anisotropy always to indicate that the effective scattering coefficient is dependent on the direction of light travel.

The objective of this paper is to investigate the angular radiance distribution below sea ice and its impact on the under-ice light-field and radiation measurements.

2. Methods

2.1. ROV Measurements

All measurements were performed during the expedition ARK-XXVII/3 (IceArc 2012) of the German research icebreaker *Polarstern* to the central Arctic from 2 August to 8 October 2012. We conducted synchronous measurements of spectral downwelling irradiance and radiance under sea ice using RAMSES-ACC (irradiance) and RAMSES-ARC (radiance) spectral radiometers (TriOS GmbH, Rastede, Germany) carried onboard a V8Sii Remotely Operated Vehicle (ROV) (Ocean Modules, Åtvidaberg, Sweden). ROV Observations were conducted within 1–2 m from the ice underside, yielding sensor footprint diameters of around 3.0 and 0.15 m for irradiance and radiance, respectively [*Nicolaus et al.*, 2010a]. Using synchronous measurements of downwelling irradiance at the surface, we obtained a large data set of 14,700 pairs of sea-ice transmittance and transflectance. Transflectance was introduced by *Nicolaus and Katlein* [2013] as the ratio of transmitted zenith radiance to downwelling irradiance at the surface, while transmittance is defined as the ratio of transmitted downwelling irradiance to downwelling irradiance at the surface. In addition to the setup previously described by *Nicolaus and Katlein* [2013], the ROV was equipped with an ultra-short-baseline (USBL) positioning system. The ROV attitude was recorded to give precise inclination information for the optical sensors and thus the possibility to measure the angular radiance distribution directly by rolling the ROV to the side underneath homogenous sea ice.

2.2. Lab Experiments

To measure the anisotropic nature of light extinction in the laboratory at $-20°$C, we used a setup similar to the one of *Grenfell and Hedrick* [1983]. Sea-ice samples were obtained from the bottommost part of a 12 cm-diameter ice core. As the anisotropy of the scattering coefficient is a feature of multiple scattering,
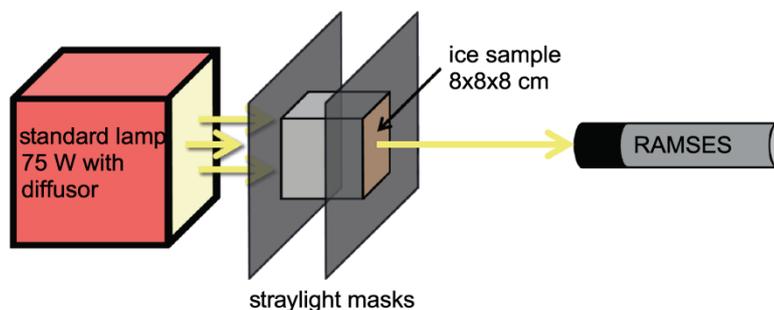
Figure 2. Sketch of the experimental setup to measure horizontal and vertical light extinction.

the sample size was chosen considerably bigger than in previous studies [*Grenfell and Hedrick*, 1983; *Miller et al.*, 1997]. Cubic samples with an edge length of 8 ± 0.1 cm were cut from the core using a band saw. All surfaces were brushed clean from ice cuttings, smoothened with sandpaper, and finally polished with bare hands to obtain a clear surface. Exact sample sizes were measured with a caliper and samples were weighed onboard the ship to determine porosity using equations from *Cox and Weeks* [1983]. Between preparation and measurements, samples were packed in plastic wrapping to avoid further sublimation.

As shown in Figure 2, the samples were placed on a black stage and illuminated through a diffusor plate (ground glass) with a standard 75 W light bulb (OSRAM, München, Germany). The light bulb provided a stable diffuse light source over the measured wavelength range (320–950 nm) and the duration of the experiments. The lamp output was measured to be stable within $\pm 1\%$. Cardboard masks with a 7×7 cm^2 rectangular opening were placed at both sides of the samples to avoid stray light entering the detector and to reduce the influence of imperfect sample edges. The light exiting the sample was registered by a RAMSES-ARC sensor measuring spectral radiance with a field of view of approximately 7°. The sensor was mounted at a distance of either 17.5 cm or 32.7 cm from the sample to register light emerging from a circular area with a diameter of $\sim$2 cm and 4 cm, respectively.

The transmitted normal radiance was measured for all six possible sample orientations. To reduce the influence of sample inhomogeneity, measurements from opposite sample orientations were averaged. As no anisotropy was observed in the horizontal plane, we averaged all four measurements of horizontal extinction. Radiance extinction coefficients κ_L were computed from

$$\kappa_L = \frac{-\ln \frac{L_{sample}}{L_{empty}}}{l},$$ (6)

with radiance measured with and without sample in the sample holder L_{sample} and L_{empty}, respectively, and sample size, l.

Horizontal and vertical thin sections were prepared from ice cuttings left over from preparation of the cubic samples. They were photographed between crossed polarizers with a digital camera. Ice crystal and pore geometries were subsequently analyzed using the image processing software *JMicroVision*.

2.3. Radiative Transfer Model
As anisotropic inherent optical properties are currently not resolved in most radiative transfer models [e.g., *Hamre et al.*, 2004; *Kokhanovsky and Zege*, 2004], we used a Monte Carlo ray tracing model to evaluate the effect of the anisotropic scattering coefficient in sea ice. The Monte Carlo model was described in detail by *Petrich et al.* [2012a]. It is a three-dimensional, single-layer model designed to simulate anisotropic scattering coefficients as defined by *Trodahl et al.* [1987]. In the model, photons are tracked through a homogenous slab of a scattering medium. Directions of photon travel are changed by scattering events. The frequency of scattering events is determined from the scattering coefficient that in our anisotropic case is dependent on the

photon travel direction. The instantaneous scattering coefficient for a photon traveling at angle θ is calculated during the runtime of the model as $\sigma = \sigma_v + (\sigma_h - \sigma_v)\sin\theta$ [*Petrich et al.*, 2012a; *Trodahl et al.*, 1987]. We used the model to evaluate the effect of the anisotropic scattering coefficient on radiative transfer in a typical slab of sea ice. The ice thickness in the simulations was 1 m. This is a typical thickness of arctic first year ice [*Haas et al.*, 2008] and thick enough to ensure that the asymptotic state of the light field has been reached in unponded sea ice [*Pegau and Zaneveld*, 2000], resulting in an emerging light-field independent of the light-field incident on the surface. Common values for the asymmetry parameter of the phase function, $g = 0.98$, and the effective (isotropic) scattering coefficient $\sigma_{eff} = \sigma(1-g) = 2 \text{ m}^{-1}$ were chosen according to the available literature [*Haines et al.*, 1997; *Light et al.*, 2008; *Mobley et al.*, 1998; *Pegau and Zaneveld*, 2000; *Perovich*, 1990; *Petrich et al.*, 2012a]. The anisotropy of the scattering coefficient is described similar to *Trodahl et al.* [1989] by the relation of vertical and horizontal scattering coefficients σ_v and σ_h, respectively, as

$$\gamma = 1 - \frac{\sigma_v}{\sigma_h} \tag{7}$$

and was varied between $\gamma = 0$ and $\gamma = 0.8$ guided by the values presented by *Haines et al.* [1997]. The horizontal scattering coefficient, σ_h, is always greater than σ_v for sea ice. Transmittance depends nontrivially on both σ_h and σ_v. To keep the transmittance constant while varying anisotropy values γ, both scattering coefficients need to be adjusted simultaneously. We used an empirical scaling law to estimate the vertical and horizontal scattering coefficients from σ_{eff} and γ in the absence of absorption,

$$\begin{aligned} \sigma_v &= \sigma_{eff}(1-\gamma)^{0.78} \\ \sigma_h &= \sigma_{eff}(1-\gamma)^{-0.22} \end{aligned}. \tag{8}$$

Using equation (8), the bulk transmittance remained constant to within $\pm 1\%$ of the transmittance value for the scattering coefficients and anisotropies used in this study. We performed 40 simulations with different anisotropy and scattering coefficients, each with 10^6 photons. As our goal was to explore the effect of anisotropic scattering on the radiance distribution, simulations were performed without absorption.

2.4. Geometric Light-Field Model

To assess the influence of an anisotropic radiance distribution and ice covers with spatially varying surface properties such as ponded sea ice on light availability and under-ice radiation measurements, we used a two-dimensional geometric light-field model similar to the one presented by *Frey et al.* [2011]. Planar and scalar irradiances normalized to incident fluxes were calculated for points at depth z and horizontal position x along a discretized surface. Depth z is the distance to the underside of the ice. While absorption in the water column is taken into account by an exponential decay law, scattering in the water column is neglected. This is an appropriate assumption for clear Arctic waters. Planar downwelling irradiance at each point is then defined as the sum over all contributing discrete angles θ covering a solid angle interval of $\delta\Omega$,

$$F_D(x,z) = \frac{2}{\pi} \sum_{\theta=-90°}^{90°} L(\theta,\gamma) \cdot \exp(-\kappa_{abs} \cdot d(\theta,z)) \cdot \cos\theta \cdot \delta\Omega, \tag{9}$$

with distance of the grid point to the respective surface point, d, absorption coefficient of seawater, κ_{abs}, and radiance reaching the grid cell from the respective surface point, $L(\theta)$. Seawater absorption was set to $\kappa_{abs} = 0.1 \text{ m}^{-1}$ as an average of observed broadband absorption coefficients obtained from depth profiles measured with the ROV during the campaigns. The angular dependence of the radiance exiting the ice $L(\theta)$ is derived from the Monte Carlo Simulations and is dependent on the anisotropy of the scattering coefficient γ. $L(\theta)$ was obtained by scaling the modeled $f(\theta)$ in such a way, that the planar irradiance directly under a homogenous sea-ice cover is independent of γ.

To evaluate the effect of the anisotropic scattering coefficient of sea ice on the under-ice light field, we simulated one real surface profile from station PS80/224 and various artificial surface geometries with different melt-pond concentrations and melt-pond sizes. Following *Nicolaus et al.* [2012], the transmittance of ponded and bare ice was set to 0.22 and 0.04, respectively.

KATLEIN ET AL.   5
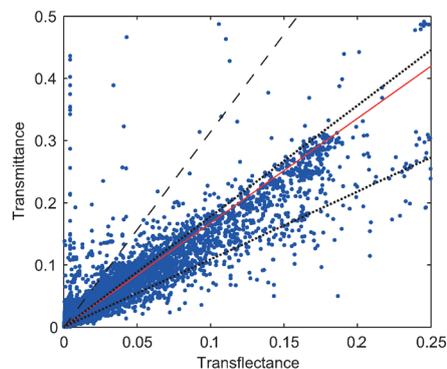
Figure 3. Transmittance F, versus transflectance L_0, for all ROV measurements conducted during IceArc 2012 (blue dots). The dashed black and red lines follow $F = C \cdot L_0$ with $C = \pi$ and $C = 1.68$, respectively. Dotted lines give the range for measured values of C (upper line: $C = 1.76$; lower line: $C = 1.09$).

3. Results

Measurements of the light field beneath Arctic sea ice resulted in values of C significantly different from π. The plot of measured transmittance versus transflectance (Figure 3) shows that C values ranged from 1.09 to 1.76 with a median of all measurements of $C = 1.68$ (Table 1). The ratio of transmittance T_F and transflectance T_L represents an observationally robust way to determine the C value. No direct dependence of single C value measurements and the distance to the ice or ice thickness was found. C values were only weakly dependent on wavelength for most of transmitted light between 400 and 600 nm where scattering dominates over absorption. Thus, C values between 400 and 600 nm are similar to those obtained from wavelength integrated broadband measurements. At wavelengths below 400 nm and larger than 600 nm, where absorption becomes more important [*Grenfell and Perovich*, 1981], C values decrease. The magnitude of this decrease varies with the strength of absorption. This independence of wavelength between 400 and 600 nm supports the hypothesis that the light field underneath sea ice is strongly influenced by the anisotropy of the scattering coefficient, as scattering in sea ice is known to be approximately independent of wavelength [*Grenfell and Hedrick*, 1983].

Results from the laboratory experiments are presented in Table 2. A clear difference of light extinction was observed between horizontal and vertical sample orientations. The extinction coefficient in the horizontal direction was up to 37% greater than in the vertical direction. Only sample 5 showed different extinction characteristics, which can be readily explained by the inhomogeneity of a thin strongly scattering layer combined with rather transparent ice.

The anisotropy of the scattering coefficient was also evident from direct measurements of the radiance distribution, obtained by rolling the ROV underneath the sea ice. The measured shape of the radiance distribution could be reproduced by model results assuming an anisotropic scattering coefficient (Figure 4).

While results for $\gamma = 0$ reproduced results from diffusion theory [*Kokhanovsky and Zege*, 2004] and the Eddington approximation [*van de Hulst*, 1980], the radiance distribution becomes increasingly downward

Table 1. Overview of Median C Values, Their Standard Deviation, and Derived γ Values Observed From ROV-Based Synchronous Measurements of Downwelling Irradiance and Radiance[a]

Station Number	Date	C	STD	$\rightarrow \gamma$	z_{ice}	Sea Ice/Clouds
PS80/224	10 Aug 2012	1.73	0.72	0.38	1.0–1.5	FYI, partly cloudy, melting
PS80/237	15 Aug 2012	1.76	2.16	0.37	1.2–2.0	FYI, overcast, melting
PS80/255	20 Aug 2012	1.70	1.90	0.40	0.7–1.2	FYI, overcast
PS80/323	4 Sep 2012	1.65	16.62	0.43	1.2–1.7	FYI, overcast
PS80/335	8 Sep 2012	1.68	6.71	0.41	0.9–1.7	FYI, overcast, roll experiment
PS80/349	18 Sep 2012	1.63	3.50	0.43	1.2–1.8	MYI, overcast
PS80/360	22 Sep 2012	1.09	13.32	0.71	1.1–1.8	FYI, overcast, roll experiment, high abundance of ice algae
PS80/384	29 Sep 2012	1.76	4.66	0.37	1.0–1.4	FYI, overcast, revisited floe of PS80/224
Median	2012	1.68	9.02	0.41		

[a]Station numbers are official Polarstern station numbers. For all stations the main ice type, as well as information on cloud cover is given.

Table 2. Physical Properties of Samples From Laboratory Experiments[a]

Sample Number	Station	Date	Density (g/cm^3)	Porosity (%)	κ_H/κ_V	C	Crystal Elongation
1	PS80/255	21 Aug 2012	0.81	12.5	1.26	2.09	5.06
2	PS80/224	10 Aug 2012	0.75	18.5	1.38	1.95	4.89
3	PS80/323	5 Sep 2012	0.83	9.4	1.16	2.22	3.73
4	PS80/335	8 Sep 2012	0.89	3.4	1.07	2.37	4.36
5[b]	PS80/349	19 Sep 2012	0.85	7.5	0.95		6.74
6	PS80/360	22 Sep 2012	0.78	15.4	1.33	2.00	4.10
7	PS80/384	29 Sep 2012	0.90	2.6	1.10	2.32	3.70

[a]Porosity was calculated from the measured density, C values are derived from the quotient of measured extinction coefficients in the horizontal and vertical direction κ_H/κ_V, Crystal elongation gives the length to width ratio of the columnar ice crystals determined from thin section analysis.
[b]Vertically inhomogeneous sample.

peaked for growing γ. To obtain an empirical equation for the radiance distribution as a function of γ, the modeled radiance distributions were fitted with a two-dimensional surface using the MATLAB Curve-Fitting toolbox ($R^2 = 0.991$), resulting in

$$f^*(\theta, \gamma) = \left(\frac{1}{3} + \frac{2}{3}\cos\theta\right)\cos\theta(1-\gamma) + \gamma\exp\left((-0.05681 \pm 0.00072)\theta\right) \tag{10}$$

with $f(\theta) = f^*/\cos\theta$. This equation allows for the calculation of the radiance distribution under an optically thick ice cover for broadband quantities or between 400 and 600 nm when extinction is dominated by scattering. To obtain C values, the modeled radiance distributions were integrated numerically and the results
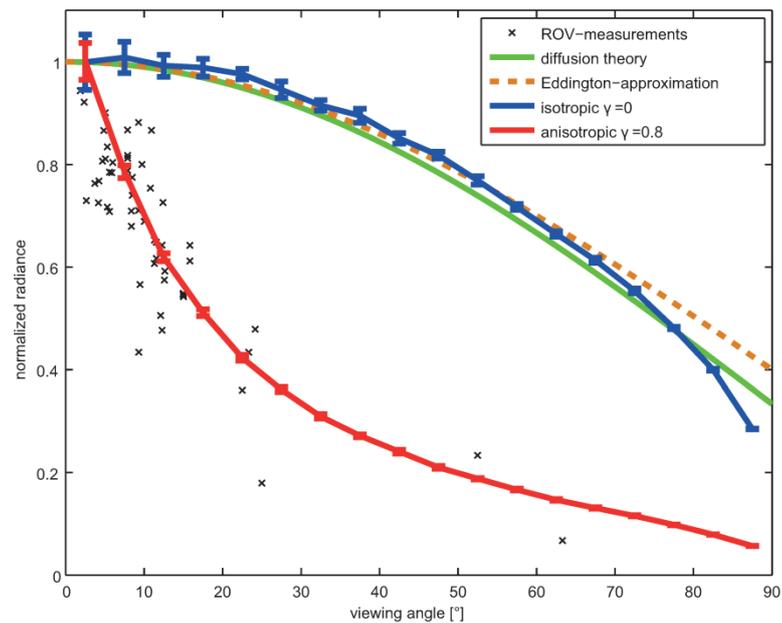
Figure 4. Angular distribution of radiance leaving the underside of sea ice. Results of the Monte Carlo model for the isotropic scattering coefficient $\gamma = 0$ (blue line) compare well with the approximation from diffusion theory (green line) and the Eddington approximation (dashed orange line). Measurements from the ROV-roll experiment on station PS80/335 on 8 Sep 2012 (crosses) are shown together with results of the model with anisotropic scattering coefficient $\gamma = 0.8$ (red line). Error bars indicate the azimuthal standard deviation of modeled photon counts.
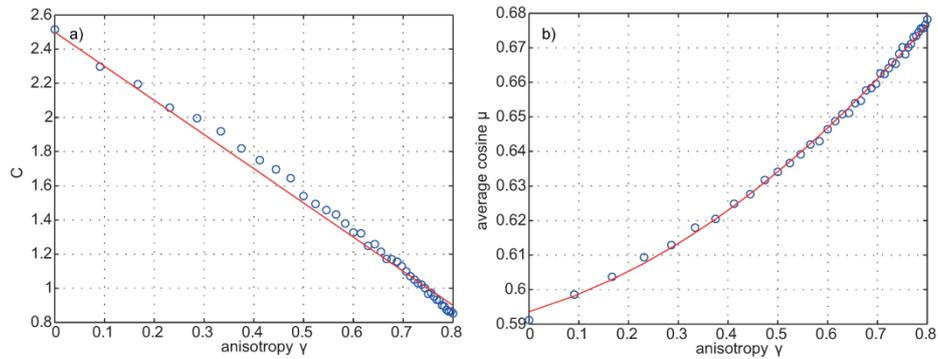
Figure 5. (a) The ratio of irradiance and radiance (C value) observed underneath the sea ice as a function of the anisotropy of the scattering coefficient γ. Blue circles show the results of Monte Carlo simulations, while the red line depicts the suggested parameterization $C = 2.5 - 2\gamma$. (b) Average cosine underneath the sea ice as a function of anisotropy γ.

plotted against γ (Figure 5). Surprisingly, C values could be described by a simple linear expression ($R^2 = 0.990$),

$$C = 2.5 - 2\gamma. \qquad (11)$$

Equation (11) can be used to determine the C value of a radiance distribution emitted from an optically thick ice cover with the known anisotropy of the scattering coefficient γ. This parameterization shows that the C value does not reach π even for isotropic scattering. In fact, $C = 2.5$ for isotropic media is in agreement with the theoretical C values derived from both photon diffusion theory [*Kokhanovsky and Zege*, 2004] and the Eddington approximation [*van de Hulst*, 1980] of 2.49 and 2.51, respectively.

The consequences of an anisotropic radiance distribution exiting the sea ice for the under-ice light field were explored with the two-dimensional geometric light-field model. Figure 6 shows the irradiance field calculated for a 450 m long profile of pond cover obtained from an aerial picture of the ice station PS80/224 on 9 August 2012. The relative differences in downwelling irradiance between $\gamma = 0$ and $\gamma = 0.6$ are in the range of 10% and would thus be accessible to measurements as measurement uncertainties are smaller
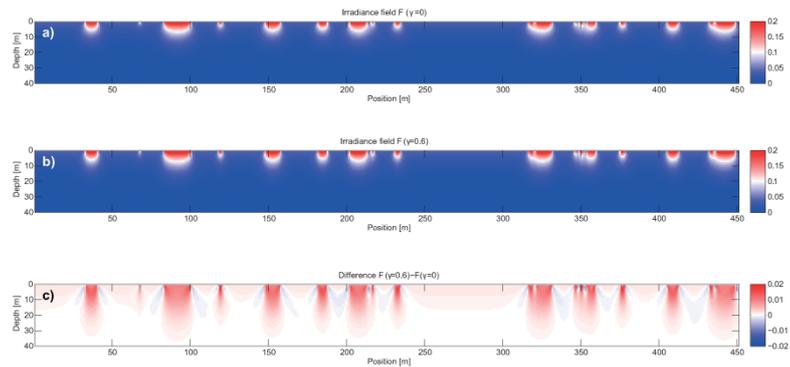
Figure 6. (a) Irradiance field calculated for a 450 m long horizontal profile of pond coverage taken from an aerial picture of ice station PS80/224. Transmittances for ponds and bare ice were 0.22 and 0.04, respectively. (b) Same irradiance field but calculated for anisotropic scattering coefficient in sea ice with $\gamma = 0.6$. (c) Difference between the irradiance fields resulting from anisotropic and isotropic scattering coefficient of the sea ice.
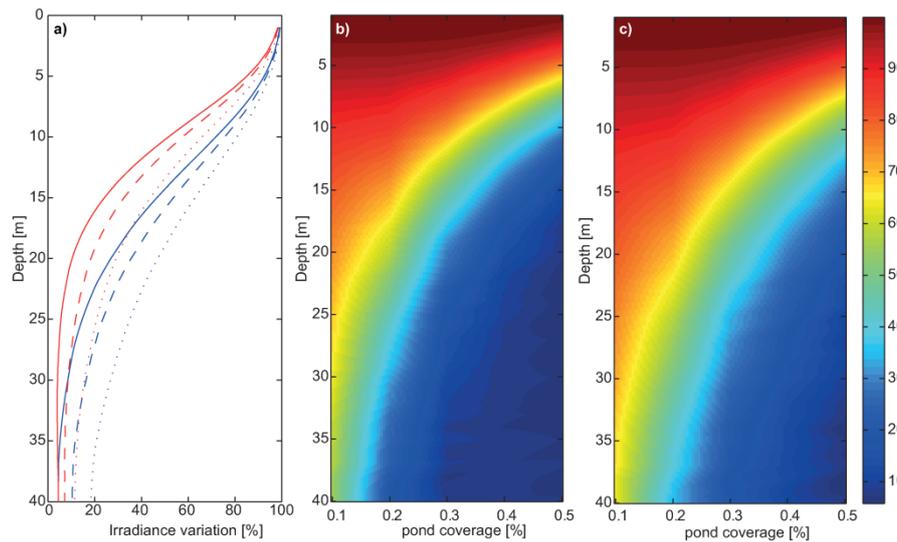
Figure 7. (a) Depth-dependent irradiance variation β for different anisotropies ($\gamma = 0$ solid line, $\gamma = 0.3$ dashed line, $\gamma = 0.6$ dotted line), a regular ice cover with pond coverages of 30% (blue) and 40% (red) and a pond size of 7.5 m. Irradiance variation at depth in dependence of pond coverage for a pond size of 7.5 m, (b) $\gamma = 0$ and (c) $\gamma = 0.6$, respectively.

[*Nicolaus and Katlein*, 2013; *Nicolaus et al.*, 2010a]. Irradiance levels under melt ponds are generally higher for large γ. This effect is especially pronounced close to the surface up to a depth of approximately 10 m, where the differences are greatest.

Under-ice measurements of radiation under heterogeneous sea-ice covers are highly dependent on the distance between sensors and the ice underside. While radiance sensors provide good spatial resolution even when operated at depth, the ability to detect spatial variability decreases drastically with depth for irradiance sensors. The detectable variability is dependent on pond size, pond fraction, extinction in the water column, and the light-field geometry represented by C. We quantified the relative range of variability at a depth z by

$$\beta^*(z) = \frac{\max(F(z)) - \min(F(z))}{\max(F(z))}. \tag{12}$$

For general comparison, this quantity was scaled with the variability at the sea-ice bottom,

$$\beta(z) = \frac{\beta^*(z)}{\beta^*(z=0)}. \tag{13}$$

Figure 7a shows examples of how the irradiance variability is propagated into the water column for a pond size of 7.5 m and pond fractions of 0.3 and 0.4. While at 20 m depth, 26.9% (10.3%) of the surface variability can be detected assuming $\gamma = 0$, up to 47.0% (29.1%) is detectable if $\gamma = 0.6$ and the pond coverage is 30% (40%). Higher values of γ lead to a deeper propagation of the variability through the water column. It is necessary to assess the variability observable from a certain depth to plan ROV and AUV campaigns. While 90% of the variability can be observed within a distance of 4 m to the ice bottom for all modeled cases with pond sizes bigger than 7.5 m, the spatial variability of ice optical properties can be assessed at depths in excess of 10 m only for ponds larger than 15 m. Large ponds, small pond coverage, and high values of γ generally lead to a better detectability of surface variations at depth. Small ponds, large pond coverage and low values of γ decrease the ability of irradiance sensors to detect surface variability at depth.

4. Discussion

4.1. Anisotropy of the Light Field

Due to the absence of significant scattering in the underlying water, the radiance distribution underneath sea ice is not isotropic. This is predicted by the theory of radiative transfer [*Kokhanovsky and Zege*, 2004; *van de Hulst*, 1980]. Our results clearly confirm that the radiance distribution underneath sea ice is not isotropic. The error introduced by the isotropic assumption is not negligible even if the scattering coefficient of the ice is isotropic ($\gamma = 0$) and can be easily determined using the C value. When converting radiance to planar irradiance, the assumption of an isotropic radiance field overestimates planar irradiance by a factor π/C. For $\gamma = 0$, this is already an overestimation of 25%. For realistic sea-ice cases with $\gamma = 0.3$ (0.6) planar irradiance is overestimated by 65% (142%). This error is even bigger for scalar irradiance. For $\gamma = 0$, scalar irradiance is overestimated by 49%, while the overestimate is 103% (213%) for $\gamma = 0.3$ (0.6). Thus, the assumption of an isotropic radiance field should not be used to estimate irradiance from radiance. Instead, a C value ≤ 2.5 should be used. Both our modeled $C = 1.3$ for $\gamma = 0.6$ as well as our measured $C = 1.68$ ($1.09 \ldots 1.76$) values are similar to the C value of 1.78 that we reconstructed from the radiance distribution measurements of *Trodahl et al.* [1989].

4.2. Influence of an Heterogeneous Sea-Ice Cover

Of importance for the light field beneath sea ice is the influence of structural inhomogeneity on the C value. Under small areas with high light transmittance, such as melt ponds or cracks in the ice, the radiance distribution is strongly downward-peaked resulting in a lower C value. Under dark patches such as pressure ridges, more light is received from the sides than from above, increasing the C value. Thus, the C value measured from the ratio of irradiance to radiance is only related to the anisotropy parameter of the ice under an ice cover which is sufficiently homogenous or when looking at the median of observations with large spatial extent. This geometric effect is the cause for the scatter in Figure 3, where datapoints with $C > \pi$ are related to measurements under bright patches

4.3. Estimating C

Our results show that the C value has significant implications for the interpretation of under-ice radiation measurements. Nevertheless, it is challenging to estimate C from the observations of ice properties. The horizontal extinction of light was found to be increasing with bulk salinity [*Zhao et al.*, 2010] which is an indicator of brine volume. *Trodahl et al.* [1989] observed that the anisotropy of the scattering coefficient is dependent on salinity and brine volume, identifying brine channels as the main source of the anisotropy. In our case of melting summer sea ice, brine volume can be approximated by the air volume of the samples as almost all pores are filled with air after sampling. We found a clear dependence of γ on porosity ($R^2 = 0.956$) in our laboratory experiments,

$$\gamma(\Phi) = 2.43 - 0.026 \ \Phi, \tag{14}$$

indicating that sea ice exhibits a stronger anisotropy of the scattering coefficient with increasing air volume. While the small number of samples did not allow us to investigate the dependence of γ on the columnar texture in depth, we found that the anisotropy tends to increase with the length to width ratio of ice crystals determined by the analysis of vertical thin sections ($R^2 = 0.29$).

In addition to microstructural properties, the C value is expected to depend on ice optical thickness and on the presence of absorbing material. The radiance distribution under sea ice is affected by absorption from ice algae [*Petrich et al.*, 2012a; *Trodahl et al.*, 1989]. This could explain the low C value of $C = 1.09$ at station PS80/360, where high abundances of ice algae in and below the ice were observed with the ROV cameras. Numerical analyses presented are valid for optically thick ice only. In optically thin ice, the transmitted radiance distribution depends on the incident light field. Thus, the presented results cannot be directly applied to estimate the radiance distribution under thin ice (e.g., nilas) and thus differ from the results of *Schoonmaker et al.* [1989] as well as *Voss et al.* [1992].

4.4. Multiple Scattering

Trodahl et al. [1989] introduced the concept of the anisotropic scattering coefficient in sea ice as a necessity to describe their experimental results. The field measurements of *Pegau and Zaneveld* [2000] could neither prove nor disprove the concept. In the classical works on scattering in sea ice, small samples of only 1–2

cm^3 were used [*Grenfell and Hedrick*, 1983; *Miller et al.*, 1997]. A slight dependence of scattering on sample orientation had been found but was considered insignificant. Our samples were significantly bigger, rendering anisotropic extinction more obvious.

We suggest that the anisotropy of the scattering coefficient originates from a nonrandom but ordered distribution of scatterers along brine inclusion planes and scattering at brine channel walls. Thus, the anisotropy should be more pronounced in columnar ice, while the less ordered texture of granular ice should lead to a weak or even no anisotropy of the scattering coefficient. As the spacing of brine inclusion planes and the size of brine channel systems is on the mm to cm scale [*Timco and Weeks*, 2010], the anisotropy of the scattering coefficient becomes observable only for larger samples when multiple scattering is present. As a result, this anisotropy is not dependent on the phase function of a single scattering event. The systematic configuration of brine inclusions causing anisotropy of the scattering coefficient also causes anisotropy of other physical properties of columnar sea ice such as tensile strength [*Timco and Weeks*, 2010] and electrical resistivity [*Jones et al.*, 2012].

We conclude from our results that the anisotropic nature of scattering is important for radiative transfer in sea ice and that not all apparent optical properties can be simulated correctly if anisotropy of the scattering coefficient is neglected. In addition, anisotropic light fields have to be taken into account in the simulation of horizontally inhomogeneous ice covers and the angular radiance distribution.

4.5. Brine Drainage
The laboratory measurements have been affected by an almost complete loss of brine. This problem applies to all sea ice sampling in summer, when large brine channels cause an immediate loss of pore water during the extraction of ice cores. We expect our drained samples to show higher scattering and extinction than expected for submerged ice samples because the contrast in refractive index is higher for air in ice than for brine in ice. Nevertheless, we do not expect a significant effect on the measured anisotropy of the scattering coefficient, as the geometry of scattering interfaces like brine channel walls are not influenced by this drainage. While the phase function of single scattering events and the magnitude of the scattering coefficients depend on the refractive index, the anisotropy of the scattering coefficient should be independent of the refractive index as it is determined by the configuration of scatterers.

4.6. Field Measurements of the Radiance Distribution
It is difficult to directly relate laboratory measurements to large-scale ROV measurements as the sea ice texture varies considerably within one ice station. Direct measurements of the angular radiance distribution obtained from rolling the ROV underneath the ice (as shown in Figure 4) can only be interpreted qualitatively, as this is a demanding operation for the ROV pilot due to considerable under-ice currents and thus data quality is low. The measurements are influenced by various factors such as horizontal displacements, rotation of the ROV, inaccurate inclination readings and variations in the not perfectly homogenous ice cover. These and other uncertainties are also discussed in *Nicolaus and Katlein* [2013]. The determination of C values from the irradiance to radiance ratio is dependent on the angular sensitivity of the radiance sensor. As a radiance sensor collects light from a finite solid angle, but radiance is mathematically defined for an infinitely small solid angle, the radiance distribution cannot be sampled correctly, when it varies significantly within the field of view of the radiance sensor. For the downward-peaked radiance distributions underneath sea ice this can result in an overestimation of the C value. This bias can be estimated for a radiance distribution given by equation (10): For $\gamma = 0.6$, the radiance distribution varies up to 10% within the sensor footprint of $6°$. This can still be regarded as narrow enough, as the absolute calibration uncertainty of the used spectral radiometers is within the order of 5–10% [*Nicolaus et al.*, 2010a]. C values obtained with radiance sensors of a much larger field of view will be significantly skewed toward higher values.

Our simulations were consistent with measurement procedures as radiance distributions were obtained by binning photons exiting the underside of the ice in bins of $5°$.

4.7. Scalar Irradiance
Knowledge about the radiance distribution is not only necessary to convert radiance to planar irradiance to determine energy fluxes but also necessary for the conversion of planar irradiance data into scalar irradiance relevant for photosynthesis. For the conversion between planar and scalar irradiance measurements, the influence of anisotropic radiance distributions can be described by the mean cosine $\bar{\mu}_d$ of the downwelling light field [*Maffione and Jaffe*, 1995],

$$\bar{\mu}_d = \frac{F}{F_{2\pi}} = \frac{\int_{\phi=0}^{2\pi}\int_{\theta=0}^{\pi/2} L(\theta,\phi)\ \cos\theta\ \sin\theta\ d\theta d\phi}{\int_{\phi=0}^{2\pi}\int_{\theta=0}^{\pi/2} L(\theta,\phi)\ \sin\theta\ d\theta d\phi} \tag{15}$$

From the results of our Monte Carlo simulations, we found for the light field right beneath sea ice $\bar{\mu}_d = 0.59$ and $\bar{\mu}_d = 0.65$ for $\gamma = 0$ and $\gamma = 0.6$, respectively. The dependence of $\bar{\mu}_d(\gamma)$ is shown in Figure 5b and could be fitted with the polynomial approximation ($R^2 = 0.998$)

$$\bar{\mu}_d(\gamma) = 0.5936 + 0.0433\ \gamma + 0.0757\ \gamma^2. \tag{16}$$

The mean cosine of the downwelling light field in sea ice has not been studied in depth. *Ehn and Mundy* [2013] use $\bar{\mu}_d = 0.7$ based on observations and modeling [*Ehn et al.*, 2008b], while *Arrigo et al.* [1991] used $\bar{\mu}_d = 0.656$. These numbers agree well with the results of our modeled radiance distributions for sea ice with anisotropic scattering coefficient $\gamma > 0.6$.

Combining equations (4) and (16) one can derive the following relation between radiance and spherical irradiance,

$$F_{2\pi} = \frac{F}{\bar{\mu}_d} = \frac{C \cdot L_0}{\bar{\mu}_d}. \tag{17}$$

Both, C and $\bar{\mu}_d$ are scalars describing the radiance distribution as a function of the microstructural parameter γ.

4.8. Implications for Field Measurements
The consequences of the downward-peaked radiance distribution on the conversion of radiance measurements to irradiance discussed above are important for future radiation measurements under sea ice. To obtain high-spatial coverage, light measurements will more often be conducted from submersible sensor platforms such as ROVs or AUVs. Due to the collision hazard with under-ice topography, large platforms will have to operate at a certain minimum distance beneath the ice. When using irradiance sensors this distance will lead to a strong areal averaging of light levels and a loss of spatial resolution. However, the spatial variability is important for the small-scale assessment of the energy and mass balance of the ice cover and determination of the light available to ice associated biota for primary production. Hence, missions focusing on the spatial variability of light conditions will need to use radiance sensors to observe the spatial variability of light conditions from depths >10 m. These data can then be transferred into under-ice irradiance readings with conversion methods based on the C value presented above.

Frey et al. [2011] described irradiance maxima under bare ice adjacent to ponds, caused by the large area influencing an irradiance measurement underneath the ice. They reproduced their measurements using a geometric light-field model similar to ours but modeled maximum positions were up to 2 m shallower than the measured position of the irradiance maximum. This discrepancy could be at least partly explained by their assumption of an isotropic light field.

4.9. Future Work
For a better understanding of radiative transfer processes in sea ice and light availability underneath sea ice further investigations of the radiance distribution in and underneath sea ice are necessary. The combination of Monte Carlo models [*Petrich et al.*, 2012a; *Trodahl et al.*, 1987] with three-dimensional measurements of sea-ice microstructure by X-ray microtomographs [*Golden et al.*, 2007; *Kaempfer et al.*, 2007] could reveal more details about microscopic scattering properties. Radiance cameras [*Antoine et al.*, 2012] deployed underneath sea ice would be able to provide a more detailed measurement of the under-ice light field.

5. Conclusions
From the synopsis of our field and lab experiments and modeling results, we conclude that the radiance distribution underneath sea ice is not isotropic. In fact the radiance distribution is even more downward directed than predicted by isotropic radiative transfer theory, because scattering in sea ice is anisotropic.

KATLEIN ET AL. 12

AGU **Journal of Geophysical Research: Oceans** 10.1002/2013JC009502

These results show that the commonly used assumption of an isotropic under-ice light-field leads to significant errors in the conversion between radiance and irradiance measurements. We introduced the C value as a practical measure of light-field geometry. Theoretical and numerical considerations show that $C \leq 2.5$ should be used rather than $C = \pi$ in the absence of further information about anisotropic scattering of sea ice, if scattering properties of the sea ice are known and there is no significant contribution of absorption, C can be estimated from either equations (11) and (14) or microstructural analysis. While one would expect a C value close to 2.5 for granular ice, smaller values between 1.3 and 2.3 can be assumed for columnar ice. For cold and highly columnar winter-sea ice even lower values could occur. Our geometric light-field model shows that a conversion of radiance to irradiance data will become necessary for light measurements conducted more than 4 m away from the ice underside if the spatial variability is of interest. As a consequence, ROV-based measurements of the variability of under-ice irradiance should be conducted within 4 m distance of the ice underside. To be able to measure the spatial variability of light underneath the sea ice, future AUV and submarine missions will have to use radiance sensors and the suggested conversions in addition to the simultaneous use of irradiance sensors for the quantification of shortwave energy fluxes at depth. Knowledge of the angular radiance distribution also enables for a correct conversion of measurements of planar irradiance to scalar irradiance determining the light available for photosynthetic activity.

References

Antoine, D., et al. (2012), Underwater radiance distributions measured with miniaturized multispectral radiance cameras, *J. Atmos. Oceanic Technol.*, *30*(1), 74–95, doi:10.1175/JTECH-D-11-00215.1.

Arrigo, K. R., C. W. Sullivan, and J. N. Kremer (1991), A biooptical model of Antarctic sea ice, *J. Geophys. Res.*, *96*(C6), 10,581–10,592, doi:10.1029/91JC00455.

Bélanger, S., S. A. Cizmeli, J. Ehn, A. Matsuoka, D. Doxaran, S. Hooker, and M. Babin (2013), Light absorption and partitioning in Arctic Ocean surface waters: Impact of multiyear ice melting, *Biogeosciences*, *10*(10), 6433–6452, doi:10.5194/bg-10-6433-2013.

Cox, G. F. N., and W. F. Weeks (1983), Equations for determining the gas and brine volumes in sea-ice samples, *J. Glaciol.*, *29*(102), 306–316.

Ehn, J. K., and C. J. Mundy (2013), Assessment of light absorption within highly scattering bottom sea ice from under-ice light measurements: Implications for Arctic ice algae primary production, *Limnol. Oceanogr. Methods*, *58*(3), 893–902, doi:10.4319/lo.2013.58.3.0893.

Ehn, J. K., C. J. Mundy, and D. G. Barber (2008a), Bio-optical and structural properties inferred from irradiance measurements within the bottommost layers in an Arctic landfast sea ice cover, *J. Geophys. Res.*, *113*, C03S03, doi:10.1029/2007JC004194.

Ehn, J. K., T. N. Papakyriakou, and D. G. Barber (2008b), Inference of optical properties from radiation profiles within melting landfast sea ice, *J. Geophys. Res.*, *113*, C09024, doi:10.1029/2007JC004656.

Ehn, J. K., C. J. Mundy, D. G. Barber, H. Hop, A. Rossnagel, and J. Stewart (2011), Impact of horizontal spreading on light propagation in melt pond covered seasonal sea ice in the Canadian Arctic, *J. Geophys. Res.*, *116*, C00G02, doi:10.1029/2010JC006908.

Eicken, H., H. R. Krouse, D. Kadko, and D. K. Perovich (2002), Tracer studies of pathways and rates of meltwater transport through Arctic summer sea ice, *J. Geophys. Res.*, *107*(C10), 8046, doi:10.1029/2000JC000583.

Frey, K. E., D. K. Perovich, and B. Light (2011), The spatial distribution of solar radiation under a melting Arctic sea ice cover, *Geophys. Res. Lett.*, *38*, L22501, doi:10.1029/2011GL049421.

Golden, K. M., H. Eicken, A. L. Heaton, J. Miner, D. J. Pringle, and J. Zhu (2007), Thermal evolution of permeability and microstructure in sea ice, *Geophys. Res. Lett.*, *34*, L16501, doi:10.1029/2007GL030447.

Grenfell, T. C. (1977), The optical properties of ice and snow in the arctic basin, *J. Glaciol.*, *18*(80), 445–463.

Grenfell, T. C., and D. Hedrick (1983), Scattering of visible and near infrared radiation by NaCl ice and glacier ice, *Cold Reg. Sci. Technol.*, *8*(2), 119–127, doi:10.1016/0165-232x(83)90003-4.

Grenfell, T. C., and D. K. Perovich (1981), Radiation absorption coefficients of polycrystalline ice from 400–1400 nm, *J. Geophys. Res.*, *86*(NC8), 7447–7450, doi:10.1029/JC086iC08p07447.

Haas, C., A. Pfaffling, S. Hendricks, L. Rabenstein, J.-L. Etienne, and I. Rigor (2008), Reduced ice thickness in Arctic Transpolar Drift favors rapid ice retreat, *Geophys. Res. Lett.*, *35*, L17501, doi:10.1029/2008GL034457.

Haines, E. M., R. G. Buckley, and H. J. Trodahl (1997), Determination of the depth dependent scattering coefficient in sea ice, *J. Geophys. Res.*, *102*(C1), 1141–1151, doi:10.1029/96JC02861.

Hamre, B., J. G. Winther, S. Gerland, J. J. Stamnes, and K. Stamnes (2004), Modeled and measured optical transmittance of snow-covered first-year sea ice in Kongsfjorden, Svalbard, *J. Geophys. Res.*, *109*, C10006, doi:10.1029/2003JC001926.

Jaffé, A. (1960), Über Strahlungseigenschaften des Gletschereises, *Arch. Meteorol. Geophys. Biokl. B.*, *10*(3), 376–395, doi:10.1007/BF02243201.

Jones, K. A., M. Ingham, and H. Eicken (2012), Modeling the anisotropic brine microstructure in first-year Arctic sea ice, *J. Geophys. Res.*, *117*, C02005, doi:10.1029/2011JC007607.

Kaempfer, T. U., M. A. Hopkins, and D. K. Perovich (2007), A three-dimensional microstructure-based photon-tracking model of radiative transfer in snow, *J. Geophys. Res.*, *112*, D24113, doi:10.1029/2006JD008239.

Kokhanovsky, A. A., and E. P. Zege (2004), Scattering optics of snow, *Appl. Opt.*, *43*(7), 1589–1602, doi:10.1364/AO.43.001589.

Krembs, C., H. Eicken, and J. W. Deming (2011), Exopolymer alteration of physical properties of sea ice and implications for ice habitability and biogeochemistry in a warmer Arctic, *Proc. Natl. Acad. Sci. U. S. A.*, *108*(9), 3653–3658, doi:10.1073/pnas.1100701108.

Leu, E., J. Wiktor, J. E. Soreide, J. Berge, and S. Falk-Petersen (2010), Increased irradiance reduces food quality of sea ice algae, *Mar. Ecol. Prog. Ser.*, *411*, 49–60, doi:10.3354/meps08647.

Light, B., G. A. Maykut, and T. C. Grenfell (2003), A two-dimensional Monte Carlo model of radiative transfer in sea ice, *J. Geophys. Res.*, *108*(C7), 3219, doi:10.1029/2002JC001513.

Light, B., T. C. Grenfell, and D. K. Perovich (2008), Transmission and absorption of solar radiation by Arctic sea ice during the melt season, *J. Geophys. Res.*, *113*, C03023, doi:10.1029/2006JC003977.

🌀AGU **Journal of Geophysical Research: Oceans** 10.1002/2013JC009502

Maffione, R. A., and J. S. Jaffe (1995), The average cosine due to an isotropic light source in the ocean, *J. Geophys. Res., 100*(C7), 13,179–13,192, doi:10.1029/95JC00461.

Maffione, R. A., J. M. Voss, and C. D. Mobley (1998), Theory and measurements of the complete beam spread function of sea ice, *Limnol. Oceanogr., 43*(1), 34–43, doi:10.4319/lo.1998.43.1.0034.

Maslanik, J. A., C. Fowler, J. Stroeve, S. Drobot, J. Zwally, D. Yi, and W. Emery (2007), A younger, thinner Arctic ice cover: Increased potential for rapid, extensive Arctic sea-ice loss, *Geophys. Res. Lett., 34*, L24501, doi:10.1029/2007GL032043.

Miller, D., M. S. QuinbyHunt, and A. J. Hunt (1997), Laboratory studies of angle- and polarization-dependent light scattering in sea ice, *Appl. Opt., 36*(6), 1278–1288, doi:10.1364/ao.36.001278.

Mobley, C. D., G. F. Cota, T. C. Grenfell, R. A. Maffione, W. S. Pegau, and D. K. Perovich (1998), Modeling light propagation in sea ice, *IEEE Trans. Geosci. Remote Sens., 36*(5), 1743–1749, doi:10.1109/36.718642.

Mundy, C. J., D. G. Barber, and C. Michel (2005), Variability of snow and ice thermal, physical and optical properties pertinent to sea ice algae biomass during spring, *J. Mar. Syst., 58*(3–4), 107–120, doi:10.1016/j.jmarsys.2005.07.003.

Nicolaus, M., and C. Katlein (2013), Mapping radiation transfer through sea ice using a remotely operated vehicle (ROV), *Cryosphere, 7*(3), 763–777, doi:10.5194/tc-7-763-2013.

Nicolaus, M., S. R. Hudson, S. Gerland, and K. Munderloh (2010a), A modern concept for autonomous and continuous measurements of spectral albedo and transmittance of sea ice, *Cold Reg. Sci. Technol., 62*(1), 14–28, doi:10.1016/j.coldregions.2010.03.001.

Nicolaus, M., S. Gerland, S. R. Hudson, S. Hanson, J. Haapala, and D. K. Perovich (2010b), Seasonality of spectral albedo and transmittance as observed in the Arctic Transpolar Drift in 2007, *J. Geophys. Res., 115*, C11011, doi:10.1029/2009JC006074.

Nicolaus, M., C. Katlein, J. Maslanik, and S. Hendricks (2012), Changes in Arctic sea ice result in increasing light transmittance and absorption, *Geophys. Res. Lett., 39*, L24501, doi:10.1029/2012GL053738.

Pegau, W. S., and J. R. V. Zaneveld (2000), Field measurements of in-ice radiance, *Cold Reg. Sci. Technol., 31*(1), 33–46, doi:10.1016/s0165-232x(00)00004–5.

Perovich, D. K. (1990), Theoretical estimates of light reflection and transmission by spatially complex and temporally varying sea ice covers, *J. Geophys. Res., 95*(C6), 9557–9567, doi:10.1029/JC095iC06p09557.

Perovich, D. K. (2011), The changing Arctic sea ice cover, *Oceanography, 24*(3), 162–173.

Perovich, D. K., K. F. Jones, B. Light, H. Eicken, T. Markus, J. Stroeve, and R. Lindsay (2011), Solar partitioning in a changing Arctic sea-ice cover, *Ann. Glaciol., 52*(57), 192–196.

Petrich, C., M. Nicolaus, and R. Gradinger (2012a), Sensitivity of the light field under sea ice to spatially inhomogeneous optical properties and incident light assessed with three-dimensional Monte Carlo radiative transfer simulations, *Cold Reg. Sci. Technol., 73*, 1–11, doi:10.1016/j.coldregions.2011.12.004.

Petrich, C., H. Eicken, J. Zhang, J. Krieger, Y. Fukamachi, and K. I. Ohshima (2012b), Coastal landfast sea ice decay and breakup in northern Alaska: Key processes and seasonal prediction, *J. Geophys. Res., 117*, C02003, doi:10.1029/2011JC007339.

Roesel, A., and L. Kaleschke (2012), Exceptional melt pond occurrence in the years 2007 and 2011 on the Arctic sea ice revealed from MODIS satellite data, *J. Geophys. Res., 117*, C05018, doi:10.1029/2011JC007869.

Roulet, R. R., G. A. Maykut, and I. C. Grenfell (1974), Spectrophotometers for the measurement of light in polar ice and snow, *Appl. Opt., 13*(7), 1652–1659, doi:10.1364/ao.13.001652.

Schoonmaker, J. S., K. J. Voss, and G. D. Gilbert (1989), Laboratory measurements of optical beams in young sea ice, *Limnol. Oceanogr., 34*(8), 1606–1613.

Serreze, M. C., M. M. Holland, and J. Stroeve (2007), Perspectives on the Arctic's shrinking sea-ice cover, *Science, 315*(5818), 1533–1536, doi:10.1126/science.1139426.

Timco, G. W., and W. F. Weeks (2010), A review of the engineering properties of sea ice, *Cold Reg. Sci. Technol., 60*(2), 107–129, doi:10.1016/j.coldregions.2009.10.003.

Trodahl, H. J., R. G. Buckley, and S. Brown (1987), Diffusive transport of light in sea ice, *Appl. Opt., 26*(15), 3005–3011, doi:10.1364/AO.26.003005.

Trodahl, H. J., R. G. Buckley, and M. Vignaux (1989), Anisotropic light radiance in and under sea ice, *Cold Reg. Sci. Technol., 16*(3), 305–308, doi:10.1016/0165-232x(89)90030-x.

van de Hulst, H. C. (1980), *Multiple Light Scattering: Tables, Formulas, and Applications*, Academic, New York.

Voss, J. M., R. C. Honey, G. D. Gilbert, and R. R. Buntzen (1992), Measuring the point-spread function of sea ice in situ, in *Proceedings of the SPIE Ocean Optics XI, 1750*, doi:10.1117/12.140682.

Zeebe, R. E., H. Eicken, D. H. Robinson, D. WolfGladrow, and G. S. Dieckmann (1996), Modeling the heating and melting of sea ice through light absorption by microalgae, *J. Geophys. Res., 101*(C1), 1163–1181, doi:10.1029/95JC02687.

Zhao, J. P., T. Li, D. Barber, J. P. Ren, M. Pucko, S. J. Li, and X. Li (2010), Attenuation of lateral propagating light in sea ice measured with an artificial lamp in winter Arctic, *Cold Reg. Sci. Technol., 61*(1), 6–12, doi:10.1016/j.coldregions.2009.12.006.

KATLEIN ET AL. 14

6. Paper 4

DISTRIBUTION OF ALGAL AGGREGATES UNDER SUMMER SEA ICE IN THE CENTRAL ARCTIC

Christian Katlein[1], Mar Fernández-Méndez[1,2], Frank Wenzhöfer[1,2], Marcel Nicolaus[1]

[1]Alfred-Wegener-Institut Helmholtz-Zentrum für Polar- und Meeresforschung, Bussestr. 24, 27570 Bremerhaven, Germany

[2]Max Planck Institute for Marine Microbiology, 28359 Bremen, Germany

ORIGINAL PAPER

Distribution of algal aggregates under summer sea ice in the Central Arctic

Christian Katlein · Mar Fernández-Méndez ·
Frank Wenzhöfer · Marcel Nicolaus

Abstract The sea ice cover of the Arctic Ocean has changed dramatically in the last decades, and the resulting consequences for the sea-ice-associated eco-system remain difficult to assess. Algal aggregates underneath sea ice are of great importance for the ice-associated ecosystem and the pelagic-benthic coupling. However, the frequency and distribution of their occurrence is not well quantified. During the IceArc expedition (ARK-27/3) of RV Polarstern in late summer 2012, we observed different types of algal aggregates floating underneath various ice types in the Central Arctic basins. We investigated the spatial distribution of ice algal aggregates and quantified their biomass, using under-ice image surveys obtained by an upward-looking camera on a remotely operated vehicle. On basin scale, filamentous aggregates of *Melosira arctica* are more frequently found in the inner part of the Central Arctic pack ice, while rounded aggregates mainly formed by pennate diatoms are found closer to the ice edge, under melting sea ice. On the scale of an ice floe, the distribution of algal aggregates in late summer is mainly regulated by the topography of the ice underside, with aggregates accumulating in dome-shaped structures and at the edges of pressure ridges. The average biomass of the aggregates from our sites and season was 0.1–6.0 mg C m^{-2}. However, depending on the approach used, differences in orders of magnitude for biomass estimates may occur. This highlights the difficulties of upscaling observations and comparing results from surveys conducted using different methods or on different spatial scales.

Keywords Sea ice algae · Algal assemblages · Size distribution · *Melosira arctica* filaments · Image processing · Remotely operated vehicle

C. Katlein (✉) · M. Fernández-Méndez · F. Wenzhöfer ·
M. Nicolaus
Alfred-Wegener-Institut Helmholtz-Zentrum für Polar- und
Meeresforschung, Bussestr. 24, 27570 Bremerhaven, Germany
e-mail: ckatlein@awi.de

M. Fernández-Méndez · F. Wenzhöfer
Max Planck Institute for Marine Microbiology, 28359 Bremen,
Germany

Introduction

The Arctic Ocean has changed dramatically in recent decades. Changes of physical processes in the climate system—such as decreased sea ice extent (Serreze et al. 2007) and thickness (Haas et al. 2008; Kwok and Roth-rock 2009), the trend from multi-year to younger first-year sea ice (Maslanik et al. 2007), a longer melt season (Markus et al. 2009), increased melt-pond coverage (Roesel and Kaleschke 2012), and increased light trans-mittance through the ice (Nicolaus et al. 2012)—are affecting the sea ice ecosystem (Arrigo et al. 2008; Lee et al. 2011; Arrigo 2014). Assessing the consequences of these changes in sea ice ecosystems is difficult, as observations in the ice-covered Arctic Ocean are techni-cally challenging, and we are lacking a comprehensive baseline—especially in the central basins—to make the effects of change apparent.

Sea ice harbors a complex diversity of life, both in its brine channels and associated with its ice-water interface, which is strongly influenced by the physical conditions present (Horner et al. 1992; Legendre et al. 1992; Krembs

et al. 2002; Mundy et al. 2005; Quillfeldt et al. 2009). Sea ice algae play an important role in the sea ice ecosystem, supporting a substantial fraction of total primary productivity (Gosselin et al. 1997), potentially seeding the under-ice phytoplankton bloom in spring (Wassmann and Reigstad 2011), and providing an important food source for the zooplankton (Leu et al. 2010, 2011). Changed melting conditions and increased light availability are also expected to affect the life conditions of sea ice algae (Lee et al. 2011; Leu et al. 2010). When ice algae are released to the water column because of ice melt, they are inherently prone to aggregation due to the high production of transparent exopolymers (Riebesell et al. 1991; Krembs et al. 2011). Aggregation can then lead to either a rapid sedimentation of biomass on the seafloor (Boetius et al. 2013) or a prolonged suspension underneath the ice (Assmy et al. 2013) due to oxygen entrapment within the aggregates (Fernández-Méndez et al. 2014). In this paper, the term "algal aggregates" refers to macroscopic (>1 cm) mostly free-floating aggregations mainly formed by typical sea-ice-associated algae such as those described by Fernández-Méndez et al. (2014). These aggregates have previously been described in the literature using various names such as sub-ice assemblages, algal filaments or aggregations (Nansen 1906; Melnikov and Bondarchuk 1987; Horner et al. 1992; Gutt 1995). Despite the long history of observations of algal aggregates under Arctic sea ice, little is known about the factors controlling their spatial distribution on both floe and basin scales.

Observations of ice algal aggregates are sparse, and usually cover only a small spatial range, as it is a great challenge to gather spatial datasets underneath sea ice. Up to now, most studies have been based on diving operations (Melnikov and Bondarchuk 1987; Syvertsen 1991; Melnikov 1997; Poulin et al. 2014; Glud et al. 2014). The increased use of remotely operated vehicles (ROVs) in polar regions, along with the recent advances in digital underwater imaging, has now enabled us to perform detailed observations of under-ice environments on a larger spatial scale (Gutt 1995; Werner and Lindemann 1997; Perovich et al. 1998; Ambrose et al. 2005; Gradinger and Bluhm 2010; Nicolaus and Katlein 2013).

The objective of this paper is to quantify the amount and distribution of algal aggregates underneath Arctic summer sea ice on floe and basin scales using ROV surveys. The spatial distribution of aggregate abundance is analyzed as a function of the physical properties of the sea ice habitat. In addition, patchiness of the distribution as well as geometric properties of under-ice aggregates is investigated. Finally, different approaches for estimation of aggregate biomass are discussed to evaluate uncertainties and recommend procedures for future work.

Materials and methods

Remotely operated vehicle (ROV) observations

Sea ice algal aggregate observations were carried out during the IceArc cruise (ARK-XXVII/3) of the German research icebreaker RV Polarstern to the Central Arctic in August and September 2012. Eight ice stations were selected along the retreating sea ice edge, as well as within the Central Arctic pack ice close to the geographic North Pole (Fig. 1). The ice floe of the first ice station was revisited at the end of the cruise, enabling repeated sampling of the same ice floe after its transition from summer melting to autumn freeze-up conditions.

We used a V8Sii-ROV (Ocean Modules, Åtvidaberg, Sweden), to investigate the algae distribution underneath the sea ice. It was launched through a hole in the ice and operated from a tent directly on the ice floe several hundred meters away from the ship to avoid disturbance from the ship's thrusters. At each ice station, the ROV achieved a diving time between 6 and 8 h. The setup and operation procedure was similar to the one used in Nicolaus and Katlein (2013) with minor modifications: A Micron Nav (Tritech, Aberdeen, UK) ultra-short baseline (USBL) positioning system provided precise ROV location in a floe fixed coordinate system, while the rear facing Ospray SD-camera (Tritech, Aberdeen, UK) was repositioned to provide upward-looking imagery.

Additional sensors complemented the observations with measurements of the physical properties of the under-ice habitat. Ice draft was calculated as difference between the ROV depth and its distance to the ice measured by the upward-looking DST micron echosounder (Tritech, Aberdeen, UK) altimeter. Spectral light transmittance (320–950 nm) was calculated from continuous synchronous measurements of downwelling irradiance using two RAMSES-ACC spectroradiometers (TriOS GmbH, Rastede, Germany). While one sensor was mounted on the ROV, a reference sensor was placed on a tripod on the ice close to the ROV launch hole. Data processing, calibration, and measurement uncertainties have been described previously (Nicolaus et al. 2010; Nicolaus and Katlein 2013; Katlein et al. 2014).

At station ICE-7, under-ice aggregates were sampled with the ROV using a custom-built sampling device, to evaluate the image analyses. Samples were analyzed for particulate organic carbon (POC) and species composition as described in Assmy et al. (2013).

Image classification

To quantify the spatial distribution of under-ice algal aggregates from the acquired ROV imagery, we applied a

Fig. 1 Map of the IceArc expedition cruise track and positions of ice stations where under-ice algal aggregates were observed with the ROV. The *size of the circles* represents relative aggregate abundance (see Table 3 for absolute values), while the fraction of the two aggregate types as determined from mean aggregate eccentricity is depicted by the pie charts. *White color* stands for the fraction of elongated aggregates, while *black* depicts the fraction of rounded aggregates. Mean sea ice concentration during the cruise period is shown in the background
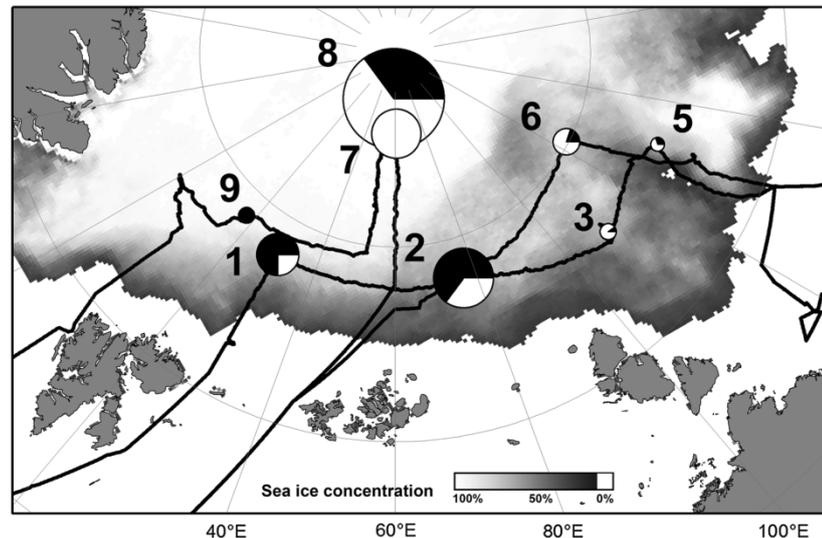
threshold algorithm implemented in MATLAB. We extracted still images (384 × 288 pixels) every 5 s from the videos of the upward-looking camera using the command line tool *ffmpeg*. Extracting the images every 5 s from the video overcomes problems with multiple detection of the same aggregates in consecutive images in most cases. To account for inconsistent lighting at the image edges, and to mask out the overlay data display, we cropped the image to obtain undisturbed RGB images of 250 × 200 pixels. Analysis of image histograms showed that aggregates could be detected well with a threshold value, by selecting all pixels with a value between 0 and 100 (out of maximal 255) in the green channel as aggregates. Thus, images were converted into binary images for further analyses.

All images taken at a depth >5 m and at ROV tilts >10° were automatically discarded. Images where ice structures or other objects were detected as aggregates and images where clearly identifiable aggregates were not detected by the algorithm were manually discarded. In the case where several close-lying aggregates were mistaken for a larger one, the image was excluded from shape and size analysis. In total, 11,000 images out of 23,800 images were used for further analysis. These images were on average taken at a distance of one meter from the ice underside and resulted in a spatial resolution of 4–5 mm.

Two-dimensional aggregate properties such as perimeter and area as well as minor axis and major axis of a fitted ellipse were calculated for each individual aggregate. For all aggregates covering more than 10 pixels of the image, shape parameters such as eccentricity, circularity, and the

equivalent circular diameter were derived. The measurements were transformed from pixel units to real units using the distance to the ice measured by the altimeter and a laboratory calibration of the camera. This image registration to true geometric units also enabled us to determine aggregate abundance per square meter as the number of aggregates in the image divided by the area surveyed by the image. Uncertainties in the distance to the ice, ROV-tilt and lens distortion result in <15 % uncertainty in aggregate size measurements.

The detection algorithm worked well in most situations, but due to its simple nature, detection was problematic in some cases, and 54 % of the images had to be excluded from the analysis. This was mostly related to inhomogeneous backlighting within the image at the transition between different ice features, where dark features in the ice were misinterpreted as aggregates. In addition, the differentiation of aggregates from small-scale ice structures and air bubbles can be ambiguous even to a trained observer verifying the detection. Finally, aggregates that are not dense enough or too small to leave a significant signature in the pixels green value remain undetected.

To account for multiple sampling due to overlapping ROV tracks in some areas (e.g., in the vicinity of the ROV launch hole), all obtained parameters were gridded on a regular grid with 3 × 3 m cell size, corresponding to the maximal uncertainty in the ROV position. All available images within a grid cell were selected, and the average of all measurements from these pictures was assigned to the grid cell.

Biomass estimation

To estimate aggregate biomass, the two-dimensional distribution deducted from the images was converted into three-dimensional volumetric information, including assumptions about the aggregate shape. While the assumption of a uniform algal layer thickness is more applicable to typical ice algal bottom layers in spring, we chose to represent the typically rounded aggregates by compact spheres. The diameter of the aggregate was determined as the equivalent circular diameter of the connected pixel region from the regions area.

We used different methods to obtain an estimate of the aggregate volume per area. Comparison between the different approaches enables us to evaluate the accuracy of our biomass estimates and the disadvantages of individual approaches. Names given in parentheses identify the different approaches later in the text.

For a first approach, aggregate volume was calculated for every detected aggregate. The single aggregate volumes were then added up and divided by the survey area ("aggregate list"). This approach does not take into account multiple sampling of some aggregates due to overlapping ROV tracks and should thus result in an overestimate of total biovolume.

In a second approach, the aggregate volume V was calculated using abundance a and diameter d values averaged over all images ("global mean"):

$$V = a \times \frac{4}{3}\pi\left(\frac{d}{2}\right)^3 \qquad (1)$$

As sphere volume is dependent on the third power of diameter (Eq. 1), this approach was repeated with a median diameter instead of average diameter, to avoid overestimation of biovolume for large, likely not spherical, aggregates ("global median").

To avoid influences from multiple sampling due to overlapping ROV tracks, the same calculation was repeated with average and median values obtained after gridding of the results ("gridded mean" and "gridded median"). The "gridded median" approach was also used in Assmy et al. (2013).

As larger rounded aggregates can occur in some parts of the survey areas, they can contribute significantly to biomass that gets lost when averaging over many grid cells. Thus, in a last approach, biovolume was calculated from abundance and diameter in each grid cell separately and averaged afterwards ("raster cells"). In the case where aggregates deviate substantially from a spherical shape, this approach can significantly overestimate biovolume.

To convert the estimated biovolume to carbon content, we used the measured carbon content of 390 mg C L^{-1} of two aggregates of known volume from ice station ICE-7 (Assmy et al. 2013).

Patchiness and size distribution

To analyze the spatial patchiness of the aggregate distribution, we used the index of mean crowding and Lloyds Index of Patchiness (Lloyd 1967; George 1981; Gutt et al. 1991) on the gridded data.

The size distribution of aggregating particles is often described using a power law

$$f(d) = cd^b \qquad (2)$$

with d the diameter, b the characteristic slope and a normalization constant c. The characteristic slope varies for different types of phytoplankton usually around a value of -3 (Alldredge and Gotschalk 1989; Guidi et al. 2009). Equation 2 was used to fit the aggregate size distributions obtained from the list of all detected aggregates and to determine the value of the characteristic slope. The characteristic slope and size distributions were interpreted in comparison with the marine particle aggregation model from Jackson (1990).

Results

Sea ice conditions

During the cruise, we observed a variety of sea ice conditions. While the first two stations located in the transpolar drift were comprised of dense first-year ice with a thickness of 1.0–1.5 m, the area of stations ICE-3 to ICE-6 was dominated by extremely rotten sea ice with a thickness of less than 1.0 m in an advanced melting stage. Later during the cruise, we observed freezing conditions, with ice covers of several centimeters forming on the melt ponds. Stations ICE-7 and ICE-8 in the central pack ice consisted of multiyear ice with a level ice thickness of up to 1.8 m. In contrast to the previous stations along the ice edge, the ice was less deteriorated by melt, and we observed the first snowfall in mid-September. The repeated visit to the first floe during ICE-9 was characterized by the fall freeze-up, with a snow cover of about 10 cm and refrozen ponds. In contrast, the topography of the ice underside had not changed dramatically. All observations were made in late summer at the end of the productive season. Thus, we can assume that algal biomass in general was low as compared to spring season, and in particular no ice algal layer was observed at the ice bottom.

ROV observations

ROV surveys underneath sea ice using upward-looking video imagery are a useful tool to quantify the abundance and spatial distribution of ice algal aggregates. The upward-looking imagery resulted in a continuous observation along

the dive tracks, covering a representative fraction of the variability in summer sea ice conditions in the investigated region. The large spatial coverage achieved during rather short station time is of great advantage in mapping the patchy under-ice ecosystem without bias towards sites with more abundant biomass. Detailed analysis of the upward-looking video imagery enabled us to quantify the amount and distribution of ice algal aggregates. Aggregate coverage for our investigated sites varied between 0.003 and 0.163 %, with an average of 0.04 %, while the abundance varied between 0.3 and 16.0 aggregates m^{-2}, with an average of 3.4 aggregates m^{-2} (Table 1). A comparison of our new and improved image processing analysis with previous studies using smaller data sets to estimate aggregate coverage and abundance is shown in Table 1. Subsequent analysis of several subsets of the entire dataset revealed that, due to the high spatial patchiness of the aggregates, the result was to some extent dependent on the area covered by the survey. While Assmy et al. (2013) analyzed only data from ice stations ICE-1 and ICE-2, Boetius et al. (2013) analyzed only one representative dive per ice station. As the image registration required manual post-processing, it was not available onboard the ship, and thus Boetius et al. (2013) reported only percent cover instead of aggregate abundance or biomass. When processing capabilities are limited, reasonably good estimates of percent cover can be achieved with the analysis of just one ROV transect if it is selected as representative from all available dives by the ROV pilot. Nevertheless, some transects differ significantly from the rest of the survey area.

Aggregates were observed both under first-year and under multi-year sea ice. Under-ice aggregates were found to be either free-floating, rounded masses dominantly formed by pennate diatoms (Fig. 2a), or elongated filamentous strings attached to or floating underneath the sea ice and composed of *M. arctica* (Fig. 2b). Details of the composition, development and fate of these aggregates have been described elsewhere (Assmy et al. 2013; Boetius et al. 2013; Fernández-Méndez et al. 2014).

Spatial distribution on floe scale

Maps of aggregate distributions were constructed from the results of the image analysis. A representative example can be found in Fig. 3 and all other stations in Online Resource 1. The aggregate distribution exhibited high variation, which is indicated by high values of Lloyd's index of patchiness, especially for stations with low aggregate abundance. The aggregate distribution is very patchy, and abundances vary from vast empty stretches to accumulations with peak detections of up to 200 aggregates m^{-2} on short distances of only tens of meters.

According to the visual impression from upward- and forward-looking ROV cameras, most of the aggregates were floating freely up against the underside of the sea ice. The buoyant status of the aggregates could be assessed after detachment from their original position by thruster disturbance. After disturbance, they again slowly rose up against the ice-water interface, indicating slightly positive buoyancy. Due to this positive buoyancy, most of them were situated in dome-like structures with a depth of just a few centimeters (Fig. 2d).

While one might expect a relation of the aggregate distribution to light availability under sea ice, due to better conditions for growth and floatation (Fernández-Méndez et al. 2014), no direct correlation of the spatial distribution of light transmittance and the aggregate distribution was found. As indicated by the visual observations, the only relation of aggregate abundance was found when comparing it to maps of ice thickness and roughness (Fig. 3 and

Table 1 Comparison of aggregate percent coverage and abundance retrieved from different image treatment approaches using varying subsets of the dataset

| Ice station	ICE-1	ICE-2	ICE-3	ICE-5	ICE-6	ICE-7	ICE-8	ICE-9
% Coverage								
Boetius et al. (2013) (one dive per station)	0.04	0.19	<0.001	0.04	0.03	0.55	0.13	–
Assmy et al. (2013) (all station dives)	0.01	0.03	–	–	–	–	–	–
This study (full dataset, improved processing)	0.026	0.062	0.005	0.003	0.008	0.163	0.093	0.004
Abundance (agg m^{-2})								
Boetius et al. (2013) (one dive per station)	–	–	–	–	–	–	–	–
Assmy et al. (2013) (all station dives)	0.79	5.06	–	–	–	–	–	–
	2.85	5.69	0.48	0.32	1.13	3.85	16.07	0.41
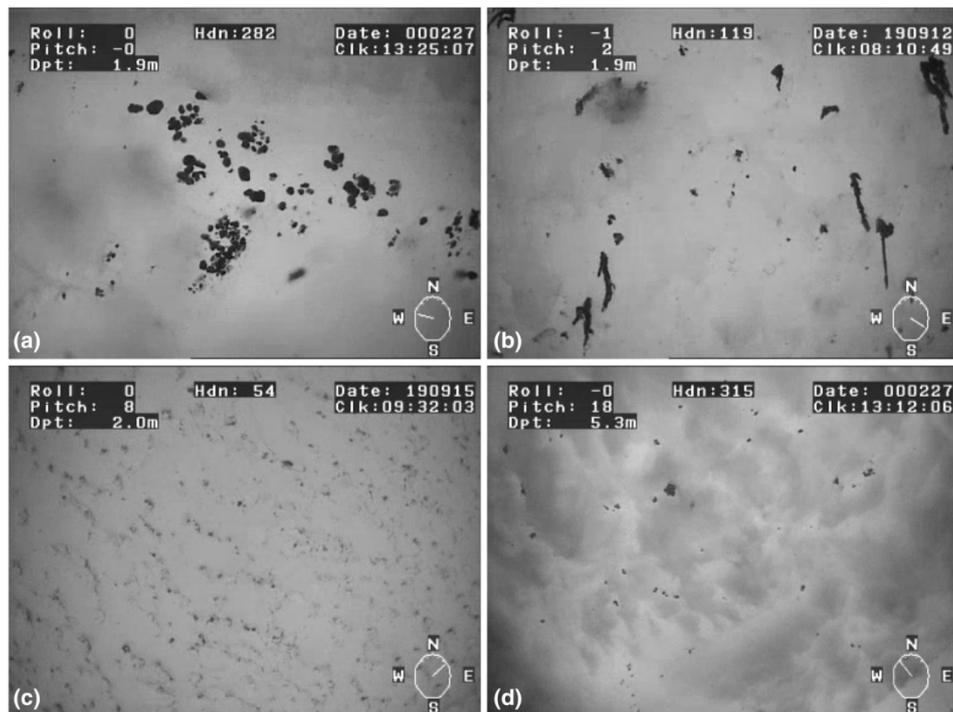
Fig. 2 Example images from the upward-looking ROV camera: **a** rounded aggregates formed by pennate diatoms, **b** filamentous aggregates of *M. arctica*, **c** a regular cover of small aggregates close to the detection limit of the method, **d** a tilted view from greater depth shows that aggregates are often trapped within dome-like or rough ice structures

Online Resource 1). High aggregate abundances often occurred at the boundaries of ridge keels and especially in level ice with moderate roughness (Fig. 4). Pressure ridges themselves did not host significant aggregate accumulations.

Biomass estimation

Results of the biomass estimates obtained by the different calculation approaches are shown in Table 2. While the different methods yielded a consistent picture of relative aggregate biomass at the different stations, they exhibited large quantitative differences. Biomass estimates spanned up to three orders of magnitude from <0.01 to 20.45 mg C m^{-2} even though they were derived with only slightly varying algorithms from the same dataset.

Aggregate properties

Mean properties of the detected aggregates are given together with the environmental parameters in Table 3. Mean aggregate diameters ranged from 2.1 to 4.1 cm, and

mean abundances ranged from 0.3 up to 16.0 aggregates per m^2. Mean aggregate eccentricities ranged from 0.76 to 0.88. The minima and maxima of observed eccentricities ($\varepsilon_{\min}$ and $\varepsilon_{\max}$) coincided with the visual observation of sole occurrence of rounded and filamentous aggregates. Thus, we deduced aggregate-type fractions ($f_{\text{spherical}}$ and f_{elong}) from a linear mapping to the eccentricity value ε with $f_{\text{spherical}} = \frac{\varepsilon - \varepsilon_{\min}}{\varepsilon_{\max} - \varepsilon_{\min}}$ and $f_{\text{elong}} = 1 - f_{\text{spherical}}$ (Fig. 1). While elongated filaments, corresponding to *M. arctica* aggregates, dominated the stations close to the Laptev Sea (ICE-3, ICE-5; ICE-6) and in the central pack ice (ICE-7, ICE-8), the stations further down the transpolar drift towards Fram Strait (ICE-1, ICE-2, ICE-9) that were dominated by rounded aggregates formed by pennate diatoms.

The size distribution of algal aggregates obtained from the image analysis for all stations generally followed the expected power law (Fig. 5). The characteristic slope obtained from power law fitting ranged from −1.3 to −3. It showed a correlation to the latitude of the ice station ($p = 0.014$). However, some important deviations between the different ice stations could be recognized. A distinct and unexpected feature was that
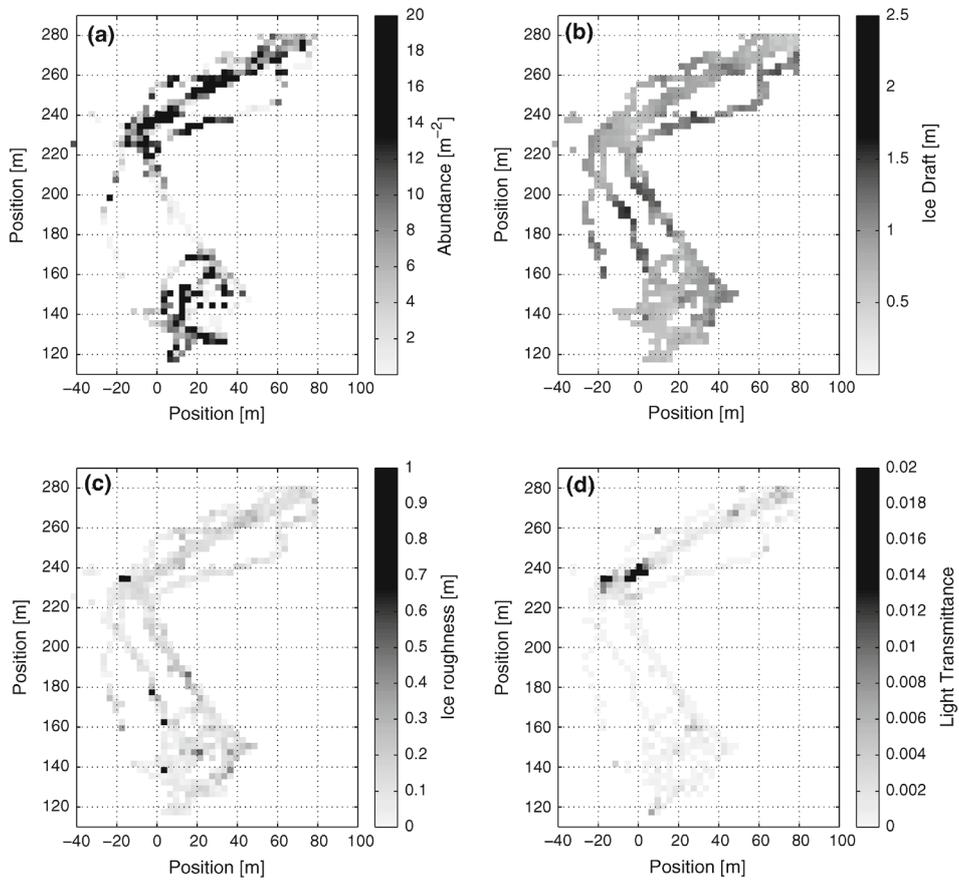
Fig. 3 Spatial distribution of aggregates (**a**), ice draft (**b**), ice roughness (**c**), and light transmittance (**d**) on station ICE-8. Distribution maps of the other stations can be found in the electronic supplement (Online Resource 1). Positions are given in a floe fixed coordinate system relative to the ship's GPS receiver

Fig. 4 Dependence of aggregate abundance on **a** sea ice draft and **b** sea ice roughness
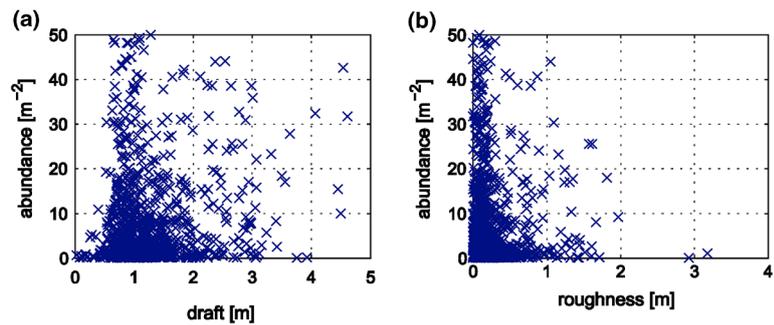
Table 2 Biomass estimates obtained by different approaches

Ice station	ICE-1	ICE-2	ICE-3	ICE-5	ICE-6	ICE-7	ICE-8	ICE-9	Mean
Aggregate volume (ml m^{-2})									
Global mean	0.4	2.1	0.02	0.03	0.04	10.4	1.1	0.03	1.8
Global median	0.2	0.5	<0.01	0.01	0.01	4.8	0.5	0.01	0.7
Gridded mean	2.5	6.0	0.7	0.3	0.4	16.8	6.5	0.3	4.2
Gridded median	0.9	1.4	0.5	0.1	0.2	21.9	4.1	0.3	3.7
Raster cells	5.2	16.3	4.7	1.6	3.0	38.6	6.9	1.7	9.7
Aggregate list	2.2	20.4	0.2	0.5	0.7	52.5	6.9	0.4	10.5
Carbon content (mg C m^{-2})									
Global mean	0.2	0.8	0.01	0.01	0.02	4.0	0.4	0.01	0.7
Global median	0.1	0.2	<0.01	<0.01	<0.01	1.9	0.2	<0.01	0.3
Gridded mean	1.0	2.3	0.3	0.1	0.1	6.5	2.5	0.1	1.6
Gridded median	0.4	0.5	0.2	0.03	0.07	8.5	1.6	0.1	1.4
Raster cells	2.0	6.4	1.8	0.6	1.2	15.0	2.7	0.7	3.8
Aggregate list	0.8	8.0	0.1	0.2	0.3	20.4	2.7	0.1	4.1

"Global" refers to averages over all images with valid information, while "gridded" refers to averages determined after spatial gridding of the results. "Mean" and "median" refer to whether mean or median diameters were used in the calculation. "Raster cells" refers to biomass calculation within the spatial grid cells before averaging over the survey area, while "aggregate list" refers to a calculation based on the list of all aggregate detections. The approaches "gridded median" and "raster cells" should provide the most reasonable estimates

the size distribution on ice stations 3, 5, 6, and 9 flattened out towards larger aggregates indicating enhanced buoyancy.

Discussion

Limitations of aggregate detection

Even though our analysis of upward-looking ROV images is currently the best available method for aggregate quantification on larger scales, one needs to keep in mind some limitations of the method. Firstly, the method is only able to detect macroscopic aggregates bigger than a few millimeters floating directly underneath the sea ice. This relatively high detection limit leads to an underestimation of the total algal aggregate biomass, but might be irrelevant in light of the huge range of biomass estimates caused by the different estimation algorithms. Secondly, close-lying aggregates that are detected as a single one, as well as aggregates with a strong deviation from the spherical shape, can lead to an overestimation of total aggregate volume. To reduce this effect, we excluded clumped aggregates from the analysis. This affects <5 % of the detected aggregates. Thirdly, aggregates are often located in transition zones between different ice types, which at the same time are often discarded during image processing, as the darker background of the thicker ice type gets classified as aggregates by the threshold algorithm. Overall, our method as used in this study might be rather underestimating ice algal aggregates. Future studies could thus

benefit from a more sophisticated image classification technique and machine learning for automation of the detection.

Patchiness and biomass estimates

The patchy spatial distribution of algal aggregates makes accurate, large-scale estimates of the aggregate biomass very challenging. As our results show, not only the choice and range of sampling sites, but also the method of estimating biomass from the data, may heavily impact the estimates. Consequently, small-scale surveys of the under-ice ecosystem such as diver observations are influenced by the choice of sampling sites. When comparing different surveys from ROVs and diver studies, differences of several orders of magnitude might simply arise due to differences in data processing and the size of the survey area. These differences can be even more dramatic when compared to results obtained by classical ice coring that do not usually capture algal aggregates. Larger-scale surveys tend to give a more realistic estimate (Assmy et al. 2013), accounting also for large areas empty of aggregates, which could be under-represented in spot measurements. Hence, values found in the literature should be used with caution for upscaling calculations. As estimates of aggregate biomass are highly dependent on the diameter of the aggregate, approaches that resolve spatial differences in aggregate properties ("raster cells") and account for multiple sampling ("gridded median") should give the most reliable results (Table 2). When considering only these two algorithms, which very likely are the most reliable ones,

Table 3 Environmental parameters at the ice stations and average aggregate properties

Ice station	Units	ICE-1	ICE-2	ICE-3	ICE-5	ICE-6	ICE-7	ICE-8	ICE-9
Polarstern station #		PS80/224	PS80/237	PS80/255	PS80/323	PS80/335	PS80/349	PS80/360	PS80/384
Latitude	°	84.00	83.95	82.86	82.88	85.06	87.93	88.83	84.35
Longitude	°	30.00	76.85	109.86	130.76	122.52	60.95	58.53	17.73
Date in 2012		10 Aug	15 Aug	20 Aug	5 Sep	8 Sep	19 Sep	22 Sep	29 Sep
Water depth	m	4,300	4,300	4,290	4,020	4,000	3,250	4,090	3,700
Sea ice concentration	%	80	80	70	60	50	100	100	100
Sea ice thickness	m	1.0	1.3	0.9	0.8	0.7	1.6	1.8	1.2
Sea ice type		FYI	FYI	FYI	FYI	FYI	MYI	MYI	FYI
Abundance	Agg. m^{-2}	2.8	5.6	0.4	0.3	1.1	3.8	16.0	0.4
Diameter (median)	cm	2.1	2.0	3.4	2.1	1.6	3.5	2.0	1.5
Diameter (mean)	cm	2.5	2.9	4.1	2.9	2.2	4.0	2.4	2.1
Circularity	–	0.79	0.77	0.66	0.70	0.68	0.64	0.71	0.84
Eccentricity	–	0.79	0.81	0.89	0.87	0.85	0.88	0.87	0.76
Index of Patchiness	–	11.5	9.2	67.4	17.9	74.0	3.1	3.3	5.2
Distance to ice edge	km	180	190	380	300	510	600	700	320
Distance to Laptev sea	km	1,450	910	580	490	740	1,210	1,210	1,560
Melt water[a]	m	0.5	0.7	0.7	2.3	2.2	0.8	0.9	–
Deep-sea algae cover[a]	%	0	0.003	1.3	0.5	0.8	2.2	10.4	–
slope of size distribution	–	−1.9	−2.2	−1.3	−1.7	−2.3	−2.2	−3.1	−1.6
Slope (Ø > 2 cm)	–	−3.0	−3.0	−0.6[b]	−1.2[b]	−2.0[b]	−3.2	−3.9	−1.0[b]

[a] Data from Boetius et al. (2013)

[b] $R^2 < 0.8$
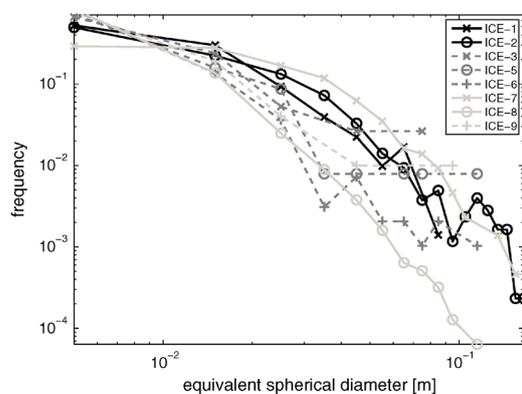
Fig. 5 Aggregate size distribution on the different ice stations. Size distributions that flatten out towards big aggregates are shown by *dashed lines*

the average aggregate biomass at our investigated sites and season accounts for 0.1–6 mg C m^{-2}.

Despite improvements in their quantification, algal aggregates will be difficult to include in ecosystem models, as low areal average biomass cannot describe their patchy distribution and thus their role as hotspots of biological activity (Assmy et al. 2013; Fernández-Méndez et al. 2014).

In comparison with our results, the study of Ambrose et al. (2005) shows a much higher percent coverage of 40–90 % of algae. This is due to the fact that the study was conducted much earlier in the season (June) on the shelf, and apart from aggregations also included the thin algal layer at the ice bottom in the analysis. Percent cover as presented in Ambrose et al. (2005) is a challenging proxy of total biomass due to the variable three-dimensional appearance of ice algae and aggregates. While in our dataset percent cover was only weakly correlated to aggregate abundance ($p = 0.16$), it was a better indicator of the total aggregate volume ($p = 0.001$–0.003 for the different algorithms). Aggregate abundance measured using ROV observations off Greenland in June/July varied between <1 and 50 aggregates m^{-2} (Gutt 1995) compares well to our study with an average abundance of <1 up to 16 aggregates m^{-2} with peak detections in a few images of maximal 200 aggregates m^{-2}. Recent diving investigations from an ice floe in the Fram Strait also revealed abundances of 6.3 ± 3.1 aggregates m^{-2} (Glud et al. 2014). While abundance values compare well, Glud et al. (2014) derived biomass estimates of up to 2.94 mg Chl a m^{-2}. This significantly exceeds our estimates of <0.01 to 0.19 mg Chl a m^{-2}. The large difference can be explained by the seasonal cycle of ice algal development, including seasonal variability in carbon to chlorophyll ratios, as well as differences in methodology.
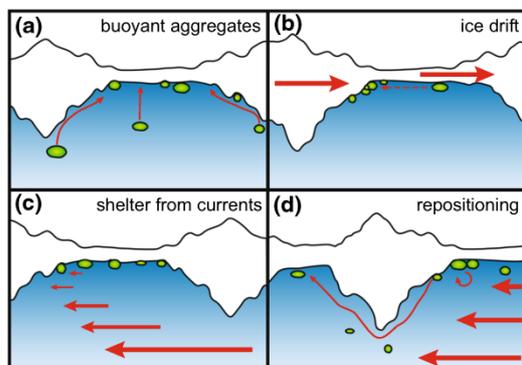
Fig. 6 Summary of the four main physical processes governing the spatial distribution of aggregates: **a** Buoyant aggregates are floating up against the ice and accumulate in level ice and dome-shaped structures; **b** during ice drift, pressure ridges skim through the water and can press the aggregates towards ridge edges; **c** location of the aggregates in the level ice and dome-shaped structures provides shelter from under-ice currents; **d** When these get stronger, aggregates get transported further by turbulent water motion

Spatial distribution

Our results show that the spatial distribution of under-ice algal-aggregate biomass is mostly dependent on the topography of the ice underside and the hydrodynamic regime. Ridge edges, dome-like structures, pockholes and small-scale roughness trap the loosely floating aggregates, leading to accumulations of aggregates in such topographic features. In contrast, pressure ridges themselves, did not host aggregate accumulations due to their large drafts, but rather acted as barriers hindering further aggregate movement. The aggregate distribution is likely very dynamic and can easily be affected by changing ice relative currents, such as strong winds or tides (Assmy et al. 2013; Glud et al. 2014). During such events, algal aggregates can get suspended in the mixed layer and drift along the ice until they get trapped again in the next ice feature. These main mechanisms of physical aggregate redistribution are summarized in Fig. 6. This solely physical mechanism differs strongly from the spatial distribution patterns of actively swimming zooplankton, which can use pressure ridges as a shelter (Gradinger et al. 2010). Also typical habitat properties determining organism distribution such as light availability did not explain the aggregate distribution, as the individual aggregate cannot position itself actively. Its position is determined passively by a complex hydrodynamic interaction between buoyancy, under-ice currents and turbulence, as well as the topography of the ice underside. Nevertheless, a wide range of habitat properties like the availability of light and nutrients as well as grazing of course influence the growth of sea ice algae, the formation of aggregates, and their fate related to sinking or suspension (Fernández-Méndez et al. 2014). While these factors impact the overall aggregate biomass, and might be responsible for the large biomass variation observed in this and other studies, the spatial distribution of aggregates on floe scale is determined by the topography of the ice underside.

This observed distribution pattern is typical of free-floating buoyant aggregates. While the rounded aggregates, formed by ice algae that aggregate after being flushed out of the brine channels due to summer-melt, are always free-floating, elongated aggregates formed by *M. arctica* have been observed both free-floating and attached to the ice. As we observed mostly free-floating aggregates, the spatial distribution of algal filaments attached to the ice could be different than described here. Nevertheless, we suppose that their spatial distribution is similar, as they also profit from current protection by pressure ridges. Even for attached aggregates, we would not expect a direct relation to the under-ice light field, as higher light penetration, e.g., through melt ponds can often be related to higher melt-water fluxes, and thus more difficult conditions for under-ice attachment.

Aggregate biomass as quantified by abundance or percent cover showed some positive correlation to geographical latitude ($p = 0.02$–0.03), indicating that aggregate biomass is greater within the Central Arctic basin than at the ice edge at the end of the summer. According to the shape analysis (Fig. 1), the fraction of filamentous aggregates of *Melosira arctica* seems to be decreasing with increasing distance from the Laptev Sea. This is consistent with previous observations. Ambrose et al. (2005) and Melnikov (1997) described *M. arctica* as occurring on the shelves of the Arctic, where its spores can get incorporated during ice formation in polynias and be transported into the central basin (Smetacek 1985). The fraction of rounded aggregates composed of pennate diatoms increases towards the ice edge. Syvertsen (1991) described a similar succession of pelagic and ice algal flocs in the Barents Sea, followed by filaments of *M. arctica* towards the central pack ice.

Implications for carbon export

It was possible to resample the ice floe of ice station ICE-1 (10 August) almost 2 months later on 29 September at the end of the productive season, when light availability was strongly reduced. Assuming that the ice floe was in both cases representative for the area and that thus displacement of aggregates by advection can be neglected, we can deduce some information about the changes in the aggregate distribution during that time period. Along with the decrease in aggregate abundance from 2.8 to

0.4 aggregates m^{-2} and the decrease in median diameter from 2.1 to 1.5 cm, we estimate that 67–94 % of the biomass present during the first sampling disappeared by the end of September. Observations of fresh aggregates on the sea floor indicate that they sank to the deep sea (Boetius et al. 2013), but consumption by zooplankton could have played a role as well (Assmy et al. 2013). The aggregate size distributions of both samplings reveal significant differences in the buoyancy status of the aggregate population. While the size distribution in August resembles a more typical distribution of aggregates prone to sinking (McCave 1984), the size distribution at the end of September levels out towards larger aggregates. This flattening of the size distribution towards larger sizes could be reproduced by deactivating the sinking term in the aggregate formation model from Jackson (1990). It thus indicates that aggregates that are still present in September are buoyant and have so far avoided sinking, while the non-buoyant portion of the aggregate population sank down between the first and second samplings. Analyzing the size distributions, we found a signature of buoyant aggregates mainly in the stations closest to the Laptev Sea shelf edge. In this area, we observed extremely rotten and melting sea ice with favorable conditions for aggregate floatation due to sufficient light available for oxygen production (Glud et al. 2014; Fernández-Méndez et al. 2014).

The theory of particle aggregation also yields critical POC concentrations above which phytoplankton exhibits a high aggregation potential (Jackson 1990). Water column concentrations of 70–100 µg L^{-1} POC from our field sites (Fernández-Méndez et al. 2014) thus imply that with typical under-ice shear rates between 0.001 and 1 s^{-1} (McPhee and Morison 2001), the sticking efficiency must be very high. Accordingly the Kolmogorov length scale of turbulence, describing the length scale at which aggregates are prone to breakup processes, is only 0.2–3 cm. The aggregates must thus be bonded together strongly, avoiding aggregate breakup. This matches previous stickiness estimates (Riebesell 1991; Hansen and Kiorboe 1997) and our observations that the aggregates even withstand thruster wash from the ROV.

The ice algal aggregates described in this study are of extraordinary size, when compared to size-ranges observed in flocculation studies in other seas (Riebesell et al. 1991; Alldredge and Gotschalk 1989). When applying relationships between diameter and sinking speed from the literature (Jackson 1990), aggregates with a diameter of 3 cm will reach the deep-sea floor surprisingly fast within a single day once they lose buoyancy at the surface, potentially due to insufficient light conditions or high respiration rates within the aggregates (Fernández-Méndez et al. 2014). This is consistent with observations of fresh ice algal aggregates in water depths around 4,000 m from Boetius et al. (2013).

We conclude that the spatial distribution of under-ice algal aggregates is mainly governed by the topography of the ice underside. Aggregates float up against any dome-shaped structures, and ridge edges inhibit further movement. Thus, sea ice ridges play an important role in structuring the spatial distribution of ice algal aggregates. On the large scale, filamentous aggregates of *M. arctica* are the dominant aggregate type in the inner part of the Central Arctic pack ice, while closer to the ice edge under melting sea ice, rounded aggregates mainly formed by pennate diatoms dominate. The size distribution of aggregates indicates that at least a portion of them do stay afloat and can get incorporated into the ice during freeze-up. Even though our ROV-based method has proved suitable for providing the first large-scale quantitative estimate of aggregate biomass, it remains difficult to compare biomass estimates to other studies, due to the high patchiness, and uncertainties in both samplings and in particular in different ways of deriving areal average estimates from the observations.

References

Alldredge AL, Gotschalk CC (1989) Direct observations of the mass flocculation of diatom blooms: characteristics, settling velocities and formation of diatom aggregates. Deep Sea Res Part A Oceanogr Res Pap 36(2):159–171. doi:10.1016/0198-0149(89)90131-3

Ambrose WG, von Quillfeldt C, Clough LM, Tilney PVR, Tucker T (2005) The sub-ice algal community in the Chukchi sea: large- and small-scale patterns of abundance based on images from a remotely operated vehicle. Polar Biol 28(10):784–795. doi:10.1007/s00300-005-0002-8

Arrigo KR (2014) Sea ice ecosystems. Ann Rev Mar Sci 6(1):439–467. doi:10.1146/annurev-marine-010213-135103

Arrigo KR, van Dijken G, Pabi S (2008) Impact of a shrinking Arctic ice cover on marine primary production. Geophys Res Lett 35(19):L19603. doi:10.1029/2008gl035028

Assmy P, Ehn JK, Fernández-Méndez M, Hop H, Katlein C, Sundfjord A, Bluhm K, Daase M, Engel A, Fransson A, Granskog MA, Hudson SR, Kristiansen S, Nicolaus M, Peeken I,

Renner AHH, Spreen G, Tatarek A, Wiktor J (2013) Floating ice-algal aggregates below melting Arctic sea ice. PLoS One 8(10):e76599. doi:10.1371/journal.pone.0076599

Boetius A, Albrecht S, Bakker K, Bienhold C, Felden J, Fernandez-Mendez M, Hendricks S, Katlein C, Lalande C, Krumpen T, Nicolaus M, Peeken I, Rabe B, Rogacheva A, Rybakova E, Somavilla R, Wenzhoefer F (2013) Export of algal biomass from the melting Arctic sea ice. Science 339(6126):1430–1432. doi:10.1126/science.1231346

Fernández-Méndez M, Wenzhöfer F, Peeken I, Sørensen HL, Glud RN, Boetius A (2014) Composition, buoyancy regulation and fate of ice algal aggregates in the central Arctic Ocean. PLoS One 9(9):e107452. doi:10.1371/journal.pone.0107452

George D (1981) Zooplankton patchiness. Rep Freshw Biol Assoc 49:32–44

Glud R, Rysgaard S, Turner G, McGinnis D, Leaky R (2014) Biological and physical induced oxygen dynamics in melting sea ice of the Fram Strait. Limnol Oceanogr 59(4):1097–1111. doi:10.4319/lo.2014.59.4.1097

Gosselin M, Levasseur M, Wheeler PA, Horner RA, Booth BC (1997) New measurements of phytoplankton and ice algal production in the Arctic Ocean. Deep Sea Res Part II 44(8):1623–1644. doi:10.1016/S0967-0645(97)00054-4

Gradinger R, Bluhm B (2010) Assessment of the abundance and diversity of sea ice biota. In: Eicken H, Salganek M (eds) Field techniques for sea-ice research. University of Alaska Press, Fairbanks, p 294

Gradinger R, Bluhm B, Iken K (2010) Arctic sea-ice ridges—safe heavens for sea-ice fauna during periods of extreme ice melt? Deep Sea Res Part II Top Stud Oceanogr 57(1–2):86–95. doi:10.1016/j.dsr2.2009.08.008

Guidi L, Stemmann L, Jackson GA, Ibanez F, Claustre H, Legendre L, Picheral M, Gorsky G (2009) Effects of phytoplankton community on production, size and export of large aggregates: a world-ocean analysis. Limnol Oceanogr 54(6):1951–1963. doi:10.4319/lo.2009.54.6.1951

Gutt J (1995) the occurrence of sub-ice algal aggregations off Northeast Greenland. Polar Biol 15(4):247–252

Gutt J, Gorny M, Arntz W (1991) Spatial distribution of Antarctic Shirmps (Crustacea, Decapoda) by underwater photography. Antarct Sci 3(4):363–369

Haas C, Pfaffling A, Hendricks S, Rabenstein L, Etienne J-L, Rigor I (2008) Reduced ice thickness in Arctic Transpolar Drift favors rapid ice retreat. Geophys Res Lett 35(17):L17501. doi:10.1029/2008gl034457

Hansen JLS, Kiorboe T (1997) Quantifying interspecific coagulation efficiency of phytoplankton. Mar Ecol Prog Ser 159:75–79

Horner R, Ackley SF, Dieckmann GS, Gulliksen B, Hoshiai T, Legendre L, Melnikov IA, Reeburgh WS, Spindler M, Sullivan CW (1992) Ecology of Sea Ice Biota. 1. Habitat, terminology, and methodology. Polar Biol 12(3–4):417–427

Jackson GA (1990) A model of the formation of marine algal flocs by physical coagulation processes. Deep Sea Res Part A Oceanogr Res Pap 37(8):1197–1211. doi:10.1016/0198-0149(90)90038-w

Katlein C, Nicolaus M, Petrich C (2014) The anisotropic scattering coefficient of sea ice. J Geophys Res Oceans. doi:10.1002/2013JC009502

Krembs C, Tuschling K, von Juterzenka K (2002) The topography of the ice-water interface - its influence on the colonization of sea ice by algae. Polar Biol 25(2):106–117. doi:10.1007/s003000100318

Krembs C, Eicken H, Deming JW (2011) Exopolymer alteration of physical properties of sea ice and implications for ice habitability and biogeochemistry in a warmer Arctic. Proc Natl Acad Sci USA 108(9):3653–3658. doi:10.1073/pnas.1100701108

Kwok R, Rothrock DA (2009) Decline in Arctic sea ice thickness from submarine and ICESat records: 1958–2008. Geophys Res Lett. doi:10.1029/2009gl039035

Lee SH, McRoy CP, Joo HM, Gradinger R, Cui XH, Yun MS, Chung KH, Kang SH, Kang CK, Choy EJ, Son SH, Carmack E, Whitledge TE (2011) Holes in progressively thinning Arctic sea ice lead to new ice algae habitat. Oceanography 24(3):302–308

Legendre L, Ackley SF, Dieckmann GS, Gulliksen B, Horner R, Hoshiai T, Melnikov IA, Reeburgh WS, Spindler M, Sullivan CW (1992) Ecology of sea ice biota. 2. Global significance. Polar Biol 12(3–4):429–444

Leu E, Wiktor J, Soreide JE, Berge J, Falk-Petersen S (2010) Increased irradiance reduces food quality of sea ice algae. Mar Ecol Prog Ser 411:49–60. doi:10.3354/meps08647

Leu E, Soreide JE, Hessen DO, Falk-Petersen S, Berge J (2011) Consequences of changing sea-ice cover for primary and secondary producers in the European Arctic shelf seas: timing, quantity, and quality. Prog Oceanogr 90(1–4):18–32. doi:10.1016/j.pocean.2011.02.004

Lloyd M (1967) Mean Crowding. J Anim Ecol 36(1):1–30. doi:10.2307/3012

Markus T, Stroeve JC, Miller J (2009) Recent changes in Arctic sea ice melt onset, freezeup, and melt season length. J Geophys Res Oceans 114. doi:10.1029/2009jc005436

Maslanik JA, Fowler C, Stroeve J, Drobot S, Zwally J, Yi D, Emery W (2007) A younger, thinner Arctic ice cover: increased potential for rapid, extensive sea-ice loss. Geophys Res Lett 34(24):L24501. doi:10.1029/2007gl032043

McCave IN (1984) Size spectra and aggregation of suspended particles in the deep ocean. Deep Sea Res Part A Oceanogr Res Pap 31(4):329–352. doi:10.1016/0198-0149(84)90088-8

McPhee MG, Morison JH (2001) Under-ice boundary layer. In: Steele JH (ed) Encyclopedia of ocean sciences. Academic Press, Oxford, pp 3071–3078

Melnikov I (1997) The Arctic sea ice ecosystem. Cambridge University Press, Cambridge

Melnikov IA, Bondarchuk LL (1987) To the ecology of the mass aggregations of colonial diatom algae under the Arctic drifting sea ice. Okeanologiya 27(2):317–321

Mundy CJ, Barber DG, Michel C (2005) Variability of snow and ice thermal, physical and optical properties pertinent to sea ice algae biomass during spring. J Mar Syst 58(3–4):107–120. doi:10.1016/j.jmarsys.2005.07.003

Nansen F (1906) Protozoa on the ice-floes of the North Polar sea. The Norw. North Polar Exp. 1893–96. Scientific results ed by F Nansen Kristiania (Jacob Dybwad) vol 5 (No. XVI):22

Nicolaus M, Katlein C (2013) Mapping radiation transfer through sea ice using a remotely operated vehicle (ROV). The Cryosphere 7(3):763–777. doi:10.5194/tc-7-763-2013

Nicolaus M, Hudson SR, Gerland S, Munderloh K (2010) A modern concept for autonomous and continuous measurements of spectral albedo and transmittance of sea ice. Cold Reg Sci Technol 62(1):14–28. doi:10.1016/j.coldregions.2010.03.001

Nicolaus M, Katlein C, Maslanik J, Hendricks S (2012) Changes in Arctic sea ice result in increasing light transmittance and absorption. Geophys Res Lett 39:L24501. doi:10.1029/2012gl053738

Perovich DK, Roesler CS, Pegau WS (1998) Variability in Arctic sea ice optical properties. J Geophys Res Oceans 103(C1):1193–1208. doi:10.1029/97jc01614

Poulin M, Underwood GJC, Michel C (2014) Sub-ice colonial Melosira arctica in Arctic first-year ice. Diatom Res 29(2):213–221. doi:10.1080/0269249X.2013.877085

Quillfeldt CV, Hegseth EN, Sakshaug E, Johnsen G, Syvertsen EE (2009) Ice algae. In: Sakshaug E, Johnsen G, Kovacs KM (eds) Ecosystem Barents Sea. Tapir Aacademic Press, Trondheim, pp 285–302

Riebesell U (1991) Particle aggregation during a diatom bloom: 1. Physical aspects. Mar Ecol Prog Ser 69(3):273–280. doi:10.3354/meps069273

Riebesell U, Schloss I, Smetacek V (1991) Aggregation of algae released from melting sea ice—implications for seeding and sedimentation. Polar Biol 11(4):239–248

Roesel A, Kaleschke L (2012) Exceptional melt pond occurrence in the years 2007 and 2011 on the Arctic sea ice revealed from MODIS satellite data. J Geophys Res 117(C5):C05018. doi:10.1029/2011jc007869

Serreze MC, Holland MM, Stroeve J (2007) Perspectives on the Arctic's shrinking sea-ice cover. Science 315(5818):1533–1536. doi:10.1126/science.1139426

Smetacek VS (1985) Role of sinking in diatom life-history cycles: ecological, evolutionary and geological significance. Mar Biol 84(3):239–251. doi:10.1007/BF00392493

Syvertsen EE (1991) Ice algae in the Barents Sea: types of assemblages, origin, fate and role in the ice-edge phytoplankton bloom. Polar Res 10(1):277–288. doi:10.1111/j.1751-8369.1991.tb00653.x

Wassmann P, Reigstad M (2011) Future Arctic Ocean seasonal ice zones and implications for pelagic–benthic coupling. Oceanography 24(3):220–231

Werner I, Lindemann F (1997) Video observations of the underside of Arctic sea ice-features and morphology on medium and small scales. Polar Res 16:27–36. doi:10.1111/j.1751-8369.1997.tb00725.x

7. Discussion

7.1. Spatial variability of sea ice light transmittance

This thesis provides new insights into the aspects of the spatial variability of light transmission through sea ice. A main point is to show the applicability of under-ice ROV operations for the investigation of the under-ice light field and its spatial variability. Using recent underwater technology, this possibility was investigated and its use presented successfully in the scientific community. Combining upward looking multi-beam-sonar ice-bottom topography surveys with aerial photography and drill hole measurements, the length scales of spatial variability of different physical sea ice properties were investigated on different scales. While on the small scale of around 100m, the variability length scale of light transmittance was driven by the length scale of surface albedo variation - in particular melt ponds, the variability length scale of light transmittance was similar to the length scale of ice thickness variations on the km scale. This result provides an important link between small scale studies conducted by divers or observation class ROVs and large scale satellite or circulation model datasets indicating the different drivers of light variability on the different scales. To enable further understanding of light transmission over various scales, a method to derive light transmission from ice thickness and albedo distributions – both quantities that can be observed from the surface or even satellite -was proposed on the basis of the observations.

This thesis has identified variations in the surface properties of sea ice – in particular the presence of melt ponds – and variations in the ice thickness as the main drivers of the variability of light transmission through Arctic sea ice in summer. While this has been known already from previous investigations based on point measurements in the last decades [*Light et al.*, 2008; *Perovich*, 1990; 2005; *Perovich et al.*, 2011], the new datasets acquired with ROVs offer the unique possibility to investigate the spatial structure of the variability. Different typical length scales in the variability of surface properties and ice thickness identified the role of the different drivers on different scales, with albedo variations caused by melt ponds governing the light transmission variability on scales of 100m and ice thickness variations driving the light variability on larger scales.

All studies were conducted during the melting season, when no significant snow cover is present on the Arctic sea ice. In other seasons, such as winter and spring, variations in snow cover are the most important factor driving under-ice light variability [*Nicolaus et al.*, 2013a], as snow is a very efficient scattering medium,

causing ten times stronger light extinction than bare sea ice [*Grenfell*, 1977]. While undulations in a thick snow layer have only a minor effect on the absolute under-ice light field in winter due to the generally low transmittance, they might nevertheless be linked to the summer variability, as snow dune formation has been identified as one of the drivers regulating the size and position of melt ponding during spring [*Petrich et al.*, 2012b]. A contrary view considers the length scale of melt ponds as a function of melt progression inherent to the medium sea ice [*Hohenegger et al.*, 2012]. Both processes could be interesting options for realizing subgrid scale parameterizations of the spatial variability of light transmission through Arctic summer sea ice in sea-ice models or even general circulation models. Another option would be the use of the formalism for estimating light transmission histograms from distributions of ice thickness and surface albedo as presented in this thesis. The formalism can be easily generalized to accustom further variables, such as the snow thickness distribution to make it applicable to all seasons. As light extinction depends nonlinearly from ice and snow thickness it is important to work with distribution functions instead of point values to avoid underestimation of light transmission.

7.2. Radiative Transfer in an ice covered ocean

Optical measurements underneath sea ice are tricky in interpretation, as the inhomogeneous sea ice layer introduces various geometric effects due to varying sensor footprints. These effects were investigated and quantified on the basis of a newly developed model of geometrical radiometry under inhomogeneous surfaces. It was shown that the lateral extent of deviations in the data caused by geometric effects is on the length scale of the sensor depth for irradiance measurements. Furthermore it could be shown that the retrieval of inherent optical properties of sea water from vertical profiles of optical measurements as widely used in the literature [*Bélanger et al.*, 2013; *Ehn et al.*, 2011; *Nicolaus and Katlein*, 2012] can only provide limited information and thus care must be taken in the interpretation and processing of such measurements underneath a spatially inhomogeneous ice cover.

On the microscopic scale, we investigated the geometric properties of light scattering in sea ice. By an analysis of field data in combination with laboratory experiments, as well as Monte-Carlo modeling, it could be shown that the strength of scattering in sea ice is dependent on the direction of photon travel. This anisotropy is caused by the mostly lamellar microstructure of sea ice where scattering planes are predominantly aligned vertically, reducing horizontal light propagation. This finding contributed to a better understanding of the under-ice radiance distribution also facilitating the interpretation of under-ice light measurements. The anisotropic scattering in the ice affects the geometry of the

under-ice light field, leading to stronger contrasts on short distances between sea ice patches with different optical properties. A main finding is an approach to convert measurements of under-ice zenith radiance into irradiance enabling a higher spatial resolution in the investigation of the spatial variability of the under-ice light field as well as the conversion of older data acquired with radiance sensors [*Roulet et al.*, 1974].

A closer investigation confirmed that both, the anisotropic scattering within the ice as well as the geometric variations in sea ice optical properties, cause a complicated light-field geometry underneath sea ice. This has been indicated before by a few measurements of vertical light profiles below bare ice next to melt ponds, where the adjacent ponds lead to an increase of irradiance from the surface to an irradiance maximum at some meters depth, followed by a decline in irradiance [*Frey et al.*, 2011]. This for example limits the possibility to retrieve inherent optical properties of the sea water from vertical profiles and questions the usefulness and correct way of correcting measurements taken at a distance to the ice for the water layer in between sensor and ice. Unfortunately these effects of ice and measurement geometry are usually not considered in the interpretation of under-ice light measurements, even though neglecting these effects can seriously hinder data interpretation by covering the effects of the processes under investigation [e.g. in *Ehn et al.*, 2011].

Apart from the challenges arising during data interpretation, the complex under-ice light field also complicates the exact location of solar energy deposition in the upper water column. Geometric effects, as well as the varying radiance distribution due to anisotropic scattering in the ice, might lead to a bigger deposition of solar energy in deeper water layers as compared to the case with a homogeneous ice layer. This vertical location of energy deposition in the water column crucially influences the oceanographic and biogeochemical processes in the upper water layers and thus the fate of the Arctic climate system [*Park et al.*, 2015].

Most under-ice light measurements have been performed using planar irradiance sensors [*Nicolaus et al.*, 2010a; *Nicolaus et al.*, 2010b]. This is motivated by the fact, that those sensors measure the energy flux per area on a horizontal plane and thus gives crucial information about the energy fluxes in the climate system. The results of this thesis show that these sensors are though not perfectly suited for the investigation of spatial variability of ice optical properties, due to their large effective footprint reducing the lateral resolution of the measurements. Strong contrasts on short distances can better be reproduced by radiance sensors with a very narrow field of view that does not smoothen out the contrasts at the ice underside resulting in a better spatial resolution. Thus

radiance sensors should be used in conjunction with irradiance sensors, whenever the spatial structure of the light field is of interest. This holds true especially when sensors are operated at a greater distance to the ice, such as on submarines or AUVs [*Kukulya et al.*, 2010].

7.3. Relative importance of sea ice shortwave radiative transfer for the energy balance of sea ice

Shortwave radiative transfer is a crucial component of the Arctic climate system, as the partitioning of sunlight strongly impacts the energy budget of sea ice. The ice-albedo feedback - where melting ice leaves behind dark water that absorbs more energy and thus leads to more melting – is well studied to be a main driver of Arctic change. Due to the sensitivity of models to this parameter ice albedo is often used as a tuning knob for adjusting model output. Nevertheless sea ice optics is often poorly represented in current global circulation models or even specialized sea ice models.

This negligent treatment is thus well based on the early optical observations on sea-ice. As sea ice used to be thicker, older and more extensive in the past, less solar energy was transmitted so that other components, such as the ocean heat flux and turbulent fluxes were dominating the surface energy budget during all seasons. With the ongoing change of sea ice properties in the last decades, the partitioning of solar energy has gained relative importance especially during summer and the shoulder seasons. Recent observations show, that the shortwave energy flux is now frequently comparable to or even outcompetes the ocean heat flux during the melting season even in areas which are driven by the ocean heat flux throughout large parts of the year [*Flocco et al.*, 2012; *Hudson et al.*, 2013]. Several comparisons of different radiative transfer schemes in large scale models [e.g. *Holland et al.*, 2011; *Park et al.*, 2015] have pointed out the sensitivity of model results to the accuracy of the representation of shortwave radiative fluxes. This is also of particular interest for the challenge of ice forecasting for the opening maritime transport routes along the coasts of the Arctic, as the sea ice mass balance in the relevant forecast areas with retreating thinner ice is highly impacted by shortwave radiative fluxes. As shortwave energy transfer gets more important with thinner sea ice, measurement efforts need to focus more on the growth and decay of thin ice as well as on light transmission during the shoulder seasons. Higher light transmission through the pack ice is thus both a cause and a result of the ongoing rapid changes in the Arctic climate system.

The strong link between sea ice melt – in particular September minimum extent – and solar energy partitioning has been shown in several studies. *Schröder et al.*

[2014] showed, that a preconditioning of the sea ice cover with melt ponds is highly correlated to the minimum sea ice extent in September and *Cox et al.* [2015] were able to demonstrate a spatial correlation between incoming solar energy at several observation stations around the Arctic and September sea ice concentration. While the optical properties of sea ice are an efficient tuning parameter in models, these results show that this needs to be done with much care and changes in the optical properties of sea ice and also their spatial variability need to be accurately represented in models that are aiming for reliable results in the summer Arctic.

Radiative transfer models of sea ice are well developed up to a high degree of complexity. Most of them have in common that apparent optical properties of sea ice like albedo and transmittance are calculated from inherent optical properties of sea ice. While simple exponential decay models rely on only a few extinction coefficients [*Arrigo et al.*, 1991; *Grenfell*, 1977], more complex models like two stream models [*Perovich*, 1996], discrete-ordinate models [*Hamre et al.*, 2004], Monte-Carlo ray tracing models [*Light et al.*, 2003b; *Petrich et al.*, 2012a] or the Delta-Eddington scheme [*Holland et al.*, 2011] use an increasing number of coefficients representing the various micro-optical properties. Unfortunately these parameters are dependent on the model geometry and very little is known about their accurate variability both in space within a model grid cell as well as in time throughout the melt cycle, when the physical properties of sea ice change dramatically. Thus a higher degree of complexity in the optical models does not necessarily result in more accurate results. In summary, it can be said that the tools of radiative transfer modeling are well developed, but both, the choice of proper input parameters as well as the representation of spatial variability, needs significant improvements, e.g. by explicit melt pond parameterizations [*Flocco et al.*, 2010; *Flocco et al.*, 2012; *Hohenegger et al.*, 2012].

Another important aspect of the deposition of solar shortwave energy through sea ice is the vertical location, where the transmitted energy gets absorbed. A recent study by *Park et al.* [2015] shows that a variation of the depth where solar energy gets deposited in the water column significantly changes the model response to changes in the Arctic climate forcing. The location of light absorption determines whether the warmed water layer will interact with the ice cover or stay isolated, depending on local stratification and mixing. A key factor determining light penetration to greater depth is of course the turbidity caused by algal blooms in the water column underneath the ice. These blooms have only been discovered recently and have not yet been investigated more closely [*Arrigo et al.*, 2012; *Lowry et al.*, 2014], so that they have not yet been implemented in large scale models. Stronger algal blooms are fueled by higher

light levels underneath the ice, but in turn also absorb more solar energy [*Zeebe et al.*, 1996] heating the uppermost water layers, which could lead to further basal sea ice melting. On the other hand the spatial variability of the optical sea ice properties and a strongly anisotropic radiance distribution lead to a deeper penetration of light into the water column than commonly applied in sea ice models.

Altogether it can be concluded that a good understanding of ice optical properties in combination with a better understanding of under-ice mixing will improve the ability to correctly predict sea ice melt at its verge to vanishing, especially when the spatial variability is taken into account.

7.4. Impact on the sea ice ecosystem

The acquired knowledge about adequately representing the spatial variability of light transmission through sea ice and its scattering properties in simple models was used for the development of the Central Arctic Ocean Primary Productivity model (CAOPP), which calculates daily net primary production using remote sensing datasets, laboratory measured photosynthesis irradiance curves, and a specially adapted in and under-ice light parameterization. This model was then also used to calculate potential Arctic primary productivity for a future scenario, under the assumption of unchanged nutrient conditions. It is one of the first primary production models strictly focusing on the ice covered Central Arctic based on measurements and remote sensing data. As the model's parameters are based on one of the biggest primary production datasets yet available from the Central Arctic, this makes comparison of the results to other studies difficult. Nevertheless, the model was compared to other Arctic primary productivity products in the Primary Productivity Algorithm Round Robins (PPARR 5). Unfortunately this effort mostly compared data points outside of the confidence zone of the CAOPP model. Nevertheless, model performance proved to be competitive even in these areas.

As ROV observations under sea ice offer great opportunities for interdisciplinary research, the acquired data was used to investigate the influence of varying light transmission on the spatial distribution of under-ice algal aggregates. For that purpose, an algorithm for supervised automatic detection and quantification of ice algal aggregates on images from the upward looking ROV camera was developed. The data were interpreted in conjunction with light-transmission as well as ice bottom topography, water temperature, salinity and oxygen concentration. It could be shown that the spatial distribution of algal aggregates on floe scale is driven by a hydrodynamic interaction between ice bottom topography and the buoyancy inherent to the aggregates, with aggregates

concentrating in dome shaped structures, where they are protected from strong currents. Typical habitat properties that are known to be important for the development of organisms, such as available light or salinity did not seem to influence the spatial distribution of aggregates on the floe scale, whereas they certainly play an important role in the development and fate of sea-ice algae on larger scales.

Spatial variability of light conditions within the sea-ice can explain some part of the high patchiness of ice algal abundance [*Krembs et al.*, 2002] but also affects life in the water column beneath. As sea ice is drifting, the spatial variability is translated into a temporal variation or intermittency of the under-ice light field available to phytoplankton thriving in the water column beneath sea ice. While these effects of fluctuating light have hardly been studied for Arctic phytoplankton, there is evidence that intermittent light with variation periods much shorter than a diurnal cycle can have significant impact on community structure [*Flöder et al.*, 2002; *Grobbelaar et al.*, 1996; *Litchman*, 2000]. Algal photosystems adapt differently to intermittent light, potentially enabling them to avoid damage to their photosystems and make better use of the high light intensities during short duration.

7.5. Uncertainties

The presented datasets increased our understanding of uncertainties associated with radiometric measurements underneath sea ice. The investigation of the angular radiance distribution as well as the theoretical framework to assess effects of measurement geometry revealed common misconceptions widely found in the literature. For example we could show that the commonly used assumption of an isotropic light field underneath sea ice leads to errors as big as 50%. The thesis furthermore shows that irradiance measurements taken at depth cannot be corrected to accurately represent fluxes at the ice underside, if the ice geometry is neglected. This also applies to the determination of inherent optical properties of sea water underneath an inhomogeneous sea ice cover.

As the datasets contain a high number of spatially distributed measurements, distribution functions can be analyzed instead of point values. This provides a much better view of the representativeness of a single point measurement. Absolute calibration of the used sensors is conducted by the manufacturer following a NIST-traceable calibration procedure and additional sensor inter-comparison in the field. As this thesis is mostly concerned about the ratio of transmitted and incoming flux, errors in absolute calibration could easily be adjusted to obtain a high relative accuracy.

The biggest uncertainties in the presented analysis lie in the correct co-location of the optical measurements with the physical sea ice and surface properties. While this meta-data is easily acquired along drill hole surveys for point measurements, spatial datasets suffer from interpolation errors and especially problems of under-ice positioning. Aligning surface information, such as aerial images or drill hole measurements with the acoustic positioning system providing the ROV location can be challenging, but relative position accuracies of better than one meter can be achieved with modern technology.

7.6. Future development

If the observed changes of the physical properties of sea ice continue in the future as projected by current climate models, this will not only have direct effects, such as increasing light availability underneath the thinner sea ice. Light will also be available earlier in the season and deeper down in the water column. It will also change the relative contributions of turbulent and shortwave energy fluxes to the energy budget of sea ice. With thinner ice and an extended melting season, shortwave fluxes could be comparable or even dominant over the ocean heat flux in a much larger part of the Arctic during an extended time period. This will lead to increased internal and bottom melting, changing the sea ice structure to a more porous matrix with macroscopic channels. Short term predictions of the evolution of the sea ice cover will thus be increasingly dependent on accurate representations of shortwave radiative transfer through sea ice and accurate redistribution of the absorbed energy in the upper water column. Surface properties, such as the composition of the surface scattering layer and its transition from a melting snow cover to a layer of ice grains will have a stronger impact on shortwave fluxes, when the underlying ice is thin. This would lead to a general increase of light field variability underneath Arctic sea ice both in time and space.

The impact of this diversification of light conditions underneath the ice cover on the ecosystem is hard to predict [*Vancoppenolle et al.*, 2013], as the development of primary production is not only linked to the light regime but especially to the future development of nutrient supply and mixing in the upper ocean. As shown by *Park et al.* [2015], climate projections heavily depend on the coupled interplay of shortwave radiative transfer through sea ice, ocean heating by phytoplankton absorption which in turn influences upper ocean mixing and thus nutrient supplies. These three processes exhibit a high spatial variability which needs to be accounted for to achieve a realistic scenario of the future.

7.7. Open questions & Outlook

Many open questions remain that can be addressed either by the datasets already acquired using ROVs or future observations covering a large spatial area and different seasons:

The building database of ROV based optical measurements throughout the melting and freeze-up season will give the possibility to investigate the seasonal distribution of light transmittance on a spatially extensive dataset. This will allow us to describe the development of modal values of light transmittance throughout the season and describe the development of variability and the factors driving it during different seasons. The spring season is thus of highest interest for future investigations and a main question is: How do optical properties of sea ice change during the transition time from winter to summer, when the surface develops from dry snow over wet or flooded snow and slush to a summer surface with distinct melt ponds and bare ice?

While the current observations have been mostly focused on broadband light transmittance, a detailed analysis of the variations in spectral properties of the transmitted light is still missing but can be conducted on the datasets already present. This might enable a further disentanglement of several factors governing light transmittance, separating the effects of melt ponds, snow cover and probably even ice algal coverage. Apart from the detection of ice algal abundance, a spectral analysis could also reveal more information about their properties and composition.

The available datasets covering a large spatial area can be further investigated using geo-statistical methods to establish a link between the point measurements conducted in the past and the present datasets. This will also enable for a derivation of distribution functions for the inherent optical properties of sea ice, to guide parameter choice for radiative transfer schemes in large scale models.

Another important open question is the assessment of the influence of a spatially inhomogeneous sea ice on the vertical distribution of the deposition of solar energy causing heating in the upper water column. This needs to be better constrained to correctly estimate the heat budget of the upper ocean in the retreating sea ice zone and evaluate the response of the Arctic climate to continuing changes in the cryosphere.

To describe the changes of surface properties during the transition from winter to summer, it is crucial to better describe the changing surface layer. Currently this transition is hard to observe quantitatively, as even the nomenclature of

several intermediate stages during this melt process can be ambiguous. The partial failure of simple concepts, like what is snow thickness or even the question whether something is still snow or already ice, makes a quantitative description very difficult. Thus the main factors driving the seasonal variability of light transmission need to be identified to enable a framework for their proper quantitative description.

Another necessity is to develop further constraints on the inherent optical properties of sea ice and especially their evolution throughout the changing seasons. This requires localized small scale analysis of the thermal and structural properties of sea ice covered with melting snow together with precisely positioned optical measurements. Intensive ROV surveys would have to be combined with high precision measurements of sea ice properties along the dive tracks, so that inherent optical properties and their variability could be deduced using inverse radiative transfer modeling. These studies should be combined with laboratory experiments investigating the effects of changing temperature, melting snow cover, sea ice salinity and internal melt progression. This work will certainly benefit from high resolution spectral measurements allowing for a more complete picture of ice optical properties. A further investigation of the spatial variability of the sea ice optical properties caused by dynamical effects like the formation of pressure ridges and thin ice leads would be beneficial. The acquired inherent optical parameters need to be evaluated in the context of large scale models, to compare different radiative transfer schemes in their success of correctly forecasting summer melting.

This can be realized by enhanced observations with extended interdisciplinary payload on the ROV. While upward looking multi-beam and cameras can provide a good picture of the three-dimensional relief of ice-bottom topography, further oceanographic (temperature, salinity, currents) and bio-optical sensors (fluorometers, spectral transmissometer, oxygen, nutrients, turbidity) could reveal the fine scale structure of the water column below sea ice, giving new insights into mixing processes caused by water turbulence in the upper 20m.

For a large spatial coverage, this instrument suite could be integrated into autonomous underwater vehicles (AUV) that recently improved their skills of under-ice navigation significantly. For an optimal usability of the data, ROV or AUV surveys should be combined with high resolution aerial photography, laser scanner surveys revealing high resolution surface topography or UAV (unmanned aerial vehicle) borne spectral albedo measurements. The full seasonal cycle could be observed when those high resolution spatial measurements are conducted either on a manned drifting station or an advanced ice-strengthened

autonomous observatory yielding high resolution 4D sea ice mapping covering both the seasonal and spatial variability.

8. Summary & Conclusions

This thesis shows, that spatially extensive ROV surveys underneath sea ice are a unique tool for the analysis of spatial variability, covering all aspects from microscopic radiative transfer theory over lateral and vertical variability of floe scale and regional energy fluxes to the large scale picture of the sea ice climate- and ecosystem.

During summer, the main drivers of this variability are albedo variations caused by melt pond coverage and variations in ice thickness. The result that albedo variations dominate the light variability on small scales but ice thickness variations are the important driver on larger scales justifies the use of ice thickness as predictor for the under ice light field within large scale models for example by using the proposed method of deriving under-ice light from albedo and ice thickness distributions.
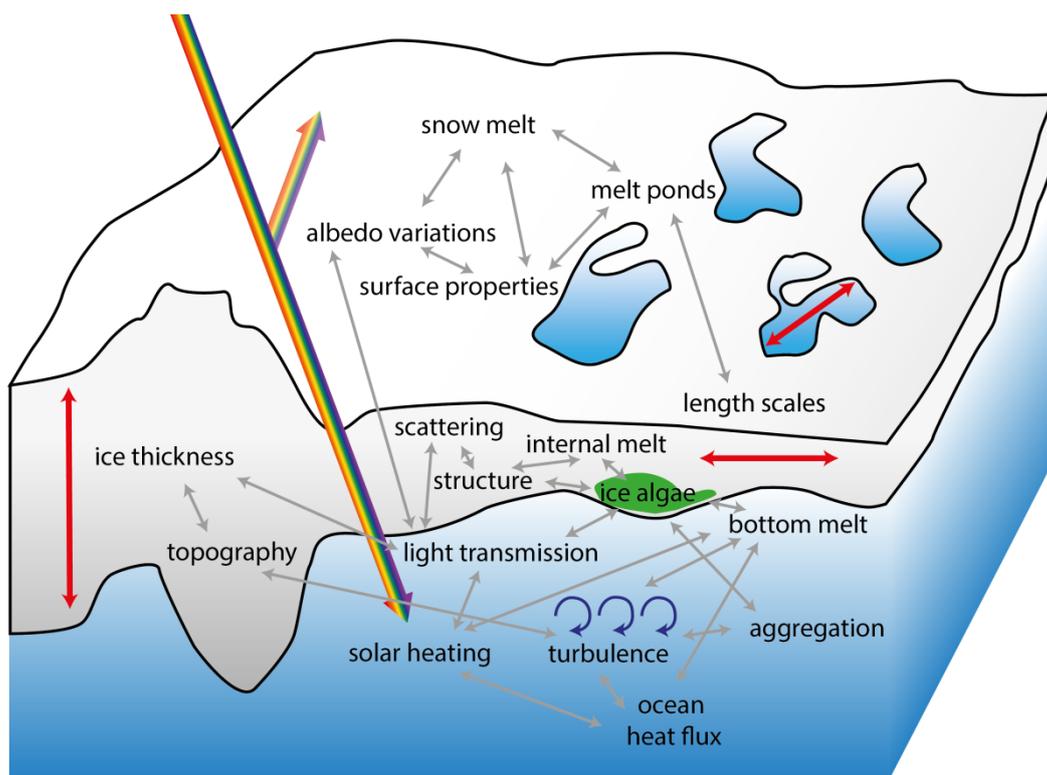
Figure 5: Overview about the different compartments and processes as well as their relationships discussed in this thesis.

A second contribution of this thesis to the current knowledge about the spatial variability of the under ice light field is the description and quantification of geometric effects caused by the inhomogeneous sea ice surface. Together with the theoretical and experimental confirmation of the anisotropic scattering coefficient of sea ice, providing new quantitative knowledge about the angular radiance distribution under sea ice, these results will enable a better evaluation of the vertical distribution of solar heating of the ocean underneath the sea ice, which in turn is relevant for the fate of the melting sea ice.

These advances in the understanding of the variable light-field under sea ice, combined with intensive interdisciplinary collaboration, enabled one of the first Arctic wide estimations of primary productivity including the contribution by sea-ice algae and also provided an outlook how primary productivity could respond to the ongoing retreat of sea ice. The establishment of procedures for ROV operations under polar sea ice and the development of the methodology allowed not only for a spatially extensive survey of the under-ice light-field, but also for the first quantification of the spatial distribution of ice algal aggregates. This study shows that the physical interplay of algal aggregate buoyancy, ice-relative currents and the topography of the ice-underside is responsible for their spatial distribution. The proposed approach for quantification of under-ice algae will help to better understand the Arctic carbon cycle and the cryo-benthic coupling in a sea ice covered ocean.

9. Literature

Antoine, D., M. Babin, J.-F. Berthon, A. Bricaud, B. Gentili, H. Loisel, S. Maritorena, and D. Stramski (2014), Shedding Light on the Sea: André Morel's Legacy to Optical Oceanography, *Annual Review of Marine Science*, *6*(1), 1-21, doi: doi:10.1146/annurev-marine-010213-135135.

Arndt, S., and M. Nicolaus (2014), Seasonal cycle and long-term trend of solar energy fluxes through Arctic sea ice, *The Cryosphere*, *8*(6), 2219-2233, doi: 10.5194/tc-8-2219-2014.

Arrigo, K. R. (2014), Sea Ice Ecosystems, *Annual Review of Marine Science*, *6*(1), 439-467, doi: 10.1146/annurev-marine-010213-135103.

Arrigo, K. R., C. W. Sullivan, and J. N. Kremer (1991), A biooptical model of Antarctic sea ice, *J. Geophys. Res.-Oceans*, *96*(C6), 10581-10592, doi: 10.1029/91jc00455.

Arrigo, K. R., G. van Dijken, and S. Pabi (2008), Impact of a shrinking Arctic ice cover on marine primary production, *Geophys. Res. Lett.*, *35*(19), L19603, doi: 10.1029/2008gl035028.

Arrigo, K. R., et al. (2012), Massive Phytoplankton Blooms Under Arctic Sea Ice, *Science*, *336*(6087), 1408, doi: 10.1126/science.1215065.

Assmy, P., et al. (2013), Floating Ice-Algal Aggregates below Melting Arctic Sea Ice, *PLoS ONE*, *8*(10), e76599, doi: 10.1371/journal.pone.0076599.

Bélanger, S., S. A. Cizmeli, J. Ehn, A. Matsuoka, D. Doxaran, S. Hooker, and M. Babin (2013), Light absorption and partitioning in Arctic Ocean surface waters: impact of multiyear ice melting, *Biogeosciences*, *10*(10), 6433-6452, doi: 10.5194/bg-10-6433-2013.

Boetius, A. (2015), The expedition PS86 of the research vessel POLARSTERN to the Arctic Ocean in 2014, edited, Alfred Wegener Institute for Polar and Marine Research, Bremerhaven.

Bowen, A. D., M. Jakuba, D. Yoerger, C. German, J. C. Kinsey, L. L. Whitcomb, and L. Mayer (2012), Lightly tethered unmanned underwater vehicle for under-ice exploration, paper presented at Aerospace Conference, 2012 IEEE, 3-10 March 2012.

Bowen, A. D., et al. (2014), Design of Nereid-UI: A remotely operated underwater vehicle for oceanographic access under ice, paper presented at Oceans - St. John's, 2014, 14-19 Sept. 2014.

Chandrasekhar, S. (1960), *Radiative transfer*, Dover Publications.

Cox, C., T. Uttal, S. Starkweather, J. Intrieri, M. Maturilli, V. Kustov, E. Konopleva, S. Crepinsek, and C. Long (2015), Using pan-Arctic, springtime, surface radiation observations to quantify atmospheric preconditioning processes that impact the sea ice melt season, in *EGU General Assembly 2015*, edited, Geophysical Research Abstracts, Wien.

Curry, J. A., J. L. Schramm, and E. E. Ebert (1995), Sea Ice-Albedo Climate Feedback Mechanism, *J. Clim.*, *8*(2), 240-247, doi: 10.1175/1520-0442(1995)008<0240:SIACFM>2.0.CO;2.

Divine, D. V., M. A. Granskog, S. R. Hudson, C. A. Pedersen, T. I. Karlsen, S. A. Divina, A. H. H. Renner, and S. Gerland (2015), Regional melt-pond fraction and albedo of thin Arctic first-year drift ice in late summer, *The Cryosphere*, *9*(1), 255-268, doi: 10.5194/tc-9-255-2015.

Ehn, J. K., T. N. Papakyriakou, and D. G. Barber (2008), Inference of optical properties from radiation profiles within melting landfast sea ice, *J. Geophys. Res.-Oceans*, *113*(C9), doi: 10.1029/2007jc004656.

Ehn, J. K., C. J. Mundy, D. G. Barber, H. Hop, A. Rossnagel, and J. Stewart (2011), Impact of horizontal spreading on light propagation in melt pond covered seasonal sea ice in the Canadian Arctic, *J. Geophys. Res.-Oceans*, *116*, doi: 10.1029/2010jc006908.

Eicken, H., and M. Salganek (2010), *Field Techniques for Sea-Ice Research*, University of Alaska Press.

Fernández-Méndez, M., F. Wenzhöfer, I. Peeken, H. L. Sørensen, R. N. Glud, and A. Boetius (2014), Composition, Buoyancy Regulation and Fate of Ice Algal Aggregates in the Central Arctic Ocean, *PLoS ONE*, *9*(9), e107452, doi: 10.1371/journal.pone.0107452.

Fetterer, F., and N. Untersteiner (1998), Observations of melt ponds on Arctic sea ice, *J. Geophys. Res.-Oceans*, *103*(C11), 24821-24835, doi: 10.1029/98jc02034.

Fetterer, F., K. Knowles, W. Meier, and M. Savoie (2002, updated daily), Sea Ice Index. , edited by N. S. a. I. D. Center, Boulder, Colorado USA.

Flocco, D., D. L. Feltham, and A. K. Turner (2010), Incorporation of a physically based melt pond scheme into the sea ice component of a climate model, *Journal of Geophysical Research: Oceans*, *115*(C8), n/a-n/a, doi: 10.1029/2009JC005568.

Flocco, D., D. Schroeder, D. L. Feltham, and E. C. Hunke (2012), Impact of melt ponds on Arctic sea ice simulations from 1990 to 2007, *Journal of Geophysical Research: Oceans*, *117*(C9), n/a-n/a, doi: 10.1029/2012JC008195.

Flöder, S., J. Urabe, and Z.-i. Kawabata (2002), The influence of fluctuating light intensities on species composition and diversity of natural phytoplankton communities, *Oecologia*, *133*(3), 395-401, doi: 10.1007/s00442-002-1048-8.

Frey, K. E., D. K. Perovich, and B. Light (2011), The spatial distribution of solar radiation under a melting Arctic sea ice cover, *Geophys. Res. Lett.*, *38*, L22501, doi: 10.1029/2011gl049421.

Gascard, J.-C., et al. (2008), Exploring Arctic Transpolar Drift During Dramatic Sea Ice Retreat, *Eos, Transactions American Geophysical Union*, *89*(3), 21-22, doi: 10.1029/2008EO030001.

Grenfell, T. C. (1977), The optical properties of ice and snow in the arctic basin, *J. Glaciol.*, *18*(80), 445-463.

Grenfell, T. C., and D. K. Perovich (1981), Radiation absorption coefficients of polycrystalline ice from 400–1400 nm, *Journal of Geophysical Research-Oceans and Atmospheres*, *86*(NC8), 7447-7450, doi: 10.1029/JC086iC08p07447.

Grenfell, T. C., and D. Hedrick (1983), Scattering of visible and near infrared radiation by NaCl ice and glacier ice, *Cold Reg. Sci. Tech.*, *8*(2), 119-127, doi: 10.1016/0165-232x(83)90003-4.

Grenfell, T. C., B. Light, and D. K. Perovich (2006), Spectral transmission and implications for the partitioning of shortwave radiation in arctic sea ice, in *Annals of Glaciology, Vol 44, 2006*, edited by P. Langhorne and V. Squire, pp. 1-6, Int Glaciological Soc, Cambridge.

Grobbelaar, J., L. Nedbal, and V. Tichý (1996), Influence of high frequency light/dark fluctuations on photosynthetic characteristics of microalgae photoacclimated to different light intensities and implications for mass algal cultivation, *J Appl Phycol*, *8*(4-5), 335-343, doi: 10.1007/BF02178576.

Haas, C., A. Pfaffling, S. Hendricks, L. Rabenstein, J.-L. Etienne, and I. Rigor (2008), Reduced ice thickness in Arctic Transpolar Drift favors rapid ice retreat, *Geophys. Res. Lett.*, *35*(17), L17501, doi: 10.1029/2008gl034457.

Hamre, B., J. G. Winther, S. Gerland, J. J. Stamnes, and K. Stamnes (2004), Modeled and measured optical transmittance of snow-covered first-year sea ice in Kongsfjorden, Svalbard, *J. Geophys. Res.-Oceans*, *109*(C10), doi: 10.1029/2003jc001926.

Hohenegger, C., B. Alali, K. R. Steffen, D. K. Perovich, and K. M. Golden (2012), Transition in the fractal geometry of Arctic melt ponds, *The Cryosphere*, *6*(5), 1157-1162, doi: 10.5194/tc-6-1157-2012.

Holland, M. M., D. A. Bailey, B. P. Briegleb, B. Light, and E. Hunke (2011), Improved Sea Ice Shortwave Radiation Physics in CCSM4: The Impact of Melt Ponds and Aerosols on Arctic Sea Ice, *J. Clim.*, *25*(5), 1413-1430, doi: 10.1175/JCLI-D-11-00078.1.

Hudson, S. R., M. A. Granskog, T. I. Karlsen, and K. Fossan (2012), An integrated platform for observing the radiation budget of sea ice at different spatial scales, *Cold Reg. Sci. Tech.*, *82*(0), 14-20, doi: http://dx.doi.org/10.1016/j.coldregions.2012.05.002.

Hudson, S. R., M. A. Granskog, A. Sundfjord, A. Randelhoff, A. H. H. Renner, and D. V. Divine (2013), Energy budget of first-year Arctic sea ice in advanced stages of melt, *Geophys. Res. Lett.*, *40*(11), 2679-2683, doi: Doi 10.1002/Grl.50517.

Jakuba, M. V., L. L. Whitcomb, D. R. Yoerger, and A. D. Bowen (2008), Toward under-ice operations with hybrid underwater robotic vehicles, paper presented at Autonomous Underwater Vehicles, 2008. AUV 2008. IEEE/OES, 13-14 Oct. 2008.

Katlein, C., M. Nicolaus, and C. Petrich (2014), The anisotropic scattering coefficient of sea ice, *Journal of Geophysical Research: Oceans*, doi: 10.1002/2013JC009502.

Kokhanovsky, A. A. (2006), *Cloud Optics*, Springer Netherlands.

Krembs, C., K. Tuschling, and K. von Juterzenka (2002), The topography of the ice-water interface - its influence on the colonization of sea ice by algae, *Polar Biol.*, *25*(2), 106-117, doi: 10.1007/s003000100318.

Krishfield, R., J. Toole, A. Proshutinsky, and M. L. Timmermans (2008), Automated Ice-Tethered Profilers for Seawater Observations under Pack Ice in All Seasons, *Journal of Atmospheric and Oceanic Technology*, *25*(11), 2091-2105, doi: 10.1175/2008JTECHO587.1.

Kukulya, A., et al. (2010), Under-ice operations with a REMUS-100 AUV in the Arctic, paper presented at Autonomous Underwater Vehicles (AUV), 2010 IEEE/OES, 1-3 Sept. 2010.

Kwok, R., and D. A. Rothrock (2009), Decline in Arctic sea ice thickness from submarine and ICESat records: 1958-2008, *Geophys. Res. Lett.*, *36*, doi: 10.1029/2009gl039035.

Kwok, R., G. Spreen, and S. Pang (2013), Arctic sea ice circulation and drift speed: Decadal trends and ocean currents, *Journal of Geophysical Research: Oceans*, *118*(5), 2408-2425, doi: 10.1002/jgrc.20191.

Lalande, C., E.-M. Nöthig, R. Somavilla, E. Bauerfeind, V. Shevchenko, and Y. Okolodkov (2014), Variability in under-ice export fluxes of biogenic matter in the Arctic Ocean, *Global Biogeochemical Cycles*, *28*(5), 571-583, doi: 10.1002/2013GB004735.

Lebedev, V. I., and D. N. Laikov (1999), A quadrature formula for the sphere of the 131st algebraic order of accuracy, *Doklady Mathematics*, *59*(3), 477-481.

Legendre, L., and M. Gosselin (1991), Insitu Spectroradiometric Estimation of Microalgal Biomass in 1st-Year Sea Ice, *Polar Biol.*, *11*(2), 113-115.

Leu, E., J. Wiktor, J. E. Soreide, J. Berge, and S. Falk-Petersen (2010), Increased irradiance reduces food quality of sea ice algae, *Mar. Ecol.-Prog. Ser.*, *411*, 49-60, doi: 10.3354/meps08647.

Leu, E., J. E. Soreide, D. O. Hessen, S. Falk-Petersen, and J. Berge (2011), Consequences of changing sea-ice cover for primary and secondary producers in the European Arctic shelf seas: Timing, quantity, and quality, *Prog. Oceanogr.*, *90*(1-4), 18-32, doi: 10.1016/j.pocean.2011.02.004.

Light, B., G. A. Maykut, and T. C. Grenfell (2003a), Effects of temperature on the microstructure of first-year Arctic sea ice, *Journal of Geophysical Research: Oceans*, *108*(C2), n/a-n/a, doi: 10.1029/2001JC000887.

Light, B., G. A. Maykut, and T. C. Grenfell (2003b), A two-dimensional Monte Carlo model of radiative transfer in sea ice, *J. Geophys. Res.-Oceans*, *108*(C7), doi: 10.1029/2002jc001513.

Light, B., T. C. Grenfell, and D. K. Perovich (2008), Transmission and absorption of solar radiation by Arctic sea ice during the melt season, *J. Geophys. Res.-Oceans*, *113*(C3), doi: 10.1029/2006jc003977.

Lindsay, R., and A. Schweiger (2015), Arctic sea ice thickness loss determined using subsurface, aircraft, and satellite observations, *The Cryosphere*, *9*(1), 269-283, doi: 10.5194/tc-9-269-2015.

Litchman, E. (2000), Growth rates of phytoplankton under fluctuating light, *Freshwater Biology*, *44*(2), 223-235.

Lowry, K. E., G. L. van Dijken, and K. R. Arrigo (2014), Evidence of under-ice phytoplankton blooms in the Chukchi Sea from 1998 to 2012, *Deep Sea Research Part II: Topical Studies in Oceanography*, *105*(0), 105-117, doi: http://dx.doi.org/10.1016/j.dsr2.2014.03.013.

Lu, Y., M. Zhou, and T. Wu (2013), Validation of parameterizations for the surface turbulent fluxes over sea ice with CHINARE 2010 and SHEBA data, *2013*, doi: 10.3402/polar.v32i0.20818.

Markus, T., J. C. Stroeve, and J. Miller (2009), Recent changes in Arctic sea ice melt onset, freezeup, and melt season length, *J. Geophys. Res.-Oceans*, *114*, doi: 10.1029/2009jc005436.

Maslanik, J. A., J. Stroeve, C. Fowler, and W. Emery (2011), Distribution and trends in Arctic sea ice age through spring 2011, *Geophys. Res. Lett.*, *38*, doi: 10.1029/2011gl047735.

Maslanik, J. A., C. Fowler, J. Stroeve, S. Drobot, J. Zwally, D. Yi, and W. Emery (2007), A younger, thinner Arctic ice cover: Increased potential for rapid, extensive sea-ice loss, *Geophys. Res. Lett.*, *34*(24), L24501, doi: 10.1029/2007gl032043.

Maykut, G. A., and N. Untersteiner (1971), Some results from a time-dependent thermodynamic model of sea ice, *Journal of Geophysical Research*, *76*(6), 1550-1575, doi: 10.1029/JC076i006p01550.

McFarland, C., M. Jakuba, S. Suman, J. Kinsey, and L. L. Whitcomb (2015), Toward Ice-Relative Navigation of Underwater Robotic Vehicles Under Moving Sea-Ice:

Experimental Evaluation in the Arctic Sea in *IEEE ICRA 2015*, edited, Seattle WA (in press).

Meier, W. N., et al. (2014), Arctic sea ice in transformation: A review of recent observed changes and impacts on biology and human activity, *Rev Geophys*, *52*(3), 185-217, doi: Doi 10.1002/2013rg000431.

Melnikov, I. (1997), The Arctic sea ice ecosystem, edited, Cambridge Univ Press.

Mobley, C. D. (1994), *Light and water: radiative transfer in natural waters*, Academic Press.

Mobley, C. D., G. F. Cota, T. C. Grenfell, R. A. Maffione, W. S. Pegau, and D. K. Perovich (1998), Modeling light propagation in sea ice, *IEEE Transactions on Geoscience and Remote Sensing 36*(5), 1743-1749, doi: 10.1109/36.718642.

Mundy, C. J., D. G. Barber, and C. Michel (2005), Variability of snow and ice thermal, physical and optical properties pertinent to sea ice algae biomass during spring, *Journal of Marine Systems*, *58*(3-4), 107-120, doi: 10.1016/j.jmarsys.2005.07.003.

Mundy, C. J., J. K. Ehn, D. G. Barber, and C. Michel (2007), Influence of snow cover and algae on the spectral dependence of transmitted irradiance through Arctic landfast first-year sea ice, *J. Geophys. Res.-Oceans*, *112*(C3), doi: 10.1029/2006jc003683.

Nicolaus, M., and C. Katlein (2012), Mapping radiation transfer through sea ice using a remotely operated vehicle (ROV), *The Cryosphere Discuss.*, *6*(5), 3613-3646, doi: 10.5194/tcd-6-3613-2012.

Nicolaus, M., and C. Katlein (2013), Mapping radiation transfer through sea ice using a remotely operated vehicle (ROV), *The Cryosphere*, *7*(3), 763-777, doi: 10.5194/tc-7-763-2013.

Nicolaus, M., S. R. Hudson, S. Gerland, and K. Munderloh (2010a), A modern concept for autonomous and continuous measurements of spectral albedo and transmittance of sea ice, *Cold Reg. Sci. Tech.*, *62*(1), 14-28, doi: 10.1016/j.coldregions.2010.03.001.

Nicolaus, M., C. Katlein, J. Maslanik, and S. Hendricks (2012), Changes in Arctic sea ice result in increasing light transmittance and absorption, *Geophys. Res. Lett.*, *39*, L24501, doi: 10.1029/2012gl053738.

Nicolaus, M., C. Petrich, S. R. Hudson, and M. A. Granskog (2013a), Variability of light transmission through Arctic land-fast sea ice during spring, *The Cryosphere*, *6*(5), 4363-4385, doi: 10.5194/tcd-6-4363-2012.

Nicolaus, M., S. Arndt, C. Katlein, J. Maslanik, and S. Hendricks (2013b), Correction to "Changes in Arctic sea ice result in increasing light transmittance and absorption", *Geophys. Res. Lett.*, *40*(11), 2699-2700, doi: 10.1002/grl.50523.

Nicolaus, M., S. Gerland, S. R. Hudson, S. Hanson, J. Haapala, and D. K. Perovich (2010b), Seasonality of spectral albedo and transmittance as observed in the Arctic Transpolar Drift in 2007, *J. Geophys. Res.-Oceans*, *115*, doi: 10.1029/2009jc006074.

Nicotra, A. B., R. L. Chazdon, and S. V. B. Iriarte (1999), SPATIAL HETEROGENEITY OF LIGHT AND WOODY SEEDLING REGENERATION IN TROPICAL WET FORESTS, *Ecology*, *80*(6), 1908-1926, doi: 10.1890/0012-9658(1999)080[1908:SHOLAW]2.0.CO;2.

Ohmura, A., et al. (1998), Baseline Surface Radiation Network (BSRN/WCRP): New Precision Radiometry for Climate Research, *Bulletin of the American Meteorological Society*, *79*(10), 2115-2136, doi: 10.1175/1520-0477(1998)079<2115:BSRNBW>2.0.CO;2.

Park, J.-Y., J.-S. Kug, J. Bader, R. Rolph, and M. Kwon (2015), Amplified Arctic warming by phytoplankton under greenhouse warming, *Proceedings of the National Academy of Sciences*, *112*(19), 5921-5926, doi: 10.1073/pnas.1416884112.

Perovich, D. K. (1990), Theoretical estimates of light reflection and transmission by spatially complex and temporally varying sea ice covers, *J. Geophys. Res.-Oceans*, *95*(C6), 9557-9567, doi: 10.1029/JC095iC06p09557.

Perovich, D. K. (1996), The optical properties of sea ice, *Monograph 96-1*.

Perovich, D. K. (2005), On the aggregate-scale partitioning of solar radiation in Arctic sea ice during the Surface Heat Budget of the Arctic Ocean (SHEBA) field experiment, *J. Geophys. Res.-Oceans*, *110*(C3), doi: 10.1029/2004jc002512.

Perovich, D. K. (2011), The changing Arctic sea ice cover, *Oceanography*, *24*(3), 162-173.

Perovich, D. K., and B. Elder (2002), Estimates of ocean heat flux at SHEBA, *Geophys. Res. Lett.*, *29*(9), 58-51-58-54, doi: 10.1029/2001GL014171.

Perovich, D. K., and J. A. Richter-Menge (2006), From points to Poles: extrapolating point measurements of sea-ice mass balance, *Ann. Glaciol.*, *44*(1), 188-192, doi: 10.3189/172756406781811204.

Perovich, D. K., and C. Polashenski (2012), Albedo evolution of seasonal Arctic sea ice, *Geophys. Res. Lett.*, *39*, doi: 10.1029/2012gl051432.

Perovich, D. K., and K. F. Jones (2014), The seasonal evolution of sea ice floe size distribution, *Journal of Geophysical Research: Oceans*, *119*(12), 8767-8777, doi: 10.1002/2014JC010136.

Perovich, D. K., C. S. Roesler, and W. S. Pegau (1998a), Variability in Arctic sea ice optical properties, *J. Geophys. Res.-Oceans*, *103*(C1), 1193-1208, doi: 10.1029/97jc01614.

Perovich, D. K., T. C. Grenfell, B. Light, and P. V. Hobbs (2002), Seasonal evolution of the albedo of multiyear Arctic sea ice, *J. Geophys. Res.-Oceans*, *107*(C10), doi: 10.1029/2000jc000438.

Perovich, D. K., K. F. Jones, B. Light, H. Eicken, T. Markus, J. Stroeve, and R. Lindsay (2011), Solar partitioning in a changing Arctic sea-ice cover, *Ann. Glaciol.*, *52*(57), 192-196.

Perovich, D. K., et al. (1998b), Field observations of the electromagnetic properties of first-year sea ice, *Geoscience and Remote Sensing, IEEE Transactions on*, *36*(5), 1705-1715, doi: 10.1109/36.718639.

Petrich, C., M. Nicolaus, and R. Gradinger (2012a), Sensitivity of the light field under sea ice to spatially inhomogeneous optical properties and incident light assessed with three-dimensional Monte Carlo radiative transfer simulations, *Cold Reg. Sci. Tech.*, *73*, 1-11, doi: 10.1016/j.coldregions.2011.12.004.

Petrich, C., H. Eicken, C. M. Polashenski, M. Sturm, J. P. Harbeck, D. K. Perovich, and D. C. Finnegan (2012b), Snow dunes: A controlling factor of melt pond distribution on Arctic sea ice, *J. Geophys. Res.*, *117*(C9), C09029, doi: 10.1029/2012jc008192.

Polyakov, I., et al. (2007), Observational program tracks Arctic Ocean transition to a warmer state, *Eos, Transactions American Geophysical Union*, *88*(40), 398-399, doi: 10.1029/2007EO400002.

Rampal, P., J. Weiss, and D. Marsan (2009), Positive trend in the mean speed and deformation rate of Arctic sea ice, 1979–2007, *Journal of Geophysical Research: Oceans*, *114*(C5), C05013, doi: 10.1029/2008JC005066.

Renner, A. H. H., S. Gerland, C. Haas, G. Spreen, J. F. Beckers, E. Hansen, M. Nicolaus, and H. Goodwin (2014), Evidence of Arctic sea ice thinning from direct observations, *Geophys. Res. Lett.*, *41*(14), 5029-5036, doi: Doi 10.1002/2014gl060369.

Richter-Menge, J. A., D. K. Perovich, B. C. Elder, K. Claffey, I. Rigor, and M. Ortmeyer (2006), Ice mass-balance buoys: a tool for measuring and attributing changes in the thickness of the Arctic sea-ice cover, *Ann. Glaciol.*, *44*(1), 205-210, doi: 10.3189/172756406781811727.

Rösel, A., and L. Kaleschke (2012), Exceptional melt pond occurrence in the years 2007 and 2011 on the Arctic sea ice revealed from MODIS satellite data, *J. Geophys. Res.*, *117*(C5), C05018, doi: 10.1029/2011jc007869.

Rothrock, D. A., D. B. Percival, and M. Wensnahan (2008), The decline in arctic sea-ice thickness: Separating the spatial, annual, and interannual variability in a quarter century of submarine data, *J. Geophys. Res.*, *113*(C5), C05003, doi: 10.1029/2007jc004252.

Roulet, R. R., G. A. Maykut, and I. C. Grenfell (1974), Spectrophotometers for the measurement of light in polar ice and snow, *Appl. Optics*, *13*(7), 1652-1659, doi: 10.1364/ao.13.001652.

Schröder, D., D. L. Feltham, D. Flocco, and M. Tsamados (2014), September Arctic sea-ice minimum predicted by spring melt-pond fraction, *Nature Clim. Change*, *4*(5), 353-357, doi: 10.1038/nclimate2203.

Serreze, M. C., M. M. Holland, and J. Stroeve (2007), Perspectives on the Arctic's Shrinking Sea-Ice Cover, *Science*, *315*(5818), 1533-1536, doi: 10.1126/science.1139426.

Solomon, S. (2007), *Climate Change 2007: The Physical Science Basis : Contribution of Working Group I to the Fourth Assessment Report of the Intergovernmental Panel on Climate Change*, Cambridge University Press.

Stroeve, J. C., M. M. Holland, W. Meier, T. Scambos, and M. Serreze (2007), Arctic sea ice decline: Faster than forecast, *Geophys. Res. Lett.*, *34*(9), doi: 10.1029/2007gl029703.

Stroeve, J. C., M. C. Serreze, M. M. Holland, J. E. Kay, J. Malanik, and A. P. Barrett (2012), The Arctic's rapidly shrinking sea ice cover: a research synthesis, *Climatic Change*, *110*(3-4), 1005-1027, doi: DOI 10.1007/s10584-011-0101-1.

Thomas, N. D., and G. S. Dieckmann (2010), *Sea Ice*, John Wiley \& Sons.

Thorndike, A. S., D. A. Rothrock, G. A. Maykut, and R. Colony (1975), The thickness distribution of sea ice, *Journal of Geophysical Research*, *80*(33), 4501-4513, doi: 10.1029/JC080i033p04501.

Trodahl, H. J., R. G. Buckley, and S. Brown (1987), Diffusive transport of light in sea ice, *Appl. Optics*, *26*(15), 3005-3011, doi: 10.1364/AO.26.003005.

Tschudi, M., C. Fowler, J. Maslanik, and J. Stroeve (2010), Tracking the Movement and Changing Surface Characteristics of Arctic Sea Ice, *Ieee J-Stars*, *3*(4), 536-540, doi: Doi 10.1109/Jstars.2010.2048305.

Vancoppenolle, M., L. Bopp, G. Madec, J. Dunne, T. Ilyina, P. R. Halloran, and N. Steiner (2013), Future Arctic Ocean primary productivity from CMIP5 simulations: Uncertain outcome, but consistent mechanisms, *Global Biogeochemical Cycles*, *27*(3), 605-619, doi: 10.1002/gbc.20055.

Wadhams, P., J. P. Wilkinson, and S. D. McPhail (2006), A new view of the underside of Arctic sea ice, *Geophys. Res. Lett.*, *33*(4), L04501, doi: 10.1029/2005GL025131.

Wassmann, P., and M. Reigstad (2011), Future Arctic Ocean Seasonal Ice Zones and Implications for Pelagic-Benthic Coupling, *Oceanography*, *24*(3), 220-231.

Wijesekera, H., W. S. Pegau, and T. Boyd (2005), Effect of surface waves on the irradiance distribution in the upper ocean, *Opt. Express*, *13*(23), 9257-9264, doi: 10.1364/OPEX.13.009257.

Williams, G. D., T. Maksym, J. Wilkinson, C. Kunz, C. Murphy, P. Kimball, and H. Singh (2015), Thick and deformed Antarctic sea ice mapped with autonomous underwater vehicles, *Nature Geosci*, *8*(1), 61-67, doi: 10.1038/ngeo2299.

Williams, G. D., et al. (2013), Beyond Point Measurements: Sea Ice Floes Characterized in 3-D, *Eos, Transactions American Geophysical Union*, *94*(7), 69-70, doi: 10.1002/2013EO070002.

Zeebe, R. E., H. Eicken, D. H. Robinson, D. WolfGladrow, and G. S. Dieckmann (1996), Modeling the heating and melting of sea ice through light absorption by

microalgae, *J. Geophys. Res.-Oceans*, *101*(C1), 1163-1181, doi: 10.1029/95jc02687.

10. Acknowledgements

11. Appendix

11.1. Talks on international conferences

- Katlein, C. , Nicolaus, M. , Jakuba, M. , Suman, S. , Elliott, S. , Whitcomb, L. L. , McFarland, C. , Perovich, D. K. , Gerdes, R. , Boetius, A. and German, C. (2015) **Influence of ice thickness and surface properties on light transmission through Arctic sea ice** , EGU General Assembly 2015, Wien, 13 April 2015 - 17 April 2015 . hdl:10013/epic.45378 ECC 2014

- Katlein, C. , Arndt, S. , Fernandez Mendez, M. , Lange, B. , Nicolaus, M. , Wenzhöfer, F. , Jakuba, M. and German, C. (2014) **Investigating changes in the climate- and ecosystem of Arctic sea ice using remotely operated vehicles**, ECC 2014, Bremen . hdl:10013/epic.44171

- Katlein, C. , Nicolaus, M. and Petrich, C. (2014) **Anisotropic radiative transfer in sea ice**, International Symposium on Sea Ice in a Changing Environment, Hobart, Tasmania, 10 March 2014 - 14 March 2014 . hdl:10013/epic.43154 GRS 2013

- Katlein, C. and Nicolaus, M. (2013) **Consequences of micro-scale optical properties of sea ice on light availability in sea ice habitats**, Gordon Research Seminar on Polar Marine Science, Ventura, 9 March 2013 - 10 March 2013 . hdl:10013/epic.41245

11.2. Posters on international conferences

- Katlein, C. , Fernandez Mendez, M. , Wenzhöfer, F. and Nicolaus, M. (2015) **Distribution of algal aggregates under summer sea ice in the Central Arctic**, Arctic Frontiers 2015, Tromsö, January 2015 hdl:10013/epic.45024

- Katlein, C. , Nicolaus, M. , Fernández, M. and Wenzhöfer, F. (2014) **Distribution of algal aggregates under summer sea ice in the Central Arctic**, International Symposium on Sea Ice in a Changing Environment, Hobart, Tasmania, 10 March 2014. hdl:10013/epic.43155

- Katlein, C. and Nicolaus, M. (2013) **Consequence of micro-scale optical properties of sea ice on light availability in sea ice habitats**, Gordon Research Conference on Polar Marine Science, Ventura, CA, 10 March 2013. hdl:10013/epic.41246

11.3. Reports

- **Sea Ice Physics**, Stefan Hendricks, Marcel Nicolaus, Thomas Krumpen, Christian Katlein, Benjamin Lange, Martin Schiller, Larysa Istomina, Scott Sorensen, in: Boetius, A. (2013): **The expedition of the research vessel "Polarstern" to the Arctic in 2012 (ARK-XXVII/3)** , Berichte zur Polar- und Meeresforschung, Bremerhaven, Alfred Wegener Institute for Polar and Marine Research, 663 , 166 p. hdl:10013/epic.41622

- **Sea-ice-optics and ROV-operations during ARKXXVII/3 - IceArc 2012,** Katlein, C. , Nicolaus, M. , Schiller, M. , Istomina, L. , Sörensen, S. , Hendricks, S. , Krumpen, T. and Lange, B. (2012) hdl:10013/epic.40404

- **Sea-ice observations**, Christian Katlein, Stefanie Arndt, Mikko Lensu, Marcel Nicolaus, in: **The expedition PS86 of the research vessel POLARSTERN to the Arctic Ocean in 2014** , Boetius, A. (2015) , Berichte zur Polar- und Meeresforschung, Bremerhaven, Alfred Wegener Institute for Polar and Marine Research, 685 , 133 p. hdl:10013/epic.44857

- **Sea Ice Physics**, Jakob Belter, Christian Katlein, Thomas Krumpen, Sebastian Schulte-Kortnack, Sascha Willmes, in: **The expedition PS92 of the research vessel POLARSTERN to the Arctic Ocean in 2015 (TRANSSIZ),** Peeken I. (2015), Berichte zur Polar- und Meeresforschung, Bremerhaven, Alfred Wegener Institute for Polar and Marine Research, to appear fall 2015

11.4. List of archived datasets

- **Katlein, Christian** et al. (2014): Solar radiation over and under sea ice and photographic quantification of Ice algal aggregates during the POLARSTERN cruise ARK-XXVII/3 (IceArc) in summer 2012. doi:10.1594/PANGAEA.833292

- **Katlein, Christian; Arndt, Stefanie; Nicolaus, Marcel (2014):** Snow thickness measurements at sea ice station PS86/071-1. *Alfred Wegener Institute, Helmholtz Center for Polar and Marine Research, Bremerhaven*, doi:10.1594/PANGAEA.835391

- **Katlein, Christian; Arndt, Stefanie; Nicolaus, Marcel (2014):** Sea ice conditions during POLARSTERN cruise PS86 (ARK-XXVIII/3 AURORA). *Alfred Wegener Institute, Helmholtz Center for Polar and Marine Research, Bremerhaven*, doi:10.1594/PANGAEA.835578

- **Katlein, Christian et al. (2015):** Solar radiation over and under sea ice at ROV station PS86/081-1 during POLARSTERN cruise PS86 (AURORA) in July 2014. Dataset #846130 (DOI registration in progress)

STATUTORY DECLARATION

(on Authorship of a Dissertation)

I, **Christian Katlein** hereby declare that I have written this PhD thesis independently, unless where clearly stated otherwise. I have used only the sources, the data and the support that I have clearly mentioned. This PhD thesis has not been submitted for conferral of degree elsewhere.

I confirm that no rights of third parties will be infringed by the publication of this thesis.

Bremen, November 6, 2015

Signature _____